ABSTRACT

Plasmonics and Epsilon-near-zero Photonics in Optical Fiber and Thin Film Platforms: From Extreme Light Nanofocusing to Enhanced Spontaneous Emission

Khant Minn, Ph.D.

Co-mentor: Zhenrong Zhang, Ph.D.
Co-mentor: Howard Lee, Ph.D.

The major challenges in the study of light-matter interaction in the deep subwavelength regime are the inefficient conversion of nearfield to farfield energy, low signal-to-noise ratio, complicated device designs requiring complex multi-step fabrication processes. Metallic nanowires supporting surface plasmon polaritons (SPP) can localize optical fields at nanoscale tapered ends for near-field imaging. Similarly, epsilon-near-zero (ENZ) resonance, which is the behavior of light inside the medium with vanishing permittivity, in transparent conducting oxide thin films possesses strong light confinement properties. In addition, both SPP and ENZ resonances enhance the local density of optical states. Due to this property, dipole emitters near the plasmonic and ENZ medium experience greatly enhanced spontaneous emission. In this dissertation, I have applied these unique optical properties to overcome the current challenges in the field of nanoscale light-matter interaction such as nearfield scanning probe spectroscopy, nanoscale waveguiding and enhancement of light emission.

I have reported four main results in this dissertation. Firstly, I have developed a photonic-plasmonic probe that uses the linearly polarized source to excite the nanoscale plasmonic hotspot at the metallic tip apex. Secondly, as a proof-of-concept demonstration of the probe described above, I have fabricated a plasmonic nanoantenna on the end facet of a photonic crystal fiber and subsequently demonstrated the coupling of light from the fiber waveguide mode to the nanoantenna plasmonic mode. Thirdly, I have designed a novel optical waveguide of a hollow step index fiber modified with a thin layer of indium tin oxide (ITO) that supports highly confined waveguide mode at the ENZ wavelength of ITO. Lastly, I have observed the room temperature photoluminescence (PL) enhancement of molybdenum disulfide monolayers on epitaxial titanium nitride (TiN) thin films at excitation wavelengths covering the ENZ regime where TiN films transition from dielectric to plasmonic.

The first two results provide an important step toward widespread application of optical fibers incorporated with plasmonic tips in nearfield spectroscopic techniques such as tip-enhanced Raman and fluorescence microscopy, single photon excitation and quantum sensors, nanoscale optical lithography, and lab-on-fiber devices. The third result provides new understanding of coupling between ENZ and fiber waveguide modes which has potential applications in nonlinear and magneto-optics, in-fiber light manipulation, and biosensing. The fourth result enriches the fundamental understanding of how emission properties are modulated by ENZ substrates that could be important for the development of advanced nanoscale lasers and light sources, bio-sensors, and nano-optoelectronic devices.

Plasmonics and Epsilon-near-zero Photonics in Optical Fiber and Thin Film Platforms: From Extreme Light Nanofocusing to Enhanced Spontaneous Emission

by

Khant Minn, B.S., M.A.

A Dissertation

Approved by the Department of Physics

_____

Dwight P. Russell, Ph.D., Chairperson

Submitted to the Graduate Faculty of
Baylor University in Partial Fulfillment of the
Requirements for the Degree
of

Doctor of Philosophy

Approved by the Dissertation Committee

_____

Zhenrong Zhang, Ph.D., Chairperson

_____

Howard Lee, Ph.D.

_____

Marlan Scully, Ph.D.

_____

David Hilton, Ph.D.

_____

Jonathan Hu, Ph.D.

Accepted by the Graduate School

May 2021

_____

J. Larry Lyon, Ph.D., Dean

Page bearing signatures is kept on file in the Graduate School.

TABLE OF CONTENTS

LIST OF FIGURES

LIST OF TABLES

ACKNOWLEDGMENTS

I would like to thank my advisors Dr. Zhenrong Zhang and Dr. Howard Lee for their support and mentorship, without which this dissertation would not have been possible. I would also like to thank my dissertation committee members. Thank you to my colleagues Jingyi Yang, Dr. Blake Birmingham, Dr. Brian Ko, Dr. Aleksei Anopchenko and many more who have helped me in many ways on and off the lab. I also want to thank my parents and my brothers for their unwavering support.

I would like to acknowledge the support of Dr. Bernd Zechmann from the Center for Microscopy and Imaging as well as the High Performance and Research Computing Services at Baylor University.

DEDICATION

To my parents Aye Win and Than Than
who value education more than material wealth.

CHAPTER ONE

Introduction

One of the major hurdles of probing light-matter interaction in nanoscale regime is the efficient delivery and collection of electromagnetic energy to-and-fro the miniscule region of interest. For such fields as tip-enhanced Raman spectroscopy, scanning nearfield optical microscopy and fluorescent emission studies, it is imperative that light is confined to a small space in the order of nanometers. Such light confinement can be achieved by means of surface plasmon polaritons (SPP)[1-2] and epsilon-near-zero (ENZ) resonances [3-5]. Surface plasmon polaritons are collective oscillation of charges coupled with the excited electromagnetic fields that propagate along the metal-dielectric interface and evanescent in the direction perpendicular to the interface. Adjacent to the surface plasmons in the study of nanoscale light confinement is the ENZ phenomena with the vanishing permittivity of the medium as the defining attribute. The scope of this dissertation applied these two related concepts in plasmonics to develop novel devices in nearfield spectroscopy, nanoscale waveguiding and light emission, with two chapters devoted to each concept.

Surface Plasmon Polaritons

Plasmons are oscillations of free electrons in response to the localized excitation electric field, occurring in materials with negative real permittivity, such as metals, semi-metals and conducting oxides in infrared regime. SPPs occurs at the interface of metals and dielectrics due to coupling of the surface charge oscillations and photons.[6] The

propagating SPPs can be adiabatically slowed down and transformed to strongly localized fields by metallic conical tapers resulting in the concentration of the optical energy to nanoscale without major losses as shown in Fig. 1.1(a).[7-8] This nanofocusing property of SPPs is applied in various nanoscale optical and chemical imaging.[9] Among them, the direct interfacing of nano-plasmonic antennae and the optical fiber waveguide is particularly interesting because this technique benefits from the advantages of both plasmonic and photonic worlds: nanoscale light confinement of nano-antenna and flexible, low-loss, background-free light transport properties of optical fibers. In fact, the development of a novel near-to-far-field probe based on this concept will be presented in chapter two and three.

Epsilon-Near-Zero Resonance

Materials with near-zero permittivity such as transparent conduction oxides near their plasma frequency and polar materials near their phonon resonances have been shown to exhibit unique optical properties. The so-called ENZ mode in the semi-infinite three-layer (insulator-metal-insulator) geometry is indeed a special case of SPP mode in the thin-film limit when the thickness of the metal layer is much less than the plasma wavelength at which the permittivity of the material is zero (see Fig. 1.1(b)).[3-5, 10] At the ENZ resonance, due to the electric field boundary conditions which requires the displacement field to be continuous, the electric field inside the ENZ medium is strongly enhanced. In addition, assuming vacuum permeability, near-zero permittivity leads to near-zero refractive index which causes the phase velocity inside the medium to diverge and wavelength to expand, resulting in the enhancement of light-matter interaction.[11] These properties are important for the device-level application of the ENZ materials. In

particular, the integration of ENZ medium with optical fiber platform is a promising concept for long range remote sensing and will be discussed in chapter four. Moreover, the effect of ENZ medium on the neighboring light-emitting layer is of great interest for numerous nanophotonic device applications and will be discussed in chapter five.

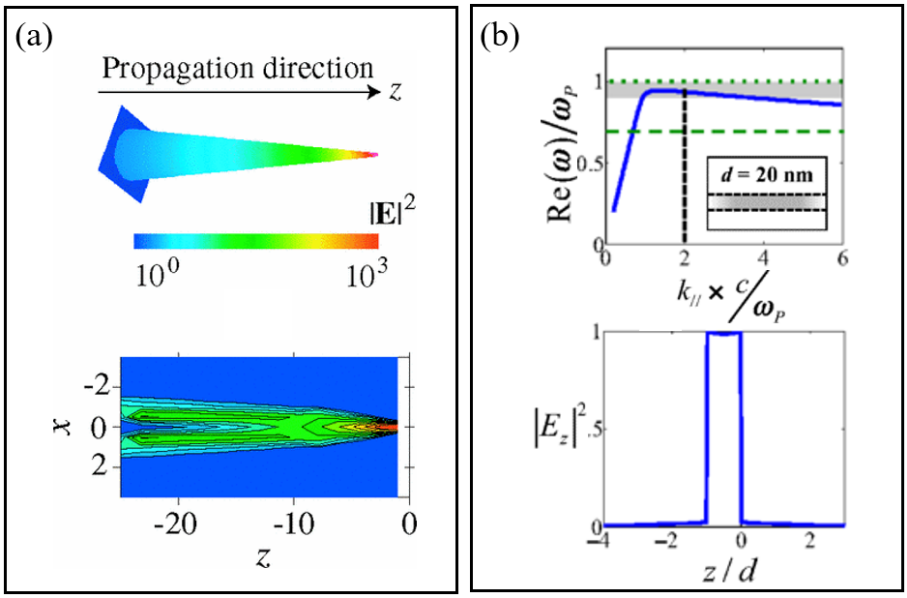

Fig. 1.1. Field enhancement properties of SPP and ENZ modes. (a) The principle of SPP nanofocusing on tapered metal waveguide. Color bar shows the electric field intensity relative to the excitation field. Adapted with permission from Phys. Rev. Lett. 2004, 93 (13), 019901. (b)ENZ mode dispersion in dielectric-metal-dielectric planar geometry (top) and the intensity profile of the transverse z-component of the electric field (below). Adapted with permission from Phys Rev B 2015, 91 (12),

Enhanced Subwavelength Coupling and Nanofocusing with Optical Fiber-Plasmonic Hybrid Probe

Chapter two and three discuss the application of SPP in nearfield sensing devices on optical fiber platform. In chapter two, a unique design of fiber-plasmonic hybrid probe for nanoscale confinement of light is presented. The conventional nearfield probe suffers from low efficiency and poor signal-to-noise ratio because of the mismatch between the microscale light energy in free space and nanoscale nearfield at the probe's tip apex.[12-15]

Recent developments in dielectric-plasmonic hybrid probes such as metal-coated tapered fiber,[16] metal-filled hollow core fiber,[17] and glass tip coated with metal gratings[18] provide an alternative platform to overcome those challenges, by focusing propagating SPP's at the nanoscale tip apex. However, they require a specialty fiber and corresponding optical components for radially polarized excitation, introducing undesirable complexities.[14, 16-17] The proposed fiber-plasmonic probe is an improvement of those existing devices. It converts linearly polarized excitation to radially polarized surface plasmons on the metallic tip to create nanoscale hotspot at the apex. The predicted focusing and collection efficiencies are 1.3% and 5.1%, significantly higher than free-space excitation and collection. Chapter two published as K. Minn, H. W. Howard Lee and Z. Zhang, Opt Express **27** (26), 38098-38108 (2019). The contributions by the authors are as follows. Khant Minn, Ho Wai Howard Lee and Zhenrong Zhang designed and conceived the project. Khant Minn performed numerical simulations. Ho Wai Howard Lee and Zhenrong Zhang supervised the project.

Interfacing Photonic Crystal Fiber with Metallic Nanoantenna for Enhanced Light Nanofocusing

Chapter three discusses the experimental realization of a hybrid fiber-plasmonic probe, a coupled system of photonic crystal fiber (PCF) and metallic nano-antenna. The probe combines the two existing light transport technologies, photonic crystal fiber and plasmonic nano-waveguide to provide a novel platform for far-to-near-field light converting device. The previous efforts in integrating plasmonic antennae with optical fibers make use of various coupling configurations such as parallel waveguide coupling through evanescent fields, [30-31] end-fire coupling,[19-20] and aperture-assisted coupling. [21-22]

The common issues with those approaches are the complexity in fabrication process which involve multi-step procedures, and the difficulty in controlling the position and size of the antenna. The approach outlined in chapter three overcomes the above difficulties by utilizing focused-electron-beam-induced-deposition technique to fabricate the device in single step. The side scattered optical measurements confirm the nanofocusing capability of the fabricated devices. Chapter three published as: K. Minn, B. Birmingham, B. Ko, H. W. H. Lee and Z. Zhang, Photonics Res **9** (2), 252-258 (2021). The contributions by the authors are as follows. Khant Minn, Blake Birmingham, Ho Wai Howard Lee and Zhenrong Zhang designed and conceived the project. Khant Minn performed numerical simulations, tip fabrications and optical measurements. Blake Birmingham and Brian Ko deposited gold on the fibers. Ho Wai Howard Lee and Zhenrong Zhang supervised the project.

Excitation of Epsilon-Near-Zero Resonance in Ultrathin Indium Tin Oxide Shell Embedded Nanostructured Optical Fiber

Chapter four and five cover the application of ENZ material in nanoscale waveguide and light emission enhancement. Chapter four shows the existence of propagating mode in an optical fiber with nano-hollow channel modified with an ENZ layer within which enhanced field is excited. Highly doped conducting oxide thin films possess ENZ near the plasma frequency, at which regime unique optical properties such as enhanced absorption,[23-26] resonant coupling,[27-28] strong nonlinear response,[29-33] and electrical modulation[34-36] can be observed. The previous studies on ENZ properties are confined to flat geometry such as planar interfaces or meta-surfaces which fundamentally limit the interaction length to sub-micrometer distances. In this work, the functionality of

ENZ mode has been extended to optical fiber platform, opening up the long-distance interaction regime. This hybrid ENZ waveguide is the first of its kind and could be used as a platform for sensing, emission control and nonlinear studies. Chapter four published as K. Minn, A. Anopchenko, J. Yang and H. W. H. Lee, Sci Rep-Uk **8** (1), 2342 (2018). The contributions by the authors are as follows. Khant Minn, Aleksei Anopchenko, and Ho Wai Howard Lee designed and conceived the project. Khant Minn, Aleksei Anopchenko, and Jingyi Yang performed numerical simulations. Ho Wai Howard Lee supervised the project.

Enhanced Spontaneous Emission of Monolayer MoS_2 on Epitaxially Grown Titanium Nitride Epsilon-Near-Zero Thin Films

Chapter five outlines the investigation of photoluminescence (PL) modulation of emitters in a two-dimensional material due to the emitter's proximity to the ENZ medium. Dipole emitters experience large density of optical states near the ENZ medium and consequently, exhibit increased rate of spontaneous emission.[37-38] The enhanced excitation field due to ENZ resonance also contributes to overall enhancement of light emission.[39] The previous studies on the ENZ-related emission enhancement are limited to complex and anisotropic structures such as metallic nanostructures and hyperbolic metamaterials. [40-45] In addition, important questions regarding the practical implementation of ENZ materials in nanoscale light-emitting devices have not been answered. These questions include whether ultrathin light emitting layers such as monolayer transition metal dichalcogenides can be coupled with ultrathin ENZ layer; how PL enhancement depends on the excitation field; how the losses of the ENZ material affect the emission; at which separation thicknesses ENZ effect plays a role; and how the

transitioning in a thin film's optical permittivity from dielectric to metallic affects the fields in the adjacent thin emitting layer. This study provides new insights by answering the above questions, using the results obtained by probing monolayer molybdenum dioxide (MoS_2), which has 1.8 eV direct bandgap, on thin (51 to 146 nm) homogeneous titanium nitride (TiN) films, whose ENZ wavelengths are in the visible spectrum, with four excitation lasers covering the ENZ wavelengths of the TiN films. This study will enrich the fundamental understanding of ENZ-enhanced PL in the nanoscale that have practical applications in the development of advanced nanophotonic light sources. Fig. 1.2. illustrates the overview of the dissertation. Chapter five published as K. Minn, A. Anopchenko, C.-W. Chang, J. Kim, Y.-J. Lu, S. Gwo and H. W. H. Lee (SPIE, 2020) Vol. 11462. The contributions by the authors are as follows. Khant Minn, Aleksei Anopchenko, and Ho Wai Howard Lee conceived the project. Ching-Wen Chang and Yu-Jung Lu fabricated the TiN films. Khant Minn fabricated spacer layers. Khant Minn and Jinmin Kim transferred MoS_2 monolayer flakes. Khant Minn performed the experiments. Khant Minn and Ching-Wen Chang performed material characterizations. Khant Minn and Aleksei Anopchenko performed numerical simulations and analyzed the results. Ho Wai Howard Lee supervised the project

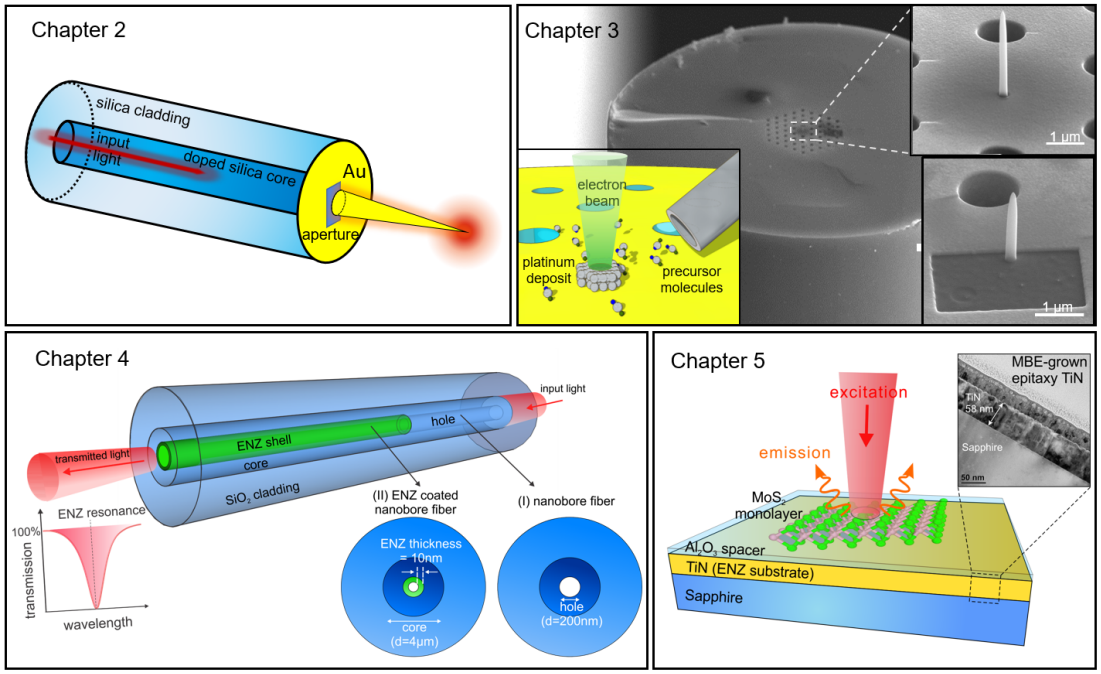

Fig. 1.2. Overview of dissertation. Chapter two presents a design of fiber-plasmonic hybrid probe for nanoscale confinement of light. Chapter three discusses the experimental realization of a hybrid fiber-plasmonic probe, a coupled system of PCF and metallic nano-antenna. Chapter four shows the existence of propagating mode in an optical fiber with nano-hollow channel modified with an ENZ layer. Chapter five outlines the investigation of PL modulation of emitters in a two-dimensional MoS_2 due to the emitter's proximity to the ENZ medium.

CHAPTER TWO

Enhanced Subwavelength Coupling and Nanofocusing with Optical Fiber-Plasmonic Hybrid Probe

This chapter published as: K. Minn, H. W. Howard Lee and Z. Zhang, Opt Express **27** (26), 38098-38108 (2019).

Introduction

One of the major hurdles of probing light-matter interaction in nanoscale regime is the efficient delivery and collection of electromagnetic energy to-and-fro the miniscule region of interest. For studies of molecular interaction with light such as tip-enhanced Raman spectroscopy (TERS), it is imperative that light be confined to a small space in the order of nanometers which can be achieved by means of localized surface plasmons [1-2]. In conventional TERS, surface plasmons are excited on the metallic probe by directly focusing the laser beam in free space in the vicinity of tip apex [46-50]. In direct illumination of the apex, far-field light energy, which has a few micrometers in diameter at the focal spot, is converted into localized field at the nanoscale tip apex. This mismatch between the mode volumes of free-space optical mode and the highly confined plasmonic mode leads to very small field overlap resulting in low coupling efficiency [12-14]. In addition, since the diffraction limited focal spot is much larger than the tip-sample interaction volume, background scattering dominates in the detected field and reduces the signal to noise ratio of detection [12, 15].

Recently, studies have shown that optical fiber-incorporated plasmonic probes can be a platform for transporting electromagnetic energy in micro- and nanoscale with high

efficiency [16, 18, 51-59]. For example, the core waveguide mode guided in the optical fiber can be coupled to plasmons on the surface of gold layer coated on the tapered end of fiber [16]. The coupled plasmonic mode then propagates to the narrow apex where it is localized and strongly focused, exhibiting immense longitudinal field enhancement which enables intense interaction with the sample placed near the apex. Similar devices that take advantage of photonic to plasmonic coupling and nano-focusing have also been proposed [14, 17]. However, these devices rely on the higher order radial vector mode (TM_{01}) for efficient coupling of photonic to plasmonic modes which requires a special type of fiber that maintains radial polarization in addition to complex and bulky radial polarizer in the excitation path. Efficient coupling of linearly polarized excitation to radial plasmons is highly desirable for a plethora of applications including medical procedures, biosensing, biomedical imaging, and near-field spectroscopy.

In this work, we propose a fiber-plasmonic hybrid probe for nanoscale confinement of light. Using full-wave finite difference time domain electromagnetic simulations, we show that linearly polarized excitation can be efficiently utilized to create hot-spot at the apex of the metallic tip on optical fiber. This is achieved by selectively exciting plasmons at only one side of the base of the tip from the optical fiber. Then we discuss the polarization selectiveness of our excitation scheme by comparing two orthogonal source polarizations. We show that the enhanced field at the apex is due to the spiraling plasmons excited by the end-fire coupling of light from fiber core at the tip base. We also demonstrate the cavity-like resonant response of the tip by spectrally mapping the field enhancement for varying tip sizes. As a figure of merit for our device, we calculate and present the focusing and collection efficiencies. The focusing efficiency

of 900 nm long tip at resonant wavelength is 1.3%. In the collection mode, the radiated power from a dipole emitter is collected by the 800 nm long tip and 5.1% of the dipole radiation is transmitted through the fiber. These efficiencies are significantly higher than free-space excitation and collection, and could be further enhanced by optimizing the fiber and tip geometries.

Results and Discussions

The proposed device is depicted in Fig. 2.1(a). The end facet of a single mode step index fiber is coated with 100 nm thick gold layer, through which a 200 nm by 400 nm rectangular aperture is etched at the center of fiber core. The thickness of the gold layer is chosen to suppress the direct transmission of light from the fiber. A half-ellipsoid gold tip, whose circular base diameter is 240 nm and length 800 nm, sits on one of the long edges of aperture in such a way that one half of the tip base interfaces with the fiber core and the other half with the gold layer (see inset of Fig. 2.1(a)). The size of the aperture is chosen to be relatively small to suppress free-space transmission through the aperture which causes background scattering while allowing significant light coupling to the exposed base of the gold tip. Note that the reported coupling efficiency have not been fully optimized. Rigorous optimization of the core and wire diameters, aperture size, position and length of the nanowire, and the material of wire could potentially enhance the coupling efficiency, which is beyond the scope of this paper. The ellipsoid shape of the apex is chosen over perfect cone shape for better enhancement due to smaller overall radiative loss [60]. The fiber core's diameter is 4 μm and supports a fundamental mode with linear polarization and Gaussian intensity distribution as shown in Fig. 2.1(b). We start with the discussion on the delivery of light from the fiber to the tip apex. When the light

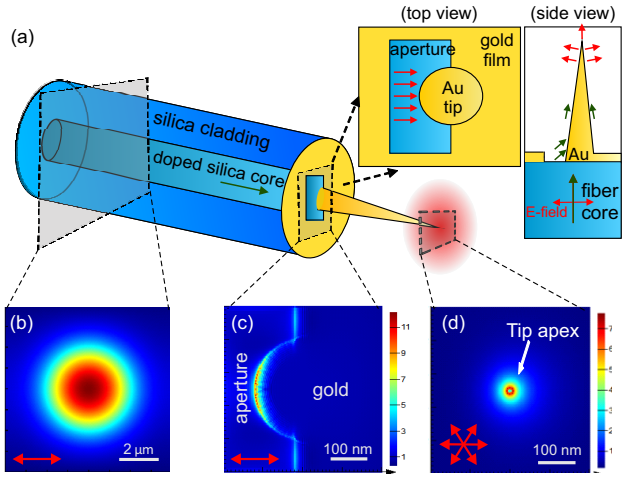

Fig. 2.1. Coupling scheme of the proposed asymmetric mode conversion and nano-focusing. (a) schematic of the device: half of the gold tip sits on edge of an aperture and the other half on the gold layer coated on a step-index fiber's end face. The insets are the top view and the side view of the tip. Electric field distribution (b) of fundamental mode supported by the fiber used as the excitation source, (c) at the base of the Au tip upon light incidence from fiber and (d) at the apex of the tip. The red arrows indicate the polarization directions of electric field. The green arrows indicate the direction of light propagation.

propagating along the fiber is incident on the base of the tip, only the exposed side of the tip base is lit up and surface plasmon polaritons are excited through the end-fire coupling. In Fig. 2.1(c), the electric field intensity at the fiber-tip interface where the coupling takes place is plotted. The excited SPP's can be recognized as the high intensity area at the illuminated side of the tip base. The excited SPP's from the illuminated side then propagate along the tip toward the tapered end where they converge to produce highly enhanced field that is confined to the nanoscale apex as shown in Fig. 2.1(d). The schematic of the simulation region is depicted in Fig. 2.2. The HE11 mode of the step index fiber is used as the input source. The perfectly match layers (PML) are used to minimize the scattered and reflected fields at the simulation boundaries, the symmetric boundary conditions (SBC) are imposed at the center plane to reduce the computation time. Mesh size of 0.2 nm is employed in the region encompassing the tip for optimal

convergence results. The details of the simulation parameters can be found in the Methods section.

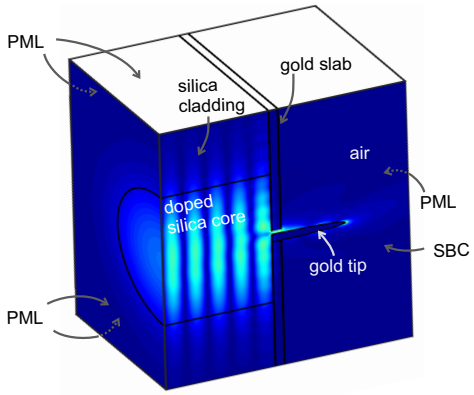

Fig. 2.2 The schematic of the 3D simulation space used in the analysis. The region contains half of the full structure. The perfectly match layers (PML) are used at the simulation boundaries, the symmetric boundary conditions (SBC) are imposed at the center plane.

In a fully symmetric end-fire coupling, i.e., if the entire base of the wire were exposed to the fiber end face, the first order mode (HE_{11}) would have been favored over radially polarized TM_{01} type SPP mode because the field overlap integral of fiber core mode with the TM_{01} mode is vanishingly small. On the other hand, HE_{11} mode's electric field vector distribution is symmetric about the polarization axis and the field vector components on opposing sides of the tip tend to cancel out as the mode propagate along the tip [61]. Furthermore, as the tip diameter gets smaller, the effective index of the mode approaches to the external medium's refractive index leading to leakage radiation [52], resulting in diminutive field near the apex. For those reasons, HE_{11} mode cannot be focused in tapered conical geometry. In our device, this problem is overcome by forcing a one-sided excitation of SPP's, breaking the symmetry of the electric field vector distribution of HE_{11} mode.

To shed light on how one-sided illumination leads to nano-focusing, we study the effect of incident polarization on excited SPP distribution. The component of incident light that is perpendicular to the side surface of the tip is most efficiently coupled to the SPP's. To elucidate this polarization selective coupling phenomenon, we compare the electric field intensity distribution on the surface of the tip resulting from two orthogonal excitation polarizations in Figs. 2.3(a) and 2.3(b). In both figures, the red arrows indicate the polarization directions of the electric field. In the first case, as plotted in Fig. 2.3(a),

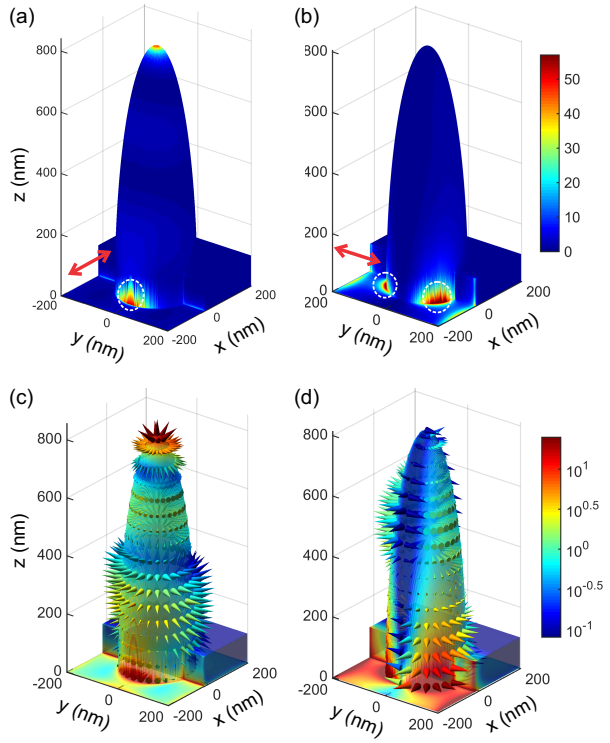

Fig. 2.3. Polarization dependence of nano-focusing. Electric field intensity distribution on the surface of the tip when the polarization of the excitation field is (a) perpendicular, and (b) parallel to the exposed edge of the tip. Intensities are normalized to the source intensity. The red arrows indicate the polarization directions of incident electric field from the fiber. The white dotted circles mark the spots of excited SPP's. (c, d) The vector cone plots depicting the electric field vector on the surface of the tip overlaid with field intensity color map in log scale for the incident polarization in (a) and (b) respectively. The color of the cone represents the magnitude of the field. The lengths of the cones are normalized to unity for the clarity of the image. The excitation wavelength is 726 nm.

the incident beam from the fiber has polarization that is perpendicular to the edge of the aperture hosting half the tip (x-polarization). The excited areas at the tip base are seen to be concentrated in the center of the illuminated side only, marked with white dotted circle in the figure, where the source field has stronger components normal to the side surface. In this scenario, the excited plasmons can propagate and get focused at the apex, achieving 88-fold intensity enhancement with respect to the intensity of the excitation source in the fiber. In the second case, excitation polarization is parallel to the aperture edge on which the tip rests (y-polarization) as shown in Fig. 2.3(b). Therefore, the source field has polarization that is parallel to the surface at the center of the exposed side of the tip. As a result, no SPP's are excited at the center. Instead, they are excited near two opposing ends of the tip's illuminated side, marked with white dotted circles in the Fig. 2.3(b). As they propagate toward narrowing tip, they destructively interfere with each other and no enhancement results at the apex. To clearly illustrate the evolution of SPP's polarization in both cases, the electric field vectors are plotted on the surface of the tip in Figs. 2.3(c) and 2.3(d) for the x- and y-polarizations respectively. In the case of x-polarization which results in strong localized field at the apex, the SPP's polarization is asymmetric (Fig. 2.3(c)) at the excitation site at the tip base. As they propagate along the tip, however, the electric field vector distribution becomes radially symmetric. The longitudinal z-component is also seen to be growing towards the apex and at the apex, the field is purely longitudinal. In contrast, for y-polarized excitation which results in no enhancement, the electric field vector distribution remains antisymmetric about the center plane all the way to the apex (Fig. 2.3(d)).

Next, we study the energy flow of SPP's that are excited with the perpendicular incident polarization in the case of Fig. 2.3(a) by plotting the Poynting vectors as cones on the surface of the tip overlaid with the map of logarithmic scale of electric field intensity in Fig. 2.4. The flow of optical energy is clearly seen by tracing along the Poynting vectors starting from the excited spots at the tip base on the illuminated side, marked with a red dotted circle in Fig. 2.4(a). From there the Poynting vectors wrap around the tip indicating that the plasmons spiral in both clockwise and counter-clockwise directions to the shadowed side of the tip (Fig. 2.4(c)) and then to the apex (Poynting vectors marked by the red dotted arrows as a visual guide for the reader). The orientation of the Poynting vectors along tip surface as seen from the top in Fig. 2.4(b) also suggests the double spiraling nature of SPP's.

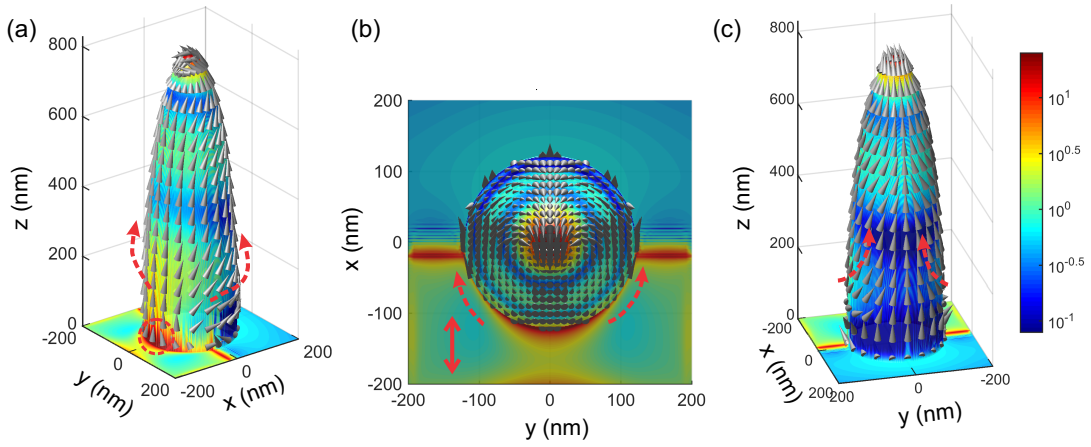

Fig. 2.4. The vector plot of the Poynting vector along the surface of the tip, overlaid with log scale map of electric field intensity to accentuate the standing wave-like intensity pattern, as viewed from (a) the illuminated side, where the tip's base is exposed to the incident light from the fiber, (b) top, and (c) shadowed side. The gray cones (vectors) are normalized to represent unit Poynting vectors. The red dotted circle in (a) marks the spots of excited SPP's. The red dotted arrows in (a), (b) and (c) indicate the direction of the spiraling plasmons. The red double-headed arrow in (b) indicates the polarization direction of the incident field from fiber.

The color contrast in the overlaid field intensity map in log scale in Fig. 2.4(c) also reveals a standing wave like maxima along the length of the tip. This suggests that the field enhancement that we observe at the apex is in part contributed by the open cavity resonance due to the finite tip size. To elucidate this phenomenon, we analyze the spectral dependence of field intensity enhancement along the tip. To this end, we find the maximum field intensity at each z-slice normalized with respect to the source intensity for a given excitation frequency and plot a hyperspectral map in Fig. 2.5(a) that contains both position and spectral information. The map gives a clear view of mode evolutions along the entire device. The bright horizonal band at $z = 0$ corresponds to the position of end-fire coupling from fiber core to plasmonic modes. The diagonal bands below $z = 0$ region results from the interference between forward and reflected fields inside the fiber. Bright undulating horizontal band at $z = 800$ nm comes from the focused plasmons at the apex giving rise to the field enhancement with peak intensities occurring at resonant frequencies corresponding to the modes of the cavity. The much fainter bands in the tip region ($0 < z < 800$ nm) are the signature of cavity modes. In Fig. 2.5(b), a single frequency slice of intensity enhancement is plotted for the resonant wavelength of 730 nm. At the apex, about 88-fold field intensity enhancement with respect to the intensity of the excitation source in the fiber is observed for the resonant wavelength of 730 nm. The spatial Fourier component of undulation along the tip is directly related to the wavenumber of the cavity mode [62]. In addition to the intensity maxima at the apex ($z = 800$ nm) and near the base of the tip ($z = 250$ nm), a third maximum can be observed near the middle ($z = 550$ nm). The three spatial maxima suggest that the 730-nm resonant peak in Fig. 2.5(a) is the second order mode [63]. The resonance wavelength changes with tip

length. We have plotted the spectral map and resonant frequency slice for a 600-nm-long tip in Figs. 2.5(c) and 2.5(d) respectively. The resonant peak at 875 nm exhibits two spatial field maxima, one at the tip apex and the other near the tip base, and thus the peak corresponds to the fundamental dipolar mode [63].

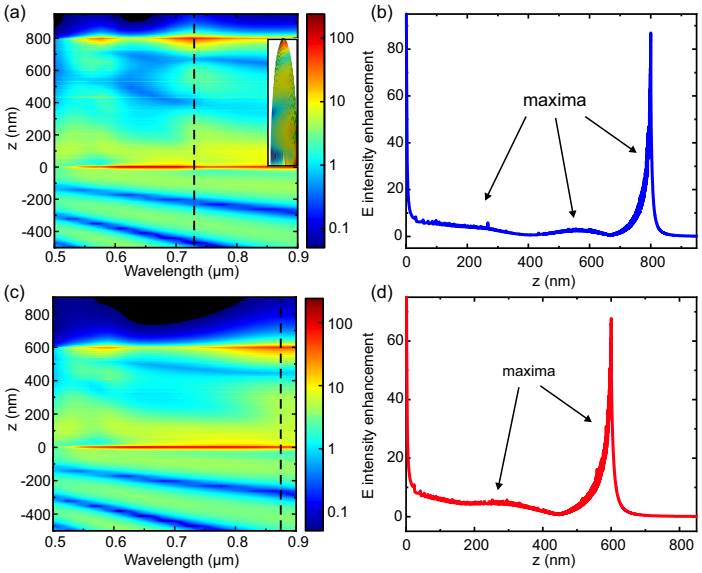

Fig. 2.5. The resonant nature of field enhancement. (a) Spectral map of maximum field intensity as a function of axial position along the fiber and 800-nm-long tip. The region where $z < 0$ is fiber core, $0 < z < 800$ nm is along the tip, and $z > 800$ nm is air. The inset figure is a visual guide for the position of the tip. The dashed vertical line marks a resonant frequency slice. (b) Single frequency slice from (a) at the resonant wavelength of 730 nm showing the z-dependence of the field intensity enhancement along the tip. (c) Spectral map for 600-nm-long tip on fiber. (d) Single frequency slice from (c) at the resonant wavelength of 875 nm.

To confirm the cavity mode's contribution, we calculate the spectral dependence of electric field magnitudes at the apex of four tips of varying lengths, 900, 800, 700 and 600 nm while keeping the same 240-nm-base diameter in Fig. 2.6(a). The second order resonant wavelength at 805 nm for 900-nm-long tip shifts to wavelengths of 730, 660 and 585 nm for tip lengths of 800, 700 and 600 nm respectively. Indeed, the resonant

frequencies increase with decreasing tip length, confirming the resonant field enhancements by the Fabry-Perot cavity mode [64-65]. The 136-fold intensity enhancement at the second order resonant frequency of 900-nm-long tip decreases to 88-, 46- and 28-fold for the tip lengths of 800, 700 and 600 nm respectively. The field enhancement becomes smaller with shorter tip length even though dissipative loss in the metal should be smaller for shorter propagation length. We attribute this apparent contradiction to the shape dependence of the radiative loss. Since the tips are half ellipsoid in shape, the shorter length implies larger and faster change of mode volume near the apex which leads to higher radiative loss. It should be noted that the enhancement values reported here are for second order resonances since the fundamental cavity modes of the tips are in the infrared, beyond the simulation bandwidth. The infrared regime would indeed benefit from higher field enhancement due to the fundamental resonant mode, as evident from the case of 600-nm-long tip whose fundamental resonance at 875 nm boasts 69-fold enhancement, in contrast to 28-fold enhancement at second-order resonance.

To quantify our device's performance, we calculate and plot the focusing efficiencies of four tips from the preceding discussion in Fig. 2.6(b). The focusing efficiency is defined as the ratio of the volume integral of electric field intensity over a small region at the apex above the tip surface extending 10 nm into air, with respect to the same quantity inside the core of the excitation fiber over a 10 nm length. Since this quantity is the ratio of energy available at the apex to input energy at the source, it provides a fair and precise assessment of our device. The focusing efficiency at resonant wavelength is 1.3% for a 900 nm tip with linearly polarized light. This is 2 to 3 orders better than 0.01 – 0.001% of aperture NSOM tips [66] while comparable to the 0.1 – 4%

performances of grating coupled tip [67-68] and 0.15 – 10% of gold coated fiber tips using radial mode excitation [14, 17, 69].

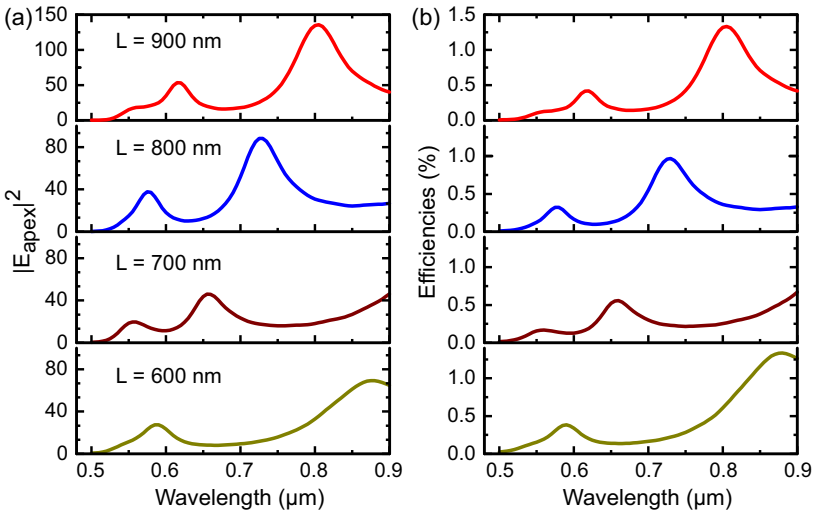

Fig. 2.6. The effect of tip size on enhancement. (a) The magnitude of the electric field at the apex as a function of excitation wavelength for varying tip lengths while the base diameter is kept constant at 240 nm. (b) The focusing efficiencies, as defined in the main text, as a function of excitation wavelength for the corresponding tips.

The analysis of our device that has been discussed so far concerns with the delivery of light from the fiber to the tip apex. Now we discuss the reverse scenario where the tip is used as a local probe to detect a radiating dipole. To investigate our device's detection performance, we perform a simulation in which an electric dipole whose orientation is aligned along the tip axis is placed 5 nm from the apex. The dipole near-field is coupled to the SPP's on the tip surface and then propagate towards the base as illustrated in Fig. 2.7(a). The scattered SPP's at the tip base is collected by the fiber and evolves into fiber core mode. Fig. 2.7(b) shows the intensity distribution of collected light inside the fiber 1.2 μm from the tip base. The collection efficiency is defined as the transmitted power into the fiber divided by the total dipole power. The transmitted power into the fiber is calculated after 1.2 μm of propagating in the fiber by integrating the z-

component of the Poynting vector over the cross-section of the fiber core. It should be noted that the coupled non-guided modes in the fiber decay strongly with propagation length and thus do not contribute to the collection efficiency. The total dipole power is the power transmitted through the cubic box of 8 nm side length, containing the point dipole source in its interior, calculated by integrating the perpendicular Poynting vector component over all six surfaces of the box. As plotted in Fig. 2.7(c), the collection efficiency is 5.1% at the 735 nm resonant frequency. The fine features in the field intensity profile in Fig. 2.7(b) and the oscillation of transmission curve in Fig. 2.7(c) is caused by the interference between the field that propagates along the tip as SPP's which later couples into the fiber and the field that propagates in free space which is transmitted through the aperture into the fiber. We estimate the latter's contribution by performing a simulation in the absence of the tip (Fig. 2.7(d)) and found to be one order of magnitude smaller than the total transmitted power into the fiber as shown in Fig. 2.7(e), which is significant enough to cause spectral beating through interference in Fig. 2.7(c) when the tip is present.

The unique contribution of our device lies in the ability to optimally convert the linearly polarized light into focusing radial plasmons, thus eliminating the needs for bulky and complicated polarization converters and specialty optical fibers. In addition, high efficiencies in both delivery and collection through incorporated flexible and broadband optical fiber make it attractive for applications in tip-enhanced Raman spectroscopy, near-field optical microscopy, biosensing, medical imaging and procedures, liquid, gas and temperature sensing. The focusing and collection efficiencies could be further enhanced by optimizing the tip/fiber geometries and materials. For

example, field enhancement can be optimized by choosing a combination of tip base and fiber core diameters that maximizes the mode overlap while minimizing the ohmic losses on the tip and leakage from the core. The tip length can also be tuned to balance the loss in the material absorption with the decreased radiative loss. Using other metals or conducting oxide materials whose absorption is lower than that of gold as the tip material (e.g. silver, ITO) will also contribute to higher device performance. The proposed nano-plasmonic antenna on optical fiber probe can be realized in practice by means of mature direct-write technologies such as ion beam or electron beam assisted metal deposition technique [70-71]. The fabricated probe can readily be implemented in a scanning tunneling microscope based Raman microscopes (STM-TERS) with the aid of fiber couplers or scanning near-field optical setups in shear-force feedback mode.

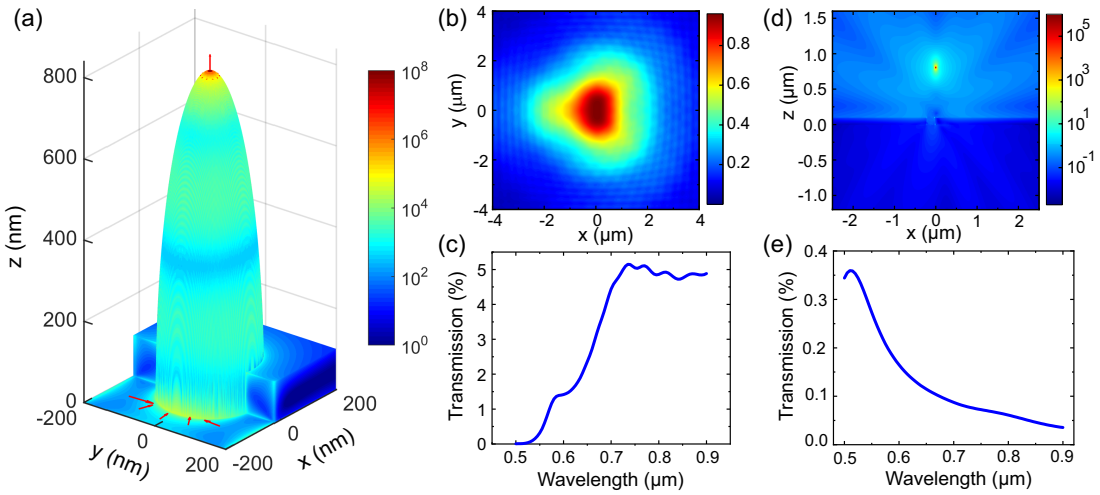

Fig. 2.7. Collection of radiation from dipole placed 5 nm above the apex of the 800 nm long tip (a) Electric field intensity distribution in log scale on the surface of the tip. The inset cartoon illustrates the location and orientation of the dipole. (b) The transmitted electric field profile on the cross-section of the fiber. (c) Transmission through the fiber normalized with respect to the source dipole power. (d, e) Collection efficiency in the absence of the tip. (d) The electric field distribution on the x-z plane going through the center of the fiber with the dipole source oriented along the axis of the fiber and light is collected into the fiber through the aperture on the fiber endface. (e) Transmission through the fiber normalized with respect to the source dipole power.

Conclusion

We demonstrate a photonic-plasmonic probe employing a novel excitation scheme that couples linearly polarized light from the optical fiber to radial plasmons on the plasmonic tip. We show that one-sided end-fire coupling asymmetrically excites surface plasmon polaritons that grow in intensity and focus to become radially symmetric plasmons as they propagate in a double spiral path towards the nanoscale apex. The cavity-like resonant response of the device allows the focusing and collection performance of the device to be optimized for a wide range of spectral positions by tuning the tip length. The focusing efficiency is comparable to the performances of other fiber tips excited using radial mode. The probe is a promising alternative to previously studied fiber-based probes due to its comparable performance while affording cheaper and more compact optical components when being incorporated into a near-field microscope.

Methods

Numerical simulations of the photonic-plasmonic probe were carried out using the FDTD Solutions software from Lumerical Solutions, Inc. In all simulations, permittivity function of silica and gold is modeled with a multi-coefficient function fitted to the Palik data [72] and Johnson and Christy data [73] respectively. Permittivity of GeO_2 doped silica (GeO_2 wt. 9% doped silica) is obtained from the literature [74]. The HE11 mode of the step index fiber is used as the input source. The perfectly match layers (PML) are used to minimize the scattered and reflected fields at the simulation boundaries, the symmetric boundary conditions (SBC) are imposed at the center plane to reduce the computation

time. Mesh size of 0.2 nm is employed in the region encompassing the tip for optimal convergence results.

CHAPTER THREE

Interfacing Photonic Crystal Fiber with Metallic Nanoantenna for Enhanced Light Nanofocusing

This chapter published as: K. Minn, B. Birmingham, B. Ko, H. W. H. Lee and Z. Zhang, Photonics Res **9** (2), 252-258 (2021).

Introduction

Optical fibers are the most broadly used optical waveguides and are essential components of broadband telecommunication. Efforts to expand their application beyond telecommunication have resulted in various fiber-based devices, including fiber lasers/nonlinear optics [75-76], biosensing and chemical sensing [77-78], optoelectronics [79] and in-fiber near-field imaging [9, 56]. On the other hand, surface plasmon polariton (SPP) waveguides have been studied extensively and have many applications in controlling and confining light in the nanometer scale such as plasmonic circuits [80], tip-enhanced Raman spectroscopy [81], nanoscale ultrafast spectroscopy [82], and quantum optics [83]. However, the propagation distance in plasmonic waveguide is largely hindered by the optical absorption by metals at visible and near infrared regime. Thus, efficient coupling of low loss photonic waveguide modes to the confined surface plasmon polariton and vice versa is necessary for practical plasmonic devices. To this end, plasmonic antennae and waveguides have been integrated with optical fibers in a number of configurations such as evanescent coupling of parallel waveguides [57-58, 84-85], end-fire coupling [19-20], tapered fiber to metallic nanotaper [86-87], aperture-assisted coupling [21-22], etc., achieving micro to nano scale light transport due to the adiabatic nanofocusing of SPP's. In those studies, integration of nanometer-sized antenna onto a micrometer-sized fiber is a fairly involved

process with multi-step procedures such as pressure-assisted high temperature melt-filling of metal inside the holey optical fiber followed by splicing/cleaving [84], fiber tapering and metal coating, chemical synthesis of nanowires followed by micromanipulation to form contact [85, 87], and electron-beam-assisted forming of 'contamination tip' on tapered fiber followed by metal coating [21], yet the precise control of the position and size of the antenna is difficult due to ad-hoc nature of the processes.

In this work, we report a simple and straightforward way of coupling photonic to plasmonic waveguide mode overcoming the difficulties mentioned above. The precise control of the position and size of the plasmonic antenna is achieved by directly writing a nanoscale metallic tip on fiber in single step inside a focused-ion and scanning electron microscope (FIB-SEM) chamber allowing for any fiber-antenna coupling configuration to be realized with high precision, in addition to high yield of designer 3D antenna with nanometer resolution. Our device can be described as a hybrid fiber-plasmonic probe, a coupled system of photonic crystal fiber (PCF) and metallic nano-antenna. A needle-like plasmonic nano-antenna is fabricated on the end facet of a PCF as shown in Fig. 3.1(a). The fundamental core mode of the PCF (Fig. 3.1(b)) is propagated through the fiber and coupled to the SPP mode on the platinum nano-antenna (Fig. 3.1(c)) via end-fire coupling. Such direct coupling relaxes the phase matching requirement, enable broadband coupling and reduces propagation losses [19]. The coupled SPP's then propagate along the antenna toward the tapered end where they converge to produce highly enhanced and confined field at the nanoscale apex.

Results and Discussions

To confirm the practicality of our device, we fabricate a platinum tip on the end facet of the PCF using electron beam induced deposition (EBID), a direct-writing technique capable of creating three-dimensional complex structures with high-resolution [88-89]. The PCF is chosen over the step-index fiber because of single mode transmission over a broad bandwidth covering visible and near infrared [90]. The modal confinement of PCF can be designed as small as ~1 μm for efficient coupling. Moreover, the presence of air-hole cladding makes it easier to align the plasmonic antenna in the core during fabrication. In this technique, metallo-organic precursor gas is introduced near the surface of the PCF facet through the injection nozzle as shown in the inset of Fig. 3.2(a). PCF facet is pre-coated with thin layer of gold to avoid charging (see Methods for details.) Then the focused electron beam is scanned over a circular area. When the electron beam

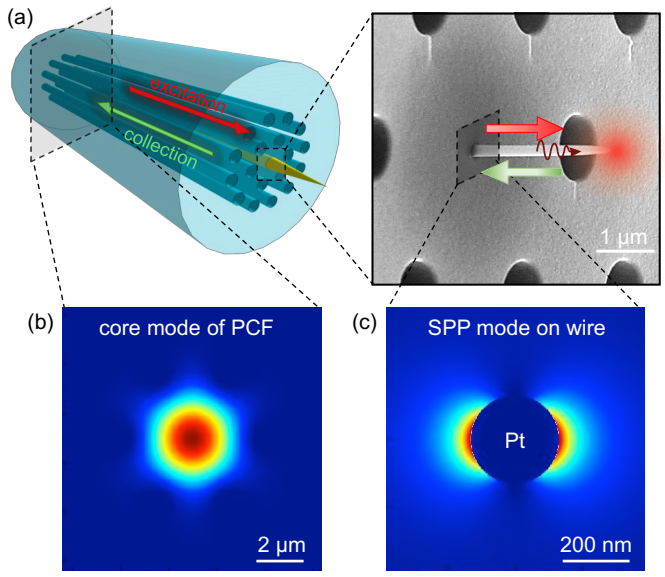

Fig. 3.1. The PCF-nanoantenna hybrid probe. (a) Schematics of the device. (b) Simulated intensity profile of fundamental guided mode in the PCF at 560 nm wavelength. (c) Simulated intensity profile of HE_{11} mode on metallic nanowire waveguide at the same wavelength.

interacts with the gas, the volatile organic molecules evaporate, and the metal part adsorbs on the surface forming a thin metal disc [70, 88]. The structure becomes taller with increasing number of passes. At the same time, deposited metal at each new pass spills over the edge resulting in the cone shaped tip formation at the top of the structures. This process is repeated until a conical pillar with the desired height is formed. The width of the deposited structure is slightly larger than the electron beam scan area. Primary electrons scattering and outgoing secondary emissions occur over an area much larger than the beam spot size [91]. Therefore, smallest width is limited by the resolution of the scan area. Nanowires with different lengths and diameters have been fabricated for this study. The SEM images of some of the fabricated tips are shown in Fig. 3.2(b-e). The inset of Fig. 3.2(b) shows the high-resolution SEM image of the tip apex. The radius of curvature at the tip apex is less than 14 nm. The tip radius of our fabricated samples ranges from about 14 to 40 nm. The tip radius of the sample on Fig. 3.2(d) is about 19 nm and Fig. 3.2(e) 26 nm. The details of the fabrication parameters and the sizes of the tips can be found in the Methods section. The results from optical measurements of the two samples in Fig. 3.2(d) and 2(e) are discussed below.

To demonstrate the light coupling and focusing performance of our nano-probe device, we chose a representative tip from among the fabricated samples. It has height of 2.353 μm and diameter of 164 nm at the center of a PCF with a 5 μm core diameter (Fig. 3.2(d)). A 30 nm of gold layer is coated on the PCF to avoid charging during the nanowire fabrication while allowing light to be transmitted through the fiber end. We performed optical characterization of the fabricated tip by imaging the scattered light to

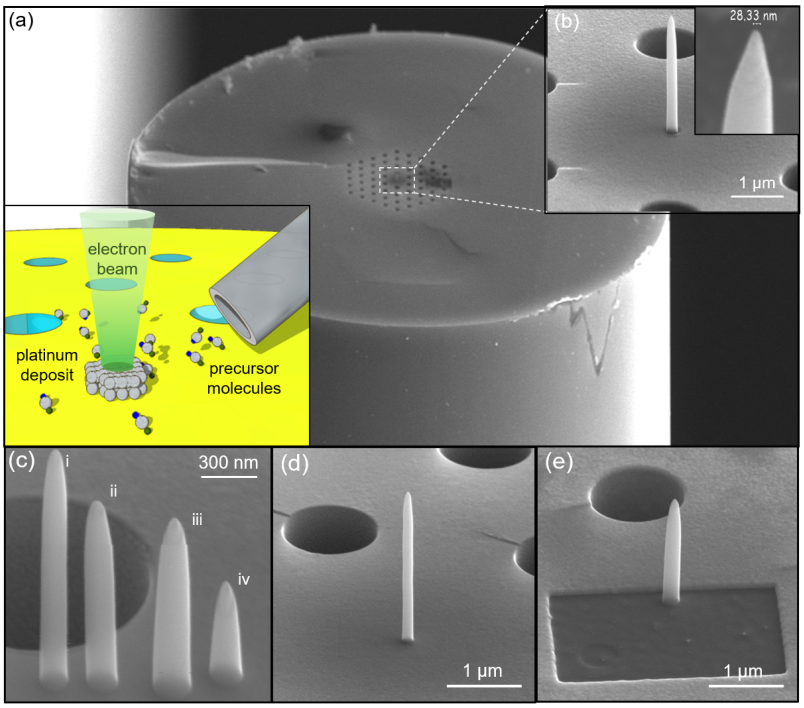

Fig. 3.2. The device fabrication with electron beam induced deposition (EBID). (a) Schematics of the EBID process and overview SEM image of PCF. (b-f) SEM images of the fabricated samples on PCF's taken at 52-degree inclination. The deposition parameters, base diameter and height of each tip is tabulated in Methods section.

the side of the tip. The side-scattered light is imaged in the far-field using the setup illustrated in Fig. 3.3(a). The light source from the super-continuum laser is free space coupled to the bare end of the PCF. At the other end with the plasmonic tip, an objective (60x magnification and 0.9 NA) is placed to collect the light scattered to the side of the tip to be imaged on the charged coupled device (CCD) after going through a polarizer and a bandpass filter having 10 nm full width at half maximum centered at 530 and 630 nm. For the sample shown in Fig. 3.3, input power of 402 mW is used, and for the sample in Fig. 3.5, 10 mW. Most of the tips were not damaged at low input power, confirmed by inspecting with SEM. The tip in Fig. 3.5 is found to withstand up to 240 mW.

The excitation of SPP's on the tip can be verified by analyzing the polarization of light that scatters to the side of the tip. In Fig. 3.3(c) and 3.3(e), when the output polarization analyzer is oriented along the antenna axis to collect the longitudinal component of scattered SPP, the intensity is much brighter than the case when the analyzer is oriented perpendicular to antenna axis (Fig. 3.3(d) and 3.3(f)) to collect the transverse component. The linearly polarized PCF core mode cannot efficiently excite radially symmetric SPP (TM0) mode on the metal tip because of modal field mismatch. The first order SPP (HE1) mode polarized along x-axis exhibits antisymmetric electric

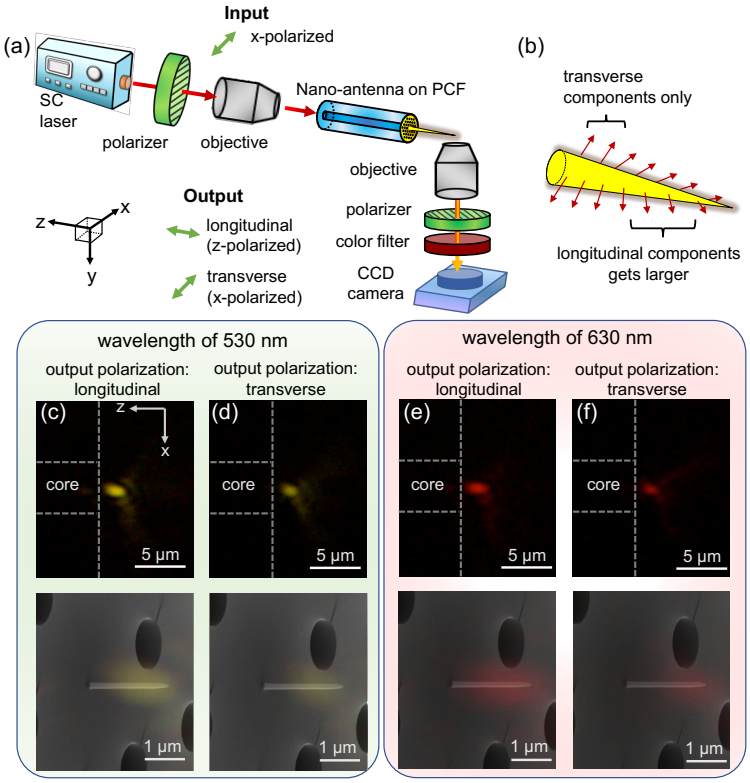

Fig. 3.3. The Fiber coupling and the polarization resolved imaging of side-scatter light. (a) schematics of the optical setup. (b) illustration of SPP vector components along the tip. (c-f) the optical images of the side scattering from the tip when the output polarizer is (c), (e) along the tip axis (longitudinal), and (d), (f) perpendicular to the tip axis (transverse). (b) and (c) is taken with 530 nm filter. (d) and (e) is taken with 630 nm filter. The dashed lines are the visual guide for outline of the PCF. The bottom panel is the SEM image overlaid on the optical image.

field distribution about y-axis [92-93], and can be excited with the linearly polarized incident core mode from PCF. However, at the mode cut-off radius, when the effective index of the mode approaches the index of air, it couples to the far-field radiation and thus could not focus down to the apex of the nanowire [93-94]. In this case, we expect to see stronger scattering of transverse than longitudinal component as depicted in Fig. 3.3(b). However, with a small asymmetry in the shape of the tip such as a slight tilt, phase difference between the two counter-propagating modes of the tip could be introduced, allowing a portion of the optical energy to be coupled to radially symmetric SPP (TM_0) mode [22, 95]. The tapered geometry of the tip forces radial SPP to slow down and asymptotically converge toward the apex [96]. As they do, the longitudinal component of the SPP becomes larger and the transverse component is suppressed. As a result, the light that scattered to the side from the apex has mostly longitudinal component. Evidently, the side-scattered light is composed mainly of longitudinal components as seen in Fig. 3.3(c) and 3.3 (e) suggesting that the SPP's are focused near the tip apex where they scatter to far field. However, there still exists transverse component in the scatter light as shown in Fig. 3.3(d) and 3.3(f) which implies that the SPP's scatter before they reach the apex. To avoid coupling to the leaky mode and improve the asymmetrical coupling of the linearly polarized light with the tip, we modify the coupling conditions at the fiber-tip interface by introducing a metallic aperture close to the nanowire.

To improve the focusing efficiency of the device, we fabricate a probe with a rectangular aperture at the tip-PCF interface. In this device, PCF is coated with 100 nm Au to block the transmitted light. A 3×4 μm^2 aperture is milled with focused-ion-beam at the center of the core. Afterwards, the tip is fabricated inside the aperture next to one of

the long edges of the aperture as shown in the Fig. 3.2(e). The modes supported by the aperture and tip system is calculated by finite element method and plotted in Fig. 3.4. In Fig. 3.4(a), the input polarization is parallel to the gap between the tip and the edge of the aperture, which we refer to as x-polarization for simplicity. The aperture shifts the spatial distribution of electromagnetic fields that is coupled to the tip mostly to the exposed side, the side that opens out to the center of the core. On the side that forms a gap with the wall of the aperture, the field does not couple to SPP. This asymmetric or one-sided coupling of SPP's on the tip evolves to radial SPPs which can propagate to the apex resulting in nano-focusing as shown in Fig. 3.4(b). It shows the intensity enhancement factor of about 24 at the tip apex compared to the fiber core. The inset of Fig. 3.4(b) shows the focusing efficiency for x-polarization, defined as the ratio of the electric field intensity integrated over a small region at the apex above the tip surface extending 10 nm into air with

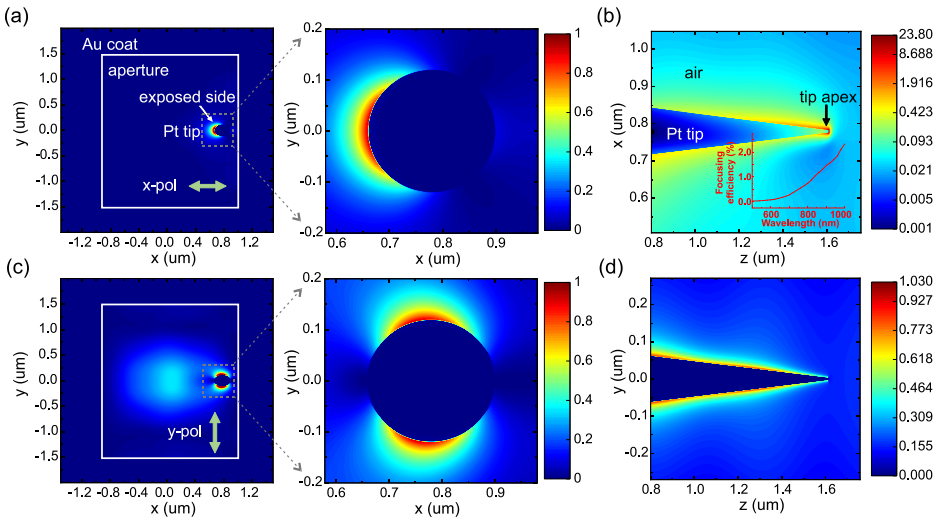

Fig. 3.4. The effect of rectangular aperture on mode coupling. (a) The electric field intensity profile of the aperture-tip geometry and (b) the propagation along the tip producing nanofocusing at the apex for x-polarized light. The color bar represents the field intensity normalized with respect to excitation intensity. Inset: focusing efficiency as a function of wavelength. (c, d) Same as (a, b) but for y-polarization with fields canceling near the apex. The green arrows in (a) and (c) indicates the input polarization.

respect to the same quantity inside the core of the excitation fiber. The efficiency in the near-infrared is about 2.3%, while it is about 0.1% in the visible. The low efficiency in the visible is due to the lossy nature of Pt and can be improved by using Au or Ag as the plasmonic tip material as well as tip size. The nanofousing via asymmetric coupling has been thoroughly investigated theoretically and reported by our group in the previous study [22]. In Fig. 3.4(c), the input polarization is perpendicular to the gap between the tip and the aperture wall, which we refer to as y-polarization. In this case, the distribution of SPP modal field around the tip remains anti-symmetric about the x-axis. As they propagate toward narrowing tip, they destructively interfere with each other and no enhancement results at the apex as shown in Fig. 3.4(d).

Figure 3.5(a) and 3.5(b) respectively show the measured optical image of side-scattered longitudinal and transverse components from the aperture-antenna when the input is x-polarized. In this polarization, the asymmetric mode discussed above in Fig. 3.4(a) is excited at the tip base and SPP's can focus on the apex. From the images, the side scattered light is seen to be purely longitudinally polarized implying that it originates from focused SPP's. To confirm that the strong longitudinal scattering is solely from the tip and not from the aperture edges, we prepare a control PCF sample with only an aperture. When the tip is absent, as shown in Fig. 3.5 (c) and 3.5(d), the scattering from the aperture has weaker longitudinal component than transverse in addition to having large spatial extent, confirming that the scattering of longitudinal components in Fig. 3.5(a) is from the tip, not from the aperture. We note that scattering from the aperture has stronger transverse component because the input x-polarization aligns with the transverse orientation of the output.

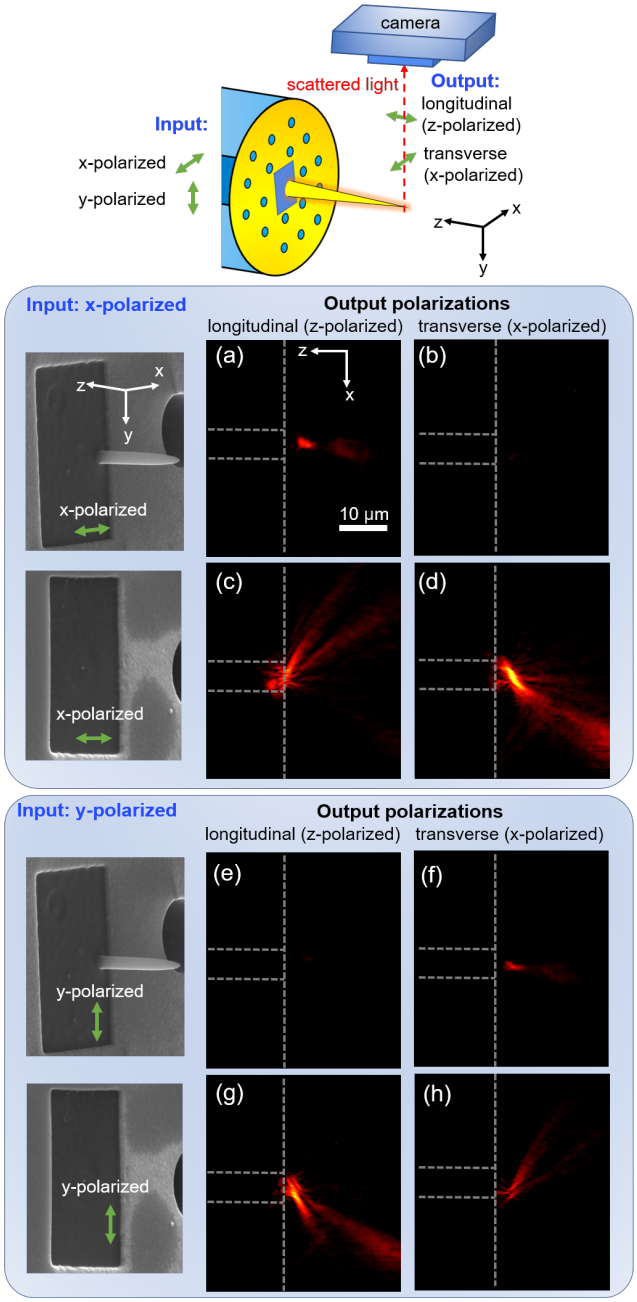

Fig. 3.5. Side-scattering from PCF-aperture-antenna system. (a-d) the optical images of the side scattering from the tip when the input polarizer is parallel to the gap between the tip and aperture-wall, with the output polarizer (a),(c) along the tip axis (longitudinal), and (b), (d) perpendicular to the tip axis (transverse). The tip is present in (a) and (b), while it is absent in (c) and (d). (e-f) scattering from the tip when the input polarizer is perpendicular to the gap between the tip and aperture-wall, with the output polarizer (e),(g) along the tip axis and (f), (h) perpendicular to the tip axis. The tip is present in (e) and (f), while it is absent in (g) and (h). Scale bar: 10 μm is for all optical images. The green arrows in the SEM images of the samples on the left panel indicate the orientation of input polarization in the plane of the aperture.

Next, we rotate the input polarization by 90 degree so that the PCF mode is y-polarized. At the fiber-tip interface, the fiber core mode couples to the y-polarized antisymmetric SPP mode discussed in Fig. 3.4(c) and 4(d). As such, the coupled SPP's on the opposing sides of the tip destructively interfere with each other as the tip radius narrows and scattering occurs without focusing at the apex. As a result, the longitudinal component is weaker than the transverse as shown in the side scatter images in Fig. 3.5(e) and 3.5(f). In contrast to Fig. 3.3(c-f), where an accidental tilt of the tip is invoked to justify the experimental results, the introduction of aperture allows us to confirm the SPP focusing by the control of the input polarization. For the control sample with aperture only, it is seen in Fig. 3.5 (g) and 3.5(h) that the scattered light from the aperture has stronger longitudinal component than the transverse, confirming that the scattering in Fig. 3.5(f) is from the tip and not from aperture. We again note that when the incident beam from PCF is y-polarized, the light that is scattered from the aperture toward the detector is polarized along the y-z plane. Thus, the detected light contains more longitudinal (z-polarized) component than transverse (x-polarized).

The demonstrated input-polarization selectiveness of the device shows that the aperture clearly modified the light coupled to the plasmonic tip. For x-polarized input, the light scattered from the tip contains no transverse component indicating higher focusing performance. The aperture and tip parameters such as the width, height, gap size, etc., can be optimized to further increase the coupling and focusing efficiencies as well as the suppression of background scattering from the fiber core. In our previous work employing similar coupling mechanism, we reported 136-fold field enhancement and 1.3% focusing efficiency [22], which is better or comparable to the performance of existing

nearfield probes [17, 66, 68]. The PCF core size is also an important factor that determines the focusing efficiency. Since the modal field overlap between the core mode and the nanowire plasmonic mode determines the coupling efficiency of in the end-fire coupling scheme, the core diameter should be at least in the same order of magnitude as the nanowire diameter. On the other hand, as core size becomes smaller, the free space coupling loss into the fiber as well as the attenuation along the fiber becomes large. In this work, we use the smallest core size PCF that is commercially available that has low attenuation over a broad bandwidth. Metals with larger real part of permittivity and less absorption than platinum such as gold and silver can also be used as the tip material for improved performance; however, the precursor for those metals often results in residual carbon impurity during deposition and thus Pt is preferred for applications related to FIB-SEM machining. Alternatively, a thin layer (~50 nm) of Au or Ag can be deposited on the Pt tips by sputtering or evaporation techniques to mitigate the losses of Pt, but the optimization of the device is beyond the scope of the current study. We believe that with judicious choice of parameters mentioned above, our device provides a unique and efficient tool to study nanoscale light-matter interaction such as fiber-based tip-enhanced Raman and fluorescence spectroscopies.

Conclusion

We demonstrate a photonic-plasmonic probe employing a straightforward excitation scheme that couples linearly polarized light from the optical fiber to nano-focusing plasmons on the plasmonic tip aided by an aperture at the fiber-tip interface. As a proof of concept, PCF-nanoantenna probes are fabricated and optically characterized. We showed that when the input polarization is in the direction where aperture-tip

geometry is asymmetric, the scattered light from the antenna is longitudinally polarized which confirms the plasmonic coupling and nano-focusing.

Methods

Numerical Simulation

Numerical simulations of the photonic-plasmonic probe were carried out using the MODE Solutions and FDTD Solutions software from Lumerical Solutions, Inc. Permittivity function of silica and platinum is modeled with a multi-coefficient function fitted to the Palik data [72], and gold Johnson and Christy data [73]. PCF is modeled as hexagonal lattice (lattice constant 3 μm) of air holes (diameter 1.25 μm) in silica core with one defect at the center. Mesh size of 2 nm is employed in the region encompassing the tip for optimal convergence results.

Tip Fabrication

One end of the PCF (PMA-LM-5 from Thorlabs Inc.) is mechanically cleaved to have a clean and flat end surface which is then coated with gold layer of thickness 30 nm for the sample in Fig. 3.3 and 100 nm for the one in Fig. 3.5 using magnetron sputtering. Then the gold coated PCF is loaded into the microscope chamber vertically. Depositions were performed in a focused ion and electron beam system (Versa 3D from FEI company). The acceleration voltage of 30 kV and beam current of 140 pA is used. Platinum precursor gas (Trimethyl [(1,2,3,4,5-ETA.)-1 Methyl 2, 4-Cyclopentadien-1-YL] Platinum) is injected into the vacuum chamber near the fiber. The e-beam exposure begins when the chamber pressure stabilizes around 1.3×10^{-5} mbar.

Table. 1. The EBID deposition parameters and corresponding tip dimensions.

Scan diameter (nm)	Dwell time (μs)	Passes	Total time (s)	Base diameter (nm)	Height (μm)	Corresponding figure
75	1	1343069	32	167	0.950	Fig. 3.2(c). iii
75	1	2166241	52	146	1.263	Fig. 3.2(c). i
75	1	4332482	104	164	2.353	Fig. 3.2(d)
100	1	4332482	13	173	0.561	Fig. 3.2(c). iv
100	1	1083121	32	190	1.098	Fig. 3.2(c). ii
100	2	1126445	65	216	1.060	
100	2	1689668	98	241	1.610	Fig. 3.2(e)
100	2	2166241	126	237	1.953	

The physical dimensions of the tip such as height and width of the tip can be adjusted by controlling the dwell time and the number of passes. In Table 1, we list the deposition parameters and the resulting physical dimension of a few of the fabricated tips. By changing the scan diameter, which is the diameter of the circular area over which the focused e-beam is scanned during deposition, from 75 nm to 300 nm, the base diameter of the tip is tuned from 150 to 540 nm (only the scan diameters up to 100 nm and tip base diameters up to 241 nm is listed in Table. 1). The height of the tip can be tuned by varying the number of passes, but special care needs to be taken since the increasing passes will also widen the tip. For optimal resolution and aspect ratio, a small e-beam current of 140 pA and short dwell time is used, resulting in high number of passes (~10^6). Dwell time of 2 μs results in higher aspect ratio than dwell time of 1 μs. To show the reproducibility of our fabrication technique, five tips are fabricated using the same

deposition parameters as the tip in Fig.2(e). The standard deviation of the resulting tips' base diameter is 10 nm (or 5% of the mean) and height 200 nm (or 10% of the mean).

Optical Measurements

The optical measurements are carried out using the setup illustrated in Fig. 3.6. The light source from the super-continuum laser is free space coupled to the bare end of the PCF after passing through a polarizer. The scattered light from the other end of PCF is collected with an objective (60x magnification and 0.9 NA) aligned perpendicular to the fiber axis. The scatter light is imaged on the charged coupled device (CCD) after going through a polarizer and a bandpass filter having 10 nm full width at half maximum centered at 530 and 630 nm.

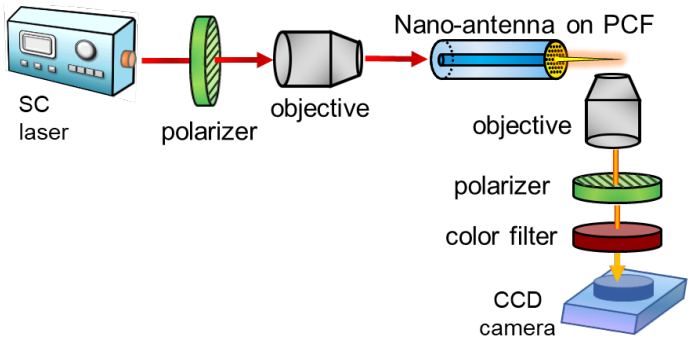

Fig. 3.6. The schematics of the optical setup for fiber coupling and the polarization resolved imaging of side-scatter light.

CHAPTER FOUR

Excitation of Epsilon-Near-Zero Resonance in Ultrathin Indium Tin Oxide Shell Embedded Nanostructured Optical Fiber

This chapter published as: K. Minn, A. Anopchenko, J. Yang and H. W. H. Lee, Sci Rep-Uk **8** (1), 2342 (2018)

Introduction

Optical response of near-zero refractive index systems has been a topic of interest recently as the electromagnetic field inside the media with near-zero parameters, i.e., vanishing permittivity and permeability values, have been shown to exhibit unique optical properties. Those features may be exploited in various optical applications such as wavefront engineering, radiation pattern tailoring [97-98] , non-reciprocal magneto-optical effects [99], nonlinear ultrafast optical switching [32, 100], dielectric permittivity sensing [101-102], and broadband perfect absorption [23, 103]. Recent studies suggest that epsilon-near-zero (ENZ) properties can also be observed in a single highly doped conducting oxide thin film. Unique properties observed include enhanced absorption in transparent conducting oxide (TCO) ENZ layers [23-26, 104], advanced resonant coupling properties with antenna [3, 27-28], and strongly enhanced nonlinear response and light generation in a TCO slab [29-33]. In addition, electrical tuning of conducting oxide materials to the ENZ regime results in efficient light manipulation and modulation [34-36]. However, most of the studies on ENZ optical properties are limited to the excitation of ENZ mode in the planar structures or meta-surfaces with short interaction length, restricting the excitation platform for novel optical applications.

Photonic crystal fiber (PCF) or micro-structured optical fiber consists of hollow channels running along the entire length of a glass strand, providing unique platform with long interaction length and engineerable dispersion for the studies of nonlinear optics, optical communication, optical/bio sensing, etc [105]. The optical properties of PCFs can be changed by filling the hollow channels with materials such as semiconductors and metals to excite the Mie resonances and surface plasmon resonances[52, 58]. Those metal/semiconductor infiltrated fibers have been proposed to use for optical sensing and in-fiber device applications. Simplified version of photonic crystal fiber with enhanced light-matter interaction could be achieved by introducing a nanoscale hollow channel into conventional optical fiber (e.g., nanobore optical fiber). Such nanobore fiber further allows the light coupling to the plasmonic modes of gold nanowire for polarization conversion [106] and optical detection of virus in nano-fluid channel [107].

In this work, we investigate the ENZ mode excitation in optical fiber platform and demonstrate that propagating fields can be confined inside a region coated with ENZ conducting oxide material which is incorporated into a nanostructured optical fiber waveguide. The novel hybrid optical fibers could be used as a platform for highly sensitive optical sensing and magneto/nonlinear-ENZ optical studies.

The ability to confine electromagnetic energy in a small space at the medium's ENZ wavelength motivates a search for highly confined propagating polariton modes using ENZ materials. It has been experimentally shown that three layer structures, where a sub-wavelength thin layer of indium tin oxide is sandwiched between two dielectric layers, can support ENZ polariton modes [3-5]. Here we present the existence of propagating mode in an optical fiber with nano-hollow channel modified with an ENZ layer within which

enhanced field is excited. Our proposed ENZ fiber waveguide design is a modified version of nanobore fiber which consists of three concentric cylindrical shells (Fig. 4.1). The two outermost shells act as cladding and core respectively. The innermost thin shell is made of ENZ material that surrounds the hollow central channel. The sub-wavelength thickness of ENZ shell ensures that the guided core fiber mode can be coupled to the thin film ENZ mode whose domain of existence is limited to film thickness much less than the plasma wavelength of the material at which its permittivity vanishes [104].

Results and Discussions

Indium-tin-oxide (ITO), a CMOS compatible TCO material, is used as the ENZ medium in the analysis. The real part of ITO permittivity crosses zero at the bulk plasmon resonant wavelength, which can be tuned in near-infrared by controlling the carrier concentration of the material [108]. The frequency dependent complex permittivity of ITO was calculated using the Drude model. (See ITO material and optical properties in *Methods* and Appendix A). For the designed ITO carrier concentration of 10^{21}, the real part of permittivity function of the ITO crosses zero at 1068 nm and with small imaginary part of permittivity ($Im(\varepsilon) = 0.41$). This carrier concentration of ITO could be achieved by various deposition techniques, for instance magneton sputtering and atomic layer deposition (ALD) [35-36, 108-110]. ALD or wet chemistry techniques could be used to fabricate conducting oxide nano-shell inside the hollow channel of the fiber[110-112].

To understand the coupling mechanism between the guided mode in the nanobore fiber and the thin film ENZ mode, we investigate their dispersion characteristics. The effective index of the fundamental guided core mode of the nanobore fiber as a function of excitation wavelength was modelled using finite difference numerical waveguide

analysis method (see *Methods*). The effective index of non-radiating thin film ENZ mode supported by the glass-ITO-air three layer structure was modelled using the transfer matrix method (see *Methods*). The coupling between the fundamental mode of the nanobore fiber and thin film ENZ mode occurs at the phase matching wavelength, at which point the effective index functions of the two modes intersect and their momenta are equal. Our results show that at the phase matching wavelength, the field confinement inside the ITO shell in the ENZ fiber is the highest and the mode has the highest loss, thus confirming the excitation of thin film ENZ mode in the fiber structure.

A schematic of the proposed ENZ optical fiber design is shown in Fig. 4.1(a). Section (I) of the structure is the hollow nanobore fiber which consists of the outer silica cladding, GeO_2 wt. 9% doped silica core of 4 μm diameter and a hollow central channel of 200 nm diameter. Section (II) depicts the ENZ fiber where the inner surface of the central hollow channel is coated with 10nm layer of ITO. Figure 4.1(b) shows the glass-ITO-air three layer structure that is considered in calculating the thin film ENZ mode. The structure is comprised of a thin ITO layer having the same thickness as the ITO shell inside the ENZ fiber sandwiched between the air and glass half spaces.

The dispersion of fundamental mode of the hollow nanobore fiber was obtained using finite difference numerical waveguide simulations on the cross-section of the nanobore fiber as depicted in the right insert of Fig. 4.1(a). A frequency dependent real part of the effective index of the mode n_{eff} was calculated ($n_{eff} = c\beta/\omega$, where β is the propagation constant in the fiber for a given wavelength). To obtain the dispersion curve

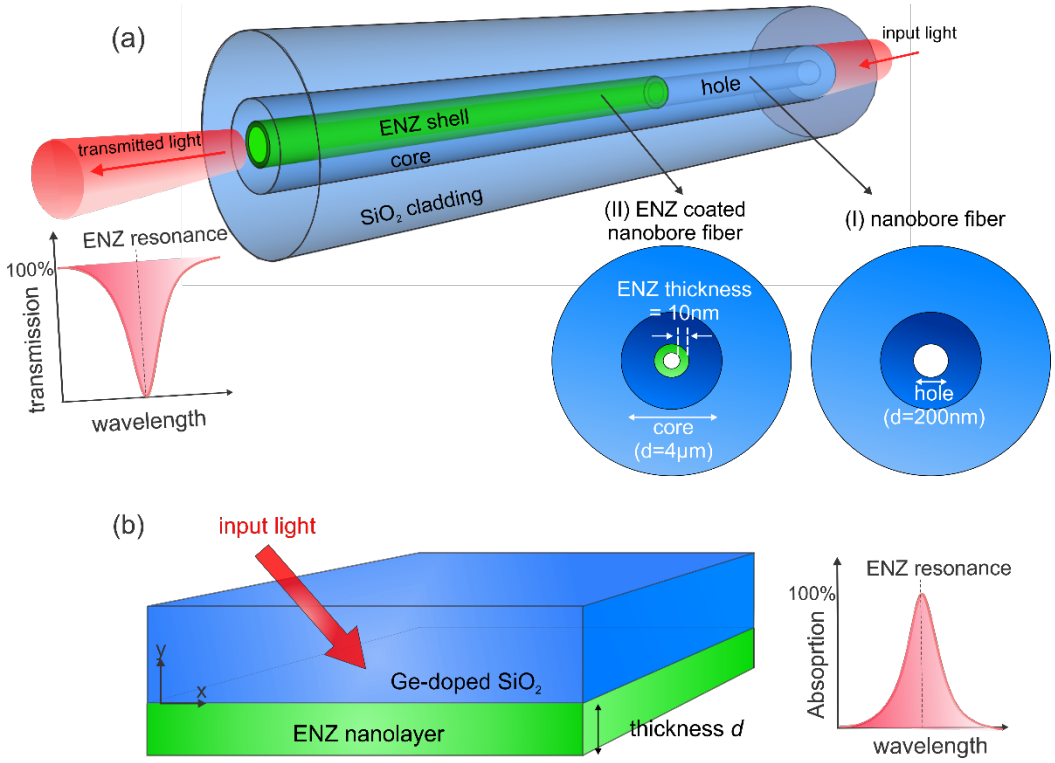

Fig. 4.1.(a) Schematic of the proposed ENZ fiber waveguide design. The inserts are cross-sections of the ENZ fiber (coated with ITO ENZ nano-shell) and hollow nanobore fiber (without ITO ENZ nano-shell). (b) Geometry of glass (GeO2 doped silica)-ITO-air three layer structure with ITO layer thickness d for excitation of NR-ENZ thin film mode.

of the thin film ENZ mode, we investigated the glass-ITO-air three layer geometry shown in Fig. 4.1(b) using the transfer matrix method. To ensure the excitation of the non-radiative ENZ mode, the ENZ mode is excited from the glass half space using Kretschmann configuration [113]. The reflectance was calculated for varying incident angles and wavelengths. For small enough thickness of ITO layer ($d < \lambda/50$), light incident from glass onto ITO nanolayer is perfectly absorbed at large angles and at resonant wavelength which corresponds to the ENZ polariton mode [3]. Thus for each incident angle, the wavelength that corresponds to minimum reflectance is traced to calculate the effective index of the thin film ENZ mode (see Fig. A.3. in Appendix A). The thin film

ENZ dispersion curves for 5 nm, 10 nm, 15 nm, and 20 nm ITO layer thicknesses were calculated to show that the phase matching condition with fiber core modes depends on the thickness of the ITO layer.

To understand the phase matching condition, the effective index of the thin film ENZ modes for four different ITO layer thicknesses (dash curves) and the fundamental mode of hollow nanobore fiber (blue dotted curve) were calculated and depicted in Fig. 4.2. As the ITO thickness increases, the thin film ENZ dispersion curve shifts toward longer wavelengths and thus the phase matching wavelength (crossing wavelength) with the fiber core mode. Thin film dispersion curves intersect the fiber core mode dispersion at 1070 nm, 1079 nm, 1088 nm and 1098 nm wavelengths for 5 nm, 10 nm, 15 nm and 20 nm ITO layer thicknesses respectively. Thus in the ENZ fiber, ENZ mode is expected to be excited at higher wavelengths for thicker ITO shells.

As a next step, we verified the excitation of ENZ modes in the fiber at the above resonant wavelengths. Finite difference method was used to solve the Maxwell's equations on a cross-section of the ENZ fiber waveguide. The resulted fundamental mode has highest spatial field distribution within the ITO shell compared to higher order modes. This ENZ mode was tracked over a wavelength range to calculate the modal loss ($loss = -20log_{10}e^{-2\pi k/\lambda_0}$, where k is the imaginary part of the effective index). The modal loss curves were calculated in the same way for four different ITO shell thicknesses: 5 nm, 10 nm, 15 nm and 20 nm. Figure 4.2 shows the modal losses of the fundamental mode of the ENZ fiber for four ITO shell thicknesses (color shaded areas). Peak losses are observed at wavelengths 1071 nm, 1080 nm, 1092 nm and 1102 nm for ITO shell thickness 5 nm, 10 nm, 15 nm and 20 nm respectively. These resonances are in

good agreement with the phase matching wavelengths of the nanobore fiber mode and the thin film ENZ modes calculated above. The peak in the loss spectra is resulted from the excitation of ENZ thin film mode and the strong confinement/absorption by the ITO nanolayer.

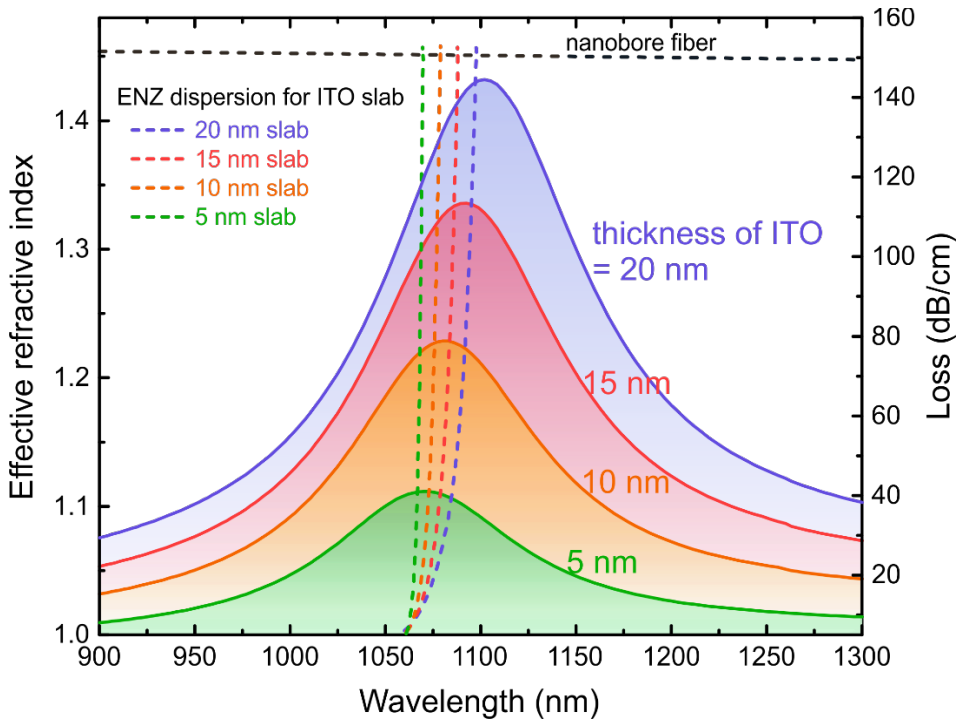

Fig. 4.2. Phase matching conditions between fundamental waveguide mode in the hollow nanobore fiber and thin-film NR-ENZ mode of glass-ITO-air three-layer geometry for 5 nm, 10 nm, 15 nm and 20 nm ITO layer thicknesses. The dotted curves are effective refractive index of waveguide and thin-film modes as a function of wavelength. The solid curves and color shaded areas are modal loss spectra of fundamental mode excited in the ENZ fiber for four ITO shell thicknesses described above.

The slight discrepancy between the phase matching and the peak loss wavelengths can be attributed to the mismatch between the excitation light sources: plane wave in the case of three layer geometry and core guided eigen-mode source in the nanobore fiber. Another contributing factor is the curvature of the ITO shell inside the fiber which is cylindrical in contrast to the flat geometry of three layer structure that is assumed when

calculating the thin film ENZ modes. The resonance discrepancy is greater with increasing shell thickness due to the mismatch in the two geometries. To study the nature of ENZ mode in the fiber, we plot the spatial electric field distributions of the fundamental mode supported by the ENZ fiber with 10 nm thick ITO shell at the ENZ wavelength and off-ENZ wavelength (Fig. 4.3). The field distribution does not exhibit radial symmetry because the excitation fiber core mode is linearly polarized (HE_{11}). The radially polarized higher order mode (TM_{01}) is not supported by the nanobore fiber at the high wavelength regime (Appendix A.2). At 1080 nm, which is the ENZ mode phase matching wavelength for 10 nm thick ITO layer, magnitude of electric field is highly confined inside ITO shell (ENZ region) as shown in Fig. 4.3(b) and (e). The high field confinement in the ENZ nano-layer results in the highest modal loss at this wavelength as seen in Fig. 4.2 (yellow solid curve). At shorter wavelength (900 nm), the refractive index of ITO resembles that of a dielectric with real part of value (n = 1.022) falls between that of air at the center and doped silica core (n = 1.459) (Appendix A.1). In this regime, the field distribution resembles the profile of the fundamental mode of hollow nanobore fiber as can be observed in Fig. 4.3 (a) and (d). At longer wavelength (1300 nm), ITO is in essence metallic-like having negative real part of permittivity ($\varepsilon = -1.707 + 0.732i$) with real part of index (0.274) smaller than imaginary part (1.335). Thus, the field is mostly contained in the core and central air channel, decaying inside the ITO shell as depicted in Fig. 4.3(c) and (f).

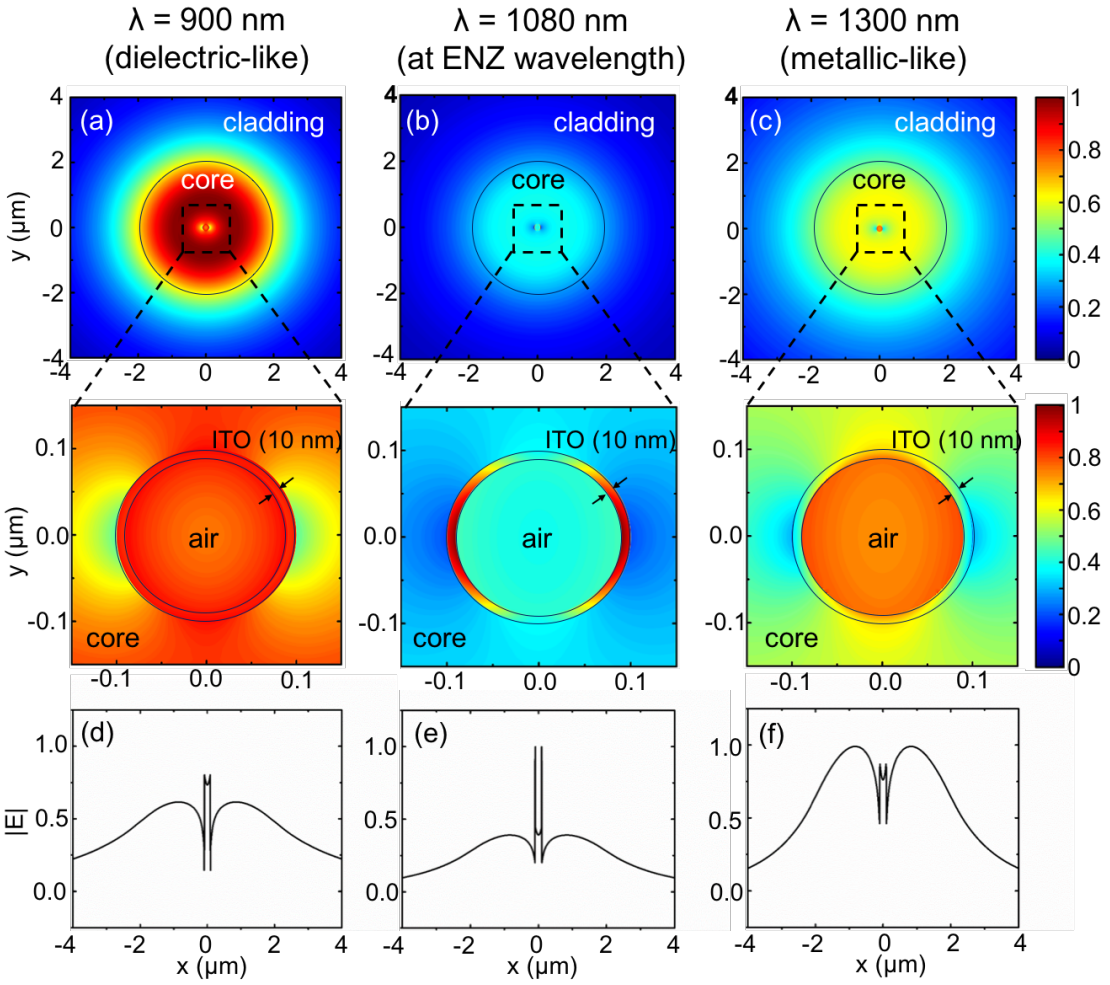

Fig. 4.3. Electric field profile of the fundamental mode supported by the ENZ fiber with 10nm ITO shell thickness at wavelengths (a, d) 900 nm (outside ENZ wavelength), (b, e) 1080 nm (at the ENZ wavelength), (c, f) 1300 nm (outside ENZ wavelength). In (a-c), the top images are the contour plots of electric field magnitude on the entire fiber cross-section and the bottom images zoom in on the ITO nanoshell. The black circles outline the structure of the fiber. (d-f) depict |E| along the diameter of the fiber.

The field enhancement in the thin ITO shell suggests that the modal properties of the fiber ENZ mode may be sensitive to the perturbations of the surrounding medium's optical properties, in particular, the dielectric permittivity of the constituents in the central hollow channel. Thus, we investigated the dependence of the modal loss spectrum on the refractive index of the central channel. The fiber ENZ modal loss spectra

calculated for five different fluids placed in the central channel of the fiber is depicted in Fig. 4.4. The refractive index of the fluid at the resonant wavelength was stated inside the parentheses next to the name of the fluid. The permittivity functions of the fluids are obtained from other reports[114-115]. The thickness of the ITO shell was kept at 20 nm. As seen in the figure, the resonant wavelength shifts from 1102 nm for air to 1156 nm for chloroform. The modal loss for chloroform is found to be 679 dB/cm, which is almost five times greater than with air at the central channel. Increasing the refractive index of the central region in the nanobore fiber effectively shifts the dispersion curve of both the guided fiber core mode and planar thin film ENZ mode (Appendix A.3.). This in turn results in the phase matching wavelength getting larger due to the change of the index of the hollow channel.

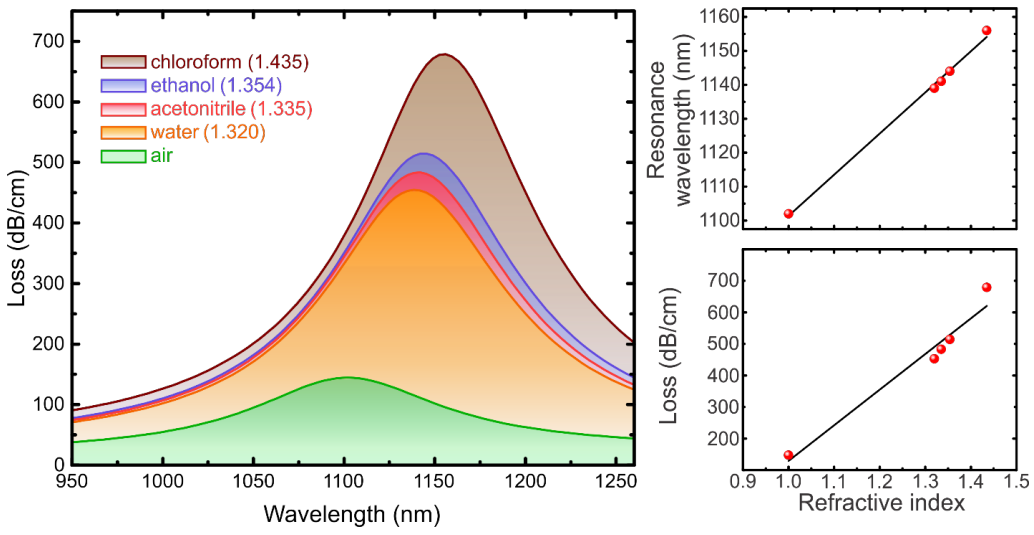

Fig. 4.4. Refractive index dependence of the ENZ fiber. The insert on the left is a sketch of the proposed index sensing mechanism where the analyte is placed inside the central channel of the fiber. The graph plots the loss spectra of ENZ mode for five analytes whose refractive indices at the resonant wavelengths are given within the parentheses. The two inserts on the right shows the refractive index dependence of ENZ resonance wavelength (slope = 121 nm/RIU) and loss on the top and bottom scatter plots respectively. The red lines in the inserts are the linear fits to the data points obtained from the main graph.

Figure 4.5 shows the comparison between the ENZ mode profiles for air and chloroform at the center of the ENZ fiber. Similar to the analysis in the planar structures, the field confinement of the ENZ mode is stronger with the external medium of chloroform, and thus the larger absorption of light was observed in the ENZ fiber with

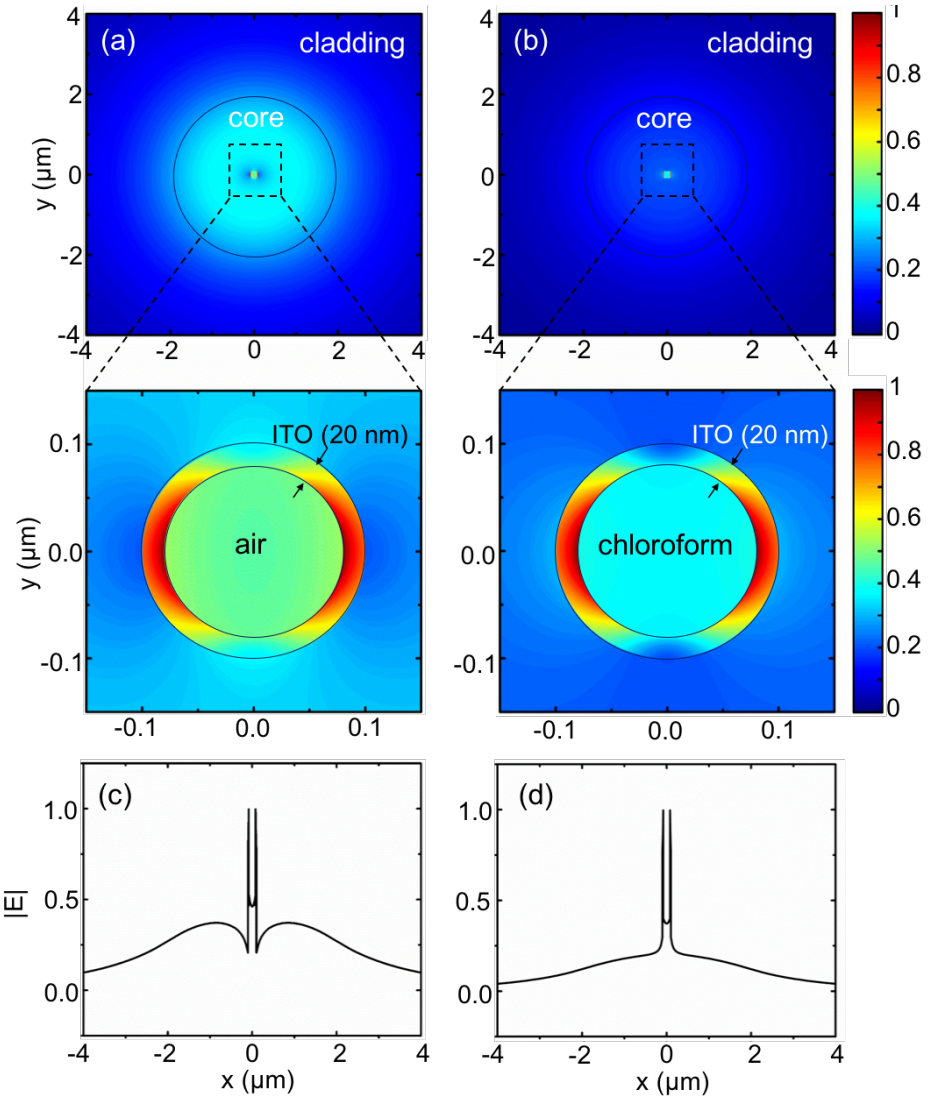

Fig. 4.5. Electric field profiles at ENZ resonance for (a,c) air, and (b,d) chloroform as analytes placed inside the ENZ fiber with 20 nm thick ITO shell. In (a) and (b), the top images are the contour plots of |E| on the entire fiber cross-section and the bottom ones zoom in on the ITO shell. The black circles outline the structure of the fiber. (c) and (d) depict |E| along the diameter of the fiber.

higher refractive index in the central nano-channel. Similar trend is observed in the field profiles for the three layer geometry (Appendix A.3).

The strong dependency on the surrounding dielectric can be exploited for novel optical/bio sensing purposes due to the unique feature of the enhanced field confinement of the ENZ mode in the fiber. For wavelength-based sensing, the average refractive index sensitivity of the ENZ fiber, defined as $\Delta\lambda/\Delta N$ where N is the refractive index of the material in the central channel of the fiber is found to be 121 nm/RIU. The observed sensitivity is comparable with other in-fiber sensing device such as Mach–Zehnder interferometer with waist-enlarged fusion bitaper [116-117] and it has better performance than some grating-based sensors [118-119]. In addition, this type of ENZ fiber sensor could be used for sensing material with wide range of refractive index, including refractive index between 1.3-1.4 in which most of the biomaterial lie on. The sensitivity of the ENZ fiber could be significantly enhanced by optimizing the materials and geometry, such as ITO thickness, core/hole diameters, choices of ENZ materials, and the core mode dispersion (e.g. engineered dispersion with additional cladding holes[105, 120]).

Conclusion

In summary, we have investigated the ENZ modes supported by a hollow fiber waveguide modified with a thin conducting oxide layer that is capable of confining high intensity fields inside a subwavelength nano-channel. At the dielectric to metal crossover point of the conducting oxide, the permittivity approaches zero enabling the excitation of ENZ mode characterized by high field enhancement in the ENZ region. The sensitivity of the waveguide's modal loss to the central channel refractive index can be exploited to

sense refractive index of medium and therefore the ENZ fiber has potential applications in optical/bio-sensing.

Methods

Numerical simulations of the waveguide structure were carried out using the MODE Solutions software from Lumerical Solutions, Inc. The effective index of the ENZ mode supported by three layer structures was calculated using of a MATLAB code developed by G. Figliozzi and F. Michelotti at the University of Rome "La Sapienza" (Italy)[121] based on the transfer matrix method [122]. In all simulations, permittivity function of silica is modeled using the Palik data [72]. Permittivity of GeO_2 doped silica (GeO_2 wt. 9% doped silica) is obtained from the literature [74]. For ITO, the Drude model is used with the parameters: the electron concentration of 1.0×10^{21} cm^{-3}, $\varepsilon_\infty = 3.6$, $\Gamma = 2.0263 \times 10^{14}$ s^{-1}, $\omega_p = 3.3722 \times 10^{15}$ s^{-1} , [123] In the index sensing analysis, the permittivity functions of the liquids that are placed inside central channel to be analyzed are obtained from literature [114-115].

CHAPTER FIVE

Enhanced Spontaneous Emission of Monolayer MoS2 on Epitaxially Grown Titanium Nitride Epsilon-Near-Zero Thin Films

This chapter published as: K. Minn, A. Anopchenko, C.-W. Chang, J. Kim, Y.-J. Lu, S. Gwo and H. W. H. Lee (SPIE, 2020) Vol. 11462

Introduction

An epsilon-near-zero (ENZ) medium, a medium with vanishing permittivity, possess different unique optical properties, including enhancement of the local density of its optical states. As a result of the enhanced density of its optical states, dipole emitters in or near the ENZ medium experience greatly enhanced spontaneous emission. In one of the earliest works on ENZ enhanced emission, a waveguide channel was used to mimic ENZ behavior at its cutoff wavelength where the propagation constant of the mode approaches zero.[38] Emitters placed inside this ENZ channel, regardless of the location, have been shown to experience an increased emission rate. Besides affecting the emission processes, ENZ materials can be used to enhance the excitation of emitters through the enhancing absorption and electric field in the emitting layer at the excitation wavelengths. Metal-insulator-metal cavities have been employed to engineer the effective permittivity of the structures.[39] Such multilayer planar cavities may exhibit multiple ENZ points which can be used to simultaneously increase absorption and the Purcell factor at the excitation and emission wavelengths, respectively. An increase in broadband excitation (absorption) has been observed in solar-harvesting modules with quantum dots deposited atop the metallic nanostructures with a complex network of ENZ regions in the

visible spectrum.[40] Absorption and photoluminescence (PL) of two-dimensional (2D) emitters can be significantly enhanced by using interference and resonance effects in 2D materials backed with planar and nanostructured metallic reflectors,[41-44] plasmonic resonances coupled to both excitation and emission fields,[124-125] hyperbolic metamaterials and photonic crystals.[45] However, most of these studies are limited to complex and anisotropic structures such as hyperbolic metamaterials that require complicated design and nanofabrication techniques. This study employs thin homogeneous titanium nitride (TiN) films with ENZ wavelengths in the visible spectrum that match a wide excitation bandwidth of quantum dots and 2D emitters to probe ENZ-emitter interaction.

The transition metal compound TiN is a promising material due to its refractory properties,[126] mechanical strength,[127] CMOS compatibility,[128] low optical losses in the visible spectrum,[129] and high optical nonlinearity.[29, 130-131] Another advantage of TiN is that its optical properties are tunable by the stoichiometry control,[132-133] and by applying electrical bias to TiN heterostructures.[134] The real part of the complex permittivity of TiN nears zero (ENZ) in the visible spectrum, i.e. its optical response changes from dielectric-like to metal-like. A few works have utilized the plasmonic properties of TiN including its ENZ properties in various applications, for example, a high-temperature stable broadband absorber for solar thermo-photovoltaics,[132] super-resolution stimulated Raman scattering microscopy with non-stoichiometric TiN,[135] and disordered nonlinear metalens for Raman spectral nanoimaging.[136] The plasmonic waveguiding properties of epitaxially-grown TiN has been demonstrated recently.[129] It has been proposed that the ENZ properties of TiN grids protect quantum information of spatially-separated quantum emitters against decoherence in on-chip quantum networks with a small footprint.[137] The

near-zero permittivity of sputtered TiN has been used to tune the emission of quantum dots.[134] However, the modulation of emission rate by the metallic TiN due to the emitter's proximity to the TiN surface has not been explored. In addition, the experimental evidence on how the transitioning in a thin film's optical permittivity from dielectric to metallic affects the fields in the adjacent thin emitting layer is urgently needed for numerous nanophotonics device applications. The simple and conclusive way to achieve this is by using 2D emitters to probe the ENZ properties of ultrathin TiN films over a broad range of excitation conditions.

To this end, we place monolayer molybdenum dioxide (MoS_2) on TiN films and collect the PL emitted in the far-field. MoS_2 is a transition metal dichalcogenide, with 1.8 eV direct bandgap in monolayer form.[138] Its electronic and optical properties have been studied extensively,[139-141] as well as room temperature quantum emission,[142] ultrathin waveguiding,[143] directional emission.[144] Two-dimensional semiconductors in general, and MoS_2 in particular, are considered as stable light emitters with small fluorescence fluctuations, in contrast to the quantum dots and dye molecules.[145] However, the monolayer has low absorption due to its angstrom scale thinness, as well as low quantum efficiencies (in the 10^{-3} order of magnitude) due to dominant Auger and other non-radiative processes,[139, 141, 146-147] prompting efforts to increase its optical performance. The spatial distribution of emitters in each monolayer flake is relatively homogeneous in the microscale (see Appendix B.1), making it an ideal material for emission enhancement studies with far-field optical setups. In addition, the excitonic emission in the monolayer

MoS_2 is almost entirely due to in-plane dipoles,[148] and the light is emitted with a peak intensity normal to the exciton dipole in the monolayer.[149]

In this work, the PL from MoS_2 flakes on thin (~50 nm) and thick (~130 nm) TiN films was measured using a confocal laser scanning fluorescence microscope with several excitation wavelengths across the ENZ wavelength. The measured PL enhancement, the ratio of integrated PL intensity with the TiN substrate to that of the sapphire substrate, was verified against the numerical calculations based on the equivalence between the probability of the radiative decay for a dipole transition and the power radiated by a classical dipole antenna, together with Fresnel-coefficient formulation of fields inside a stack of thin films. To gain insight into the role of optical losses in the PL enhancement of ENZ films, we fabricated TiN ENZ films with different properties (e.g., losses, ENZ wavelength) using molecular beam epitaxy (MBE) and magnetron sputtering methods and compared the PL enhancements. To reduce non-radiative recombination of excitons, an alumina spacer layer of a few nanometers was fabricated to separate the MoS_2 layer and TiN substrates. The results obtained with 30 nm- and 6 nm- thick alumina spacers shed light on the interference processes responsible for the radiative decay rate enhancements. This is the first comprehensive study of PL from a 2D material placed near ENZ films and its dependence on the losses of ENZ materials, spectral response with excitation across the ENZ wavelength, and oxide spacer thicknesses. Our results show that the ENZ substrate enhances absorption and the electric field of light excitation in the MoS_2 monolayer and hence enhances its spontaneous emission. This study will

enrich the fundamental understanding of spontaneous emission on ENZ substrates that might be useful for the development of advanced nanophotonic light sources.

Results and Discussion

The permittivity obtained from the ellipsometry measurements of the two TiN thick films (MBE grown and sputtered) used in the PL enhancement measurements (see Methods) along with the permittivity of gold from Johnson and Christy[150] are plotted in Fig. 5.1. See Appendix B.2 for the permittivity of all TiN samples used in the

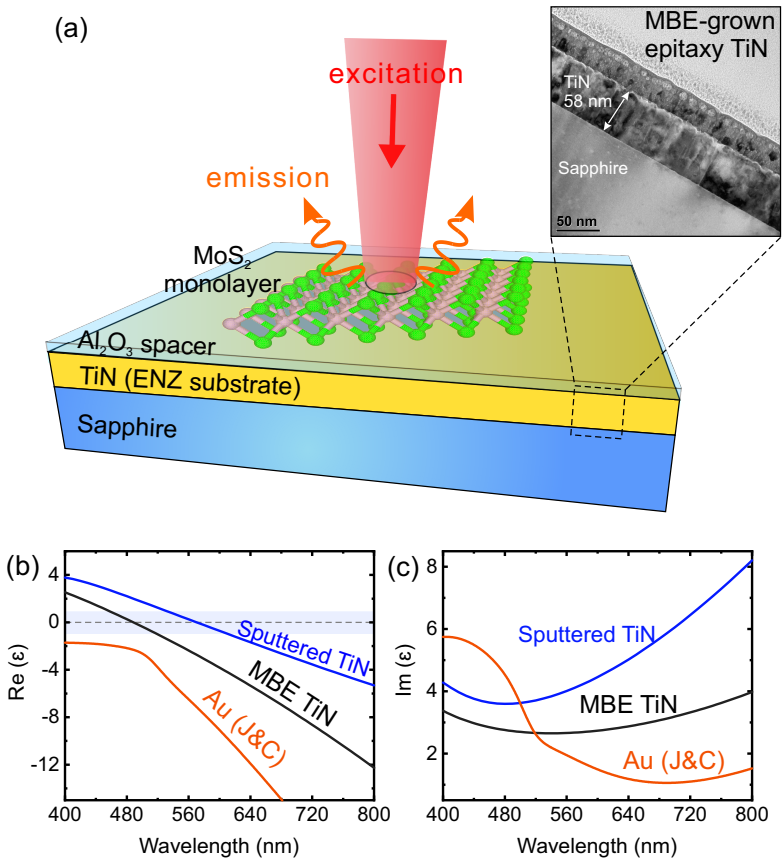

Fig. 5.1. (a) Schematic of the structures for studying spontaneous emission on TiN ENZ substrate. Inset: TEM image for one of the MBE-grown epitaxial TiN samples with thickness of 58 nm. (b) Real and (c) Imaginary part of permittivity of MBE-grown single-crystalline TiN film (thickness 133 nm) and sputtered TiN film (thickness 146 nm) measured from spectroscopic ellipsometry and gold from literature.

experiments. The thickness of MBE-grown film and sputtered film are obtained from the scanning electron microscopy images of the film cross-sections. The most significant feature is that, unlike noble metals such as gold, TiN transitions from dielectric to metallic in the visible spectrum with the crossing wavelength (ENZ wavelength) at 490 nm for MBE-grown film and 570 nm for sputtered film. In addition, the metallic TiN films have similar optical loss as gold in the visible regime (Fig. 5.1b, c). Another feature is that the MBE-grown TiN permittivity has both larger real part $|\varepsilon'|$ and smaller imaginary part ε'', implying better plasmonic performance, than the sputtered sample. TiN is a good alternative material to noble metal for plasmonic enhancement of spontaneous emission due to its ENZ characteristic in the visible spectrum. Indeed, an enhanced absorption is expected in a 2D emitter placed on ENZ substrate. Consider a very thin emitting layer (e.g., 2D emitter) with a complex permittivity ε_{em} and a thickness t much thinner than the wavelength λ, i.e., $2\pi t \ll \lambda$, placed on a substrate with a complex refractive index $n_{sub} + ik_{sub}$. The absorptance of the ultrathin layer is calculated as 1 - R - T, where R and T are the reflection and transmission coefficients.[151] Absorptance for a plane wave incident on the layer from air at normal incidence is given by the following expression:

$$A = \frac{8\pi t}{\lambda} \frac{\varepsilon''_{em}}{(1+n_{sub})^2+k_{sub}^2} + O\left(\left(\frac{2\pi t}{\lambda}\right)^2\right).$$

The above equation is derived by taking a power series expansion for the absorptance up to the first order in thickness and neglecting higher-order terms with the O ( ) symbolizing the second order term. This equation shows that light absorption and thus optical excitation of the 2D emitter is enhanced if the emitter is placed on an ENZ

substrate with low losses, i.e. $k_{ENZ} = n_{ENZ} = \sqrt{\varepsilon''_{ENZ}/2} \approx 0$. Similarly, near-perfect absorption throughout the visible and into the near-infrared spectrum has been shown in ultra-thin metals deposited on an index near zero (INZ) substrate.[152] The thin films of ENZ materials can support modes with highly confined fields which can couple strongly to emitters and metamaterial resonators.[153]

The assembly of emitter and substrate layers used in the experiment is sketched in Fig. 5.2a. It consists of a sapphire substrate (C-plane), epitaxial or sputtered TiN films, an atomic layer deposited Al_2O_3 spacer layer, and MoS_2 monolayer flakes (see Methods for details on sample fabrications). The Al_2O_3 spacer is not included in the reference sample that consists of MoS_2 flakes on a sapphire substrate since they have very similar optical properties. The PL images are taken with a dry 0.9 NA objective at normal incidence.

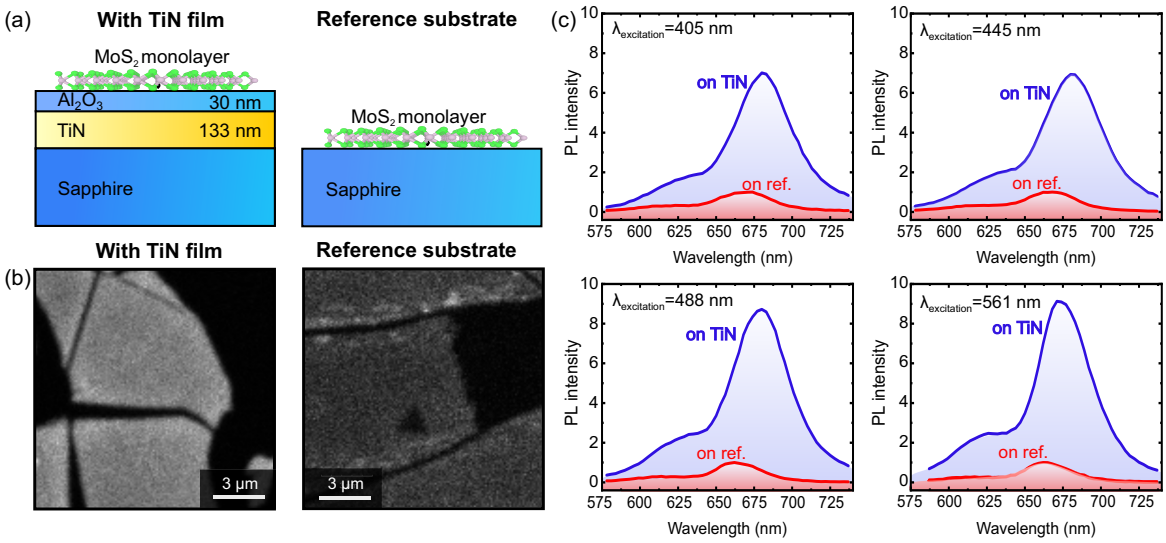

Fig. 5.2. Spectral and spatial resolved photoluminescence (PL) measurements. (a) Schematics of the samples on TiN substrate and reference substrate. (b) Typical spatially-resolved photoluminescence maps of MoS_2 on titanium nitride substrate and sapphire substrate. Two maps have the same greyscale. (c) Measured PL spectra of MoS_2 on TiN substrate (thickness of 133 nm and ENZ wavelength of 490 nm) (blue curves) and reference substrate (red curves) using four different excitation lasers with varied wavelengths.

Experimental details can be found in Methods section. Typical PL maps integrated from 640 to 700 nm emission wavelength obtained by 561 nm excitation of the flakes on epitaxial TiN (thickness of 133 nm) and on the reference sapphire are shown in Fig. 5.2b. The two maps have the same greyscale for direct comparison, and emission of the MoS_2 on TiN is clearly much brighter than on the sapphire. In addition, the PL enhancement on the titanium nitride with respect to the sapphire depends on the excitation laser wavelength, as shown in the emission spectra plotted in Fig. 5.2c for four excitation wavelengths across the ENZ wavelength. Room temperature PL spectra of MoS_2 flakes on both substrates have neutral A and B exciton peaks and charged exciton A^- trion peaks, which shapes are described by Lorentzian functions (see Appendix B.3).[154]

To gain insight into the dependence of the PL enhancement on excitation laser wavelength and Al_2O_3 spacer thickness, we performed numerical calculations of fluorescence enhancement for an emitter embedded inside a multilayer geometry.[155-156] The total electromagnetic enhancement of the PL is the product of two contributions: excitation enhancement and emission enhancement.[156-157] The excitation field enhancement due to the 133 nm thick MBE-grown TiN substrate leads to enhanced absorption of MoS_2 normalized with respect to the reference sample, which varies with spacer thickness and excitation wavelength (Fig. 5.3a). In this configuration, the TiN film acts as a metallic reflector (negative permittivity in most of the wavelength range), and the field intensity and consequently the absorptance is enhanced due to interference of the incident and reflected beams inside the open cavity. For spacer thicknesses comparable to the quarter of the incident wavelength or larger, the multi-beam interference dominates

and the Fabry-Perot resonances are responsible for the large enhancements (e.g., maximum PL enhancement with spacer thickness ~80 nm and ~280 nm).

The emission enhancement due to the TiN substrate at the emission wavelength is the enhancement in the radiative quantum efficiency, also called the external quantum efficiency (EQE), that is defined as a fraction of the radiative decay rate modified by the Purcell factor to the total decay rate, which depends on the intrinsic quantum efficiency.[155-157] The Purcell factor of an in-plane dipole located in the middle of MoS_2 layer above 133 nm thick TiN, which includes decay rate into far-field, surface modes, and absorption in the metal, is calculated as a function of emission wavelength and spacer thickness (Fig. 5.3b). The Purcell factor is greatly enhanced for small Al_2O_3 spacer thicknesses due to the high local density of optical states near the metallic TiN surface at the MoS_2 excitonic emission wavelengths, which will be discussed in Fig. 5.5. For spacers thicker than 10 nm, the Purcell factor is unity for all wavelengths and thus not shown in the figure. EQE has similar spacer dependence to the absorption enhancement for spacers larger than ~10 nm (Fig. 5.3c). In this spacer thickness range (> 10 nm), Purcell enhancement is negligible, and the emission enhancement is mainly due to the interference effects. Total PL enhancement integrated over the emission wavelength range from 575 to 740 nm is plotted in Fig. 5.3d. The maximum enhancements are challenging to attain experimentally in the normal incidence-collection configuration because the excitation wavelength for maximum enhancement overlaps with the emission wavelength range, making it difficult to filter out the excitation laser in the collection path. The experimentally attainable enhancements inside the dashed box show the wide-angle interference around ~30 to ~50 nm spacer range and multi-beam interferences or Fabry-

Perot resonances for the large spacers[156]. The case of a thin spacer (< 10 nm) is unique in the sense that the radiative decay rate is not modulated by cavity resonances but by the material dispersion and will be discussed thoroughly in Fig. 5.5.

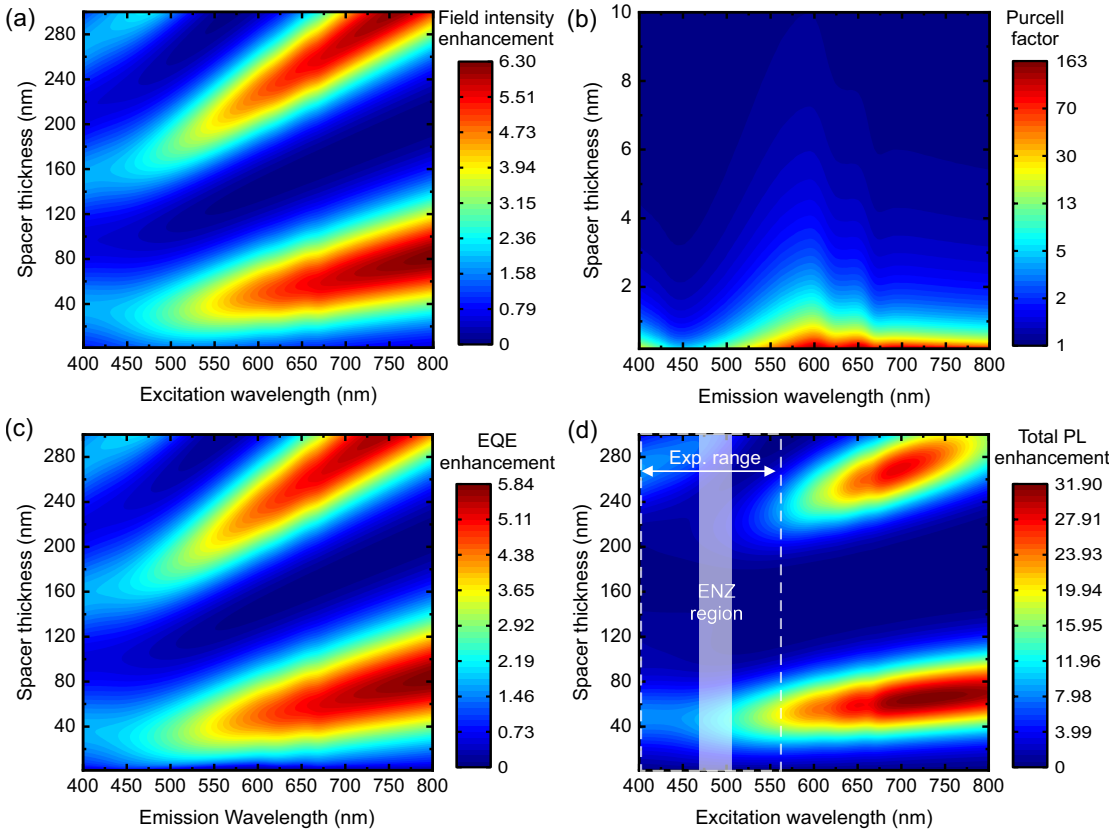

Fig. 5.3 (a) Enhancement of absorption in the MoS_2 monolayer on MBE-grown titanium nitride (thickness of 133 nm) with respect to that on sapphire substrate, (b) the Purcell factor (only shown up to 10 nm spacer, above which Purcell is 1 for all wavelengths), (c) EQE enhancement, and (d) total electromagnetic enhancement of the in-plane dipole in MoS_2 monolayer on TiN as a function of spacer thickness with respect to that on sapphire substrate.

In the experiments, we first investigated the wide-angle interference effect of TiN films by using the Al_2O_3 spacer thickness of 30 nm. We report the PL enhancement from MoS_2-spacer-TiN stacks as a function of excitation wavelength for MBE-grown epitaxial TiN and sputtered TiN. Four samples with different thicknesses: 58 nm and 133 nm thick

MBE TiN films, and 51 nm and 146 nm thick sputtered TiN films are used in the experiments to verify the consistency of the results while shedding light on the effect of material losses (ε'') versus the film thickness. As a comparison, the result from MoS_2-spacer-Au stack (Au film thickness 100 nm) is also included. The experimental and calculated PL enhancements as a function of excitation wavelength, plotted in Fig. 5.4, show good agreement with each other. For the MBE-grown epitaxial TiN (black curves in Fig. 5.4a, b), as the transition from lossy dielectric to metallic across the ENZ wavelength occurs, the PL enhancement becomes stronger (showing ~ 2-fold enhancement). In contrast, the sputtered TiN samples (blue curves in Fig. 5.4a, b), having ENZ at slightly longer wavelength than the excitation wavelength range, are all dielectric and thus do not exhibit the same trend as the MBE samples. In addition, since the MBE-grown TiN films have lower optical losses across the visible and IR spectrum and shorter ENZ wavelengths than the sputtered films (see Fig. 5.1c and Appendix B.2), the enhanced PL emission is 2 to 3 times higher. Among the two MBE TiN films, the PL enhancement for 133 nm thick sample is larger than for the 58 nm sample due to higher reflectivity even though 58 nm sample has smaller loss (Appendix B.2). It can be observed that epitaxial TiN and Au have comparable performance (black curve in Fig. 5.4b vs green curve in Fig. 5.4c), especially above the ENZ wavelength of TiN where its negative real permittivity gets larger and more metallic. In the dielectric domain, TiN has a relatively smaller enhancement than Au despite having smaller loss (Figure 5.1c). This is expected in this regime because the emitter is far enough from the lossy medium that the contributions by the surface modes and metal absorption is insignificant. Being all

metallic, Au's peak near 560 nm is due to minimum in its imaginary permittivity which leads to smaller losses.

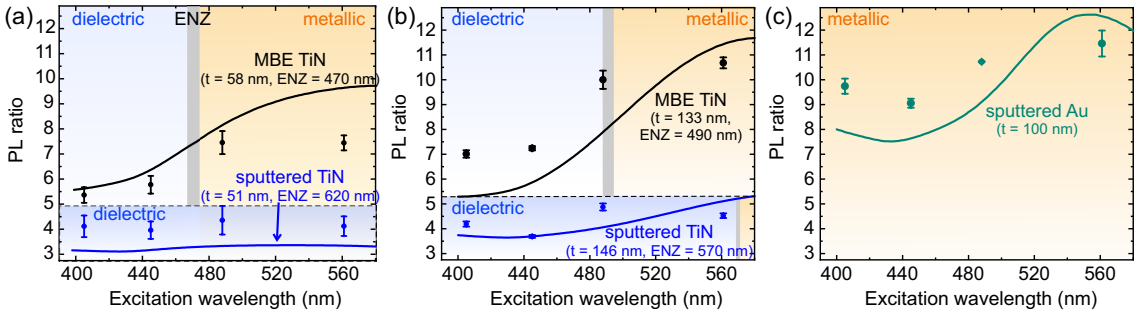

Fig. 5.4. Measured and calculated PL enhancements of MoS_2 on TiN and Au films with 30-nm-thick Al_2O_3 spacer layer with respect to that on sapphire substrate. Samples are (a) 58-nm-thick MBE-grown TiN (black) and 51-nm-thick sputtered TiN (blue), (b) 133 nm thick epitaxial TiN (black), and 146 nm thick sputtered TiN (blue), and (c) 100 nm thick sputtered Au. Data points with error bars are measured and solid curves are calculated. Gray vertical lines indicate the ENZ wavelengths TiN films.

For thin spacers (<10nm), far away from the Fabry-Perot and wide-angle interference resonances, maximum field and absorption enhancements are determined by the material property of TiN as shown in Fig. 5.5a. PL enhancement is optimal at the excitation wavelengths near ENZ wavelengths where absorption in MoS_2 is optimal. Despite the exponentially growing Purcell factor (Fig. 5.5b), the EQE enhancement decreases as the spacer thickness is decreased (Fig. 5.5c). Hence it can be deduced that the decay rate into surface modes and metal absorption dominates. The peak in the Purcell factor for ultrathin (< 5 nm) films is at the surface plasmon resonance, red-shifted from the ENZ wavelength as indicated by the band-structure calculation (Appendix B.4). In contrast to the wide-angle interference and Fabry-Perot resonances, the maximum PL enhancement (Fig. 5.5d) is within experimentally attainable range inside the dashed box. The measured PL enhancements of MoS_2-spacer-TiN stacks as a function of excitation wavelength for 6 nm spacers are depicted in Fig. 5.5e for 58 nm thick MBE-grown

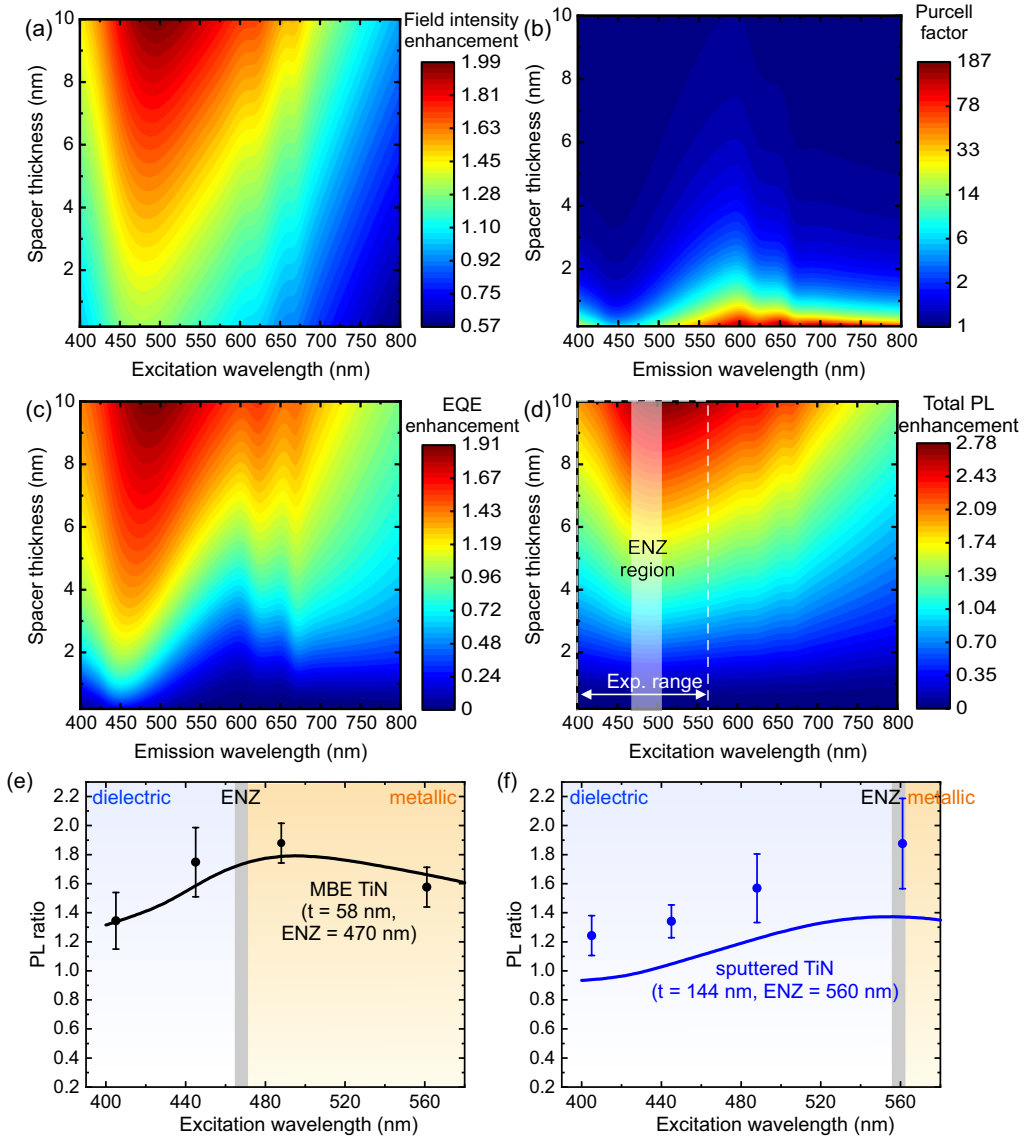

Fig. 5.5. (a) Enhancement of absorption in the MoS_2 monolayer on MBE-grown TiN (thickness of 58 nm) with respect to that on sapphire substrate, (b) the Purcell factor, (c) EQE enhancement, and (d) total electromagnetic enhancement of the in-plane dipole in MoS_2 monolayer on TiN as a function of spacer thickness. Measured and calculated PL enhancements MoS_2 on 58 nm thick MBE-grown, and (f) 144 nm thick sputtered TiN substrates with Al_2O_3 spacer thickness of 6 nm with respect to that on the sapphire substrate. Data points with error bars are measured and solid curves are calculated. Gray vertical lines indicate the ENZ wavelengths TiN films.

sample and in Fig. 5.5f for 144 nm thick sputtered sample. PL enhancement peaks are near the ENZ wavelengths for both samples in contrast to the trend observed in Fig. 5.4 with 30 nm spacer where the interference effects dominate. The slight discrepancy

between the measured and calculated enhancements can be attributed to the uncertainty in the thickness of the thin spacer layer and the variation in the intrinsic quantum efficiency (IQE) of the MoS_2 monolayer (IQE of 0.004 is used in the calculation[158]) whose effect is pronounced in proximity to the absorbing medium. However, the dependence on the excitation wavelength observed in the experiments is replicated well by the calculations.

Lastly, we comment on the dependence of PL enhancement on the permittivity of the TiN films to gain insight into how the ENZ affect the PL for. We numerically studied the excitation and emission contributions separately for varying carrier concentration of TiN films. Since permittivity is, through the Drude term, related to carrier concentration, which in practice may be tuned either by applied biased voltage or during the deposition, varying this quantity is equivalent to varying the complex permittivity of TiN in a practical way. We found that the maximum excitation enhancement is slightly displaced from the ENZ wavelengths of TiN for varying carrier concentrations because of the losses in material. The effect of ENZ is more pronounced in the emission enhancement, with the maximum EQE enhancement occurring at the ENZ wavelengths for all carrier concentrations (details of the calculations and the results are reported in the Appendix B.5).

Conclusion

In summary, we present a comprehensive study of photoluminescence from a 2D material placed near ENZ films and show the PL's dependence on the losses of ENZ materials, the excitation wavelength across the ENZ wavelength, and the oxide spacer thicknesses. We investigated the enhancement of PL emission from MoS_2 monolayer flakes due to TiN substrates, both MBE-grown and sputtered, at multiple excitation

wavelengths covering diverse complex permittivity values of TiN. We observed larger PL enhancement by the MBE-grown TiN films than their sputtered counterparts due to the low loss metal-like optical response of the epitaxial crystalline films. In addition, we demonstrated that the PL enhancement effectively doubles during the transition from dielectric to metallic regime across the ENZ wavelength. By making use of two spacer thicknesses, each of them enforcing a distinct optical phenomenon, we showed the contributions of the interference effect and the ENZ effect toward radiative decay rate enhancement. The effect of ENZ on the PL enhancement is further illuminated by analyzing the correlation between the permittivity and excitation enhancement as well as the correlation between the permittivity and emission enhancement. We note that for ultra-thin spacers, since the emission is coupled strongly to surface modes and absorption in the medium, an out-coupling mechanism is needed to improve the quantum efficiency that can be collected in the far-field. Utilization of periodic structures such as gratings, photonic cavities, and hyperbolic structures to enhance radiative emission has been reported exhaustively,[159-163] and similar mechanisms may be employed here. The emission enhancement of TiN films may have applications in optical, optoelectrical, display, and energy harvesting technologies.

Methods

Sample Fabrication

The growth of single-crystal TiN (111) thin films on a 2-inch c-sapphire substrate was carried out using a plasma-assisted molecular beam epitaxy (PAMBE) system (DCA Instruments Oy, Turku, Finland) equipped with a nitrogen plasma source (Veeco, UNI-Bulb). The base pressure of ultra-high vacuum MBE was kept about 1×10^{-10} torr before

growth. The highly pure 6N nitrogen source flux was controlled via a high-resolution mass flow controller and purified by a nitrogen purifier. Elemental titanium (Ti) of purity 5N was provided by a solid source effusion cell (DCA Instruments Oy). The double-side polished sapphire substrates were cleaned with acetone, isopropanol, and deionized water in an ultrasonic bath to remove residual organic contamination and then desiccated by nitrogen gas. Before growing the TiN epilayer, the substrate was thermally cleaned at 900 °C to obtain a clean substrate surface. The structural analysis of the single-crystal TiN is reported in the Appendix B.6. The sputtered films were deposited on the sapphire substrates by DC magnetron sputtering of the Ti target at a chamber pressure of $7.5 \times 10{-}7$ torr and at room temperature. Details on the fabrication of the epitaxial and sputtered TiN samples can be found in previous reports.[129, 134] The spacer Al_2O_3 films were deposited on TiN-sapphire substrates by atomic layer deposition at base pressure 10^{-3} Torr and at temperature 150 °C. Trimethylaluminum precursor was used, and the pulse duration was 21 ms. Commercial CVD-grown MoS_2 monolayer flakes (2dlayer, SF-MOS2-SI) were transferred using a dry stamping method.[164] Silicone gel films were stamped onto flakes grown on a Si substrate to pick up the flakes, and subsequently stamped onto the target Al_2O_3-TiN-sapphire substrates and reference sapphire substrates. A wide-field optical microscope was used to monitor the transfer process.

Optical Measurements

The permittivity of the TiN films was obtained with spectroscopic ellipsometry measurements. The photoluminescence measurements were performed on a confocal laser scanning microscope (Olympus FV 3000) equipped with a 100x objective (N.A 0.9 in air, Olympus) and four solid-state excitation lasers: 405, 445, 488, and 561 nm

(Coherent OBIS-LX series). A volume phase holographic transmission diffraction grating with motorized adjustable slit and multi-alkaline photomultiplier was used to collect the PL spectra at each pixel to obtain the hyperspectral map with a spatial dimension of 14 x 14 μm. The PL enhancement at each excitation wavelength was calculated as the ratio of the integrated PL from the TiN sample and reference sample. The error bars were obtained from about 5 - 8 sets of measurements carried out over multiple days.

Numerical calculations

Lumerical's Stack Solver and Radiating Slabs[155]– a tool to simulate, characterize, and optimize emitting, stratified optical systems – were used to calculate the PL enhancement of the in-plane dipole inside the multilayer structure. The total PL enhancement is calculated as the product of excitation enhancement and emission enhancement:

$$PL\ ratio = \frac{E_{TiN}^2}{E_{Sapph}^2} \times \frac{\left({}^{P_{rad}}/_{P_{total}}\right)_{TiN}}{\left({}^{P_{rad}}/_{P_{total}}\right)_{sapph}}$$

where $\frac{E_{TiN}^2}{E_{Sapph}^2}$ is the excitation enhancement, the ratio of the electric field intensity for the normal incidence at the center of a 0.65 nm thick MoS_2 layer on MoS_2-Al_2O_3-TiN-sapphire multilayer structure compared to the same quantity on the reference MoS_2-sapphire structure. P_{total} is the Purcell factor, the total dipole power including radiation into far-field and surface modes as well as metal absorption. ${}^{P_{rad}}/_{P_{total}}$ is the external quantum efficiency (EQE), the fraction of total dipole power that is radiated into the far-field cone angle set by the numerical aperture of the collecting objective. The emission enhancement is the ratio of EQE's for an in-plane dipole located at the center of the MoS_2 layer for each of the two structures.

CHAPTER SIX

Conclusion

The interfacing of optical fibers with metallic tips based on the nanofocusing property of surface plasmon polaritons (SPP) provides a tool for background free nanoscale optical imaging. On the other hand, the integration of transparent conducting oxide films with optical fibers and nanoscale light emitting layers based on the strong field confinement property of epsilon-near-zero (ENZ) resonance opens new possibilities in nanophotonic device applications. In this dissertation, I have presented the realization of devices that utilize these properties of SPP and ENZ resonances: a novel optical fiber plasmonic probe, an optical fiber ENZ waveguide and an ENZ-enhanced light emitting device. The results of these works are summarized as follows.

In chapter two, a photonic-plasmonic probe that transforms linearly polarized excitation beam to radial plasmons on the plasmonic tip is presented. It is shown that asymmetric excitation of SPP through an aperture leads to spiral propagation along the tip to converge towards the hotspot at the nanoscale apex. The focusing efficiency is comparable to the performances of other fiber tips excited using radial mode. Various ways to optimize the focusing and collection performance of the device is also suggested.

In chapter three, the experimental realization of photonic crystal fiber-aperture-nanoantenna probes for nanofocusing of light is presented. It is shown that the longitudinal light scattering from the tip apex is enhanced with the input linear polarization aligned for optimal coupling between the aperture and tip. The probe is a

promising platform for the development of novel devices and applications such as remote sensing and nearfield spectroscope, single photon excitation and quantum sensors, nanoscale optical lithography, and lab-on-fiber devices.

In chapter four, the excitation of ENZ mode inside a thin conducting oxide shell embedded inside a hollow core optical fiber is presented. It is shown that the phase matching between the fiber mode and the thin film ENZ mode occurs at the dielectric to metal crossover point of the conducting oxide. At this resonance, the hybridized guided mode of the fiber is characterized by high field enhancement in the ENZ layer. The sensitivity of the waveguide transmission to external refractive index variation is also explored. In addition, due to the excitation of the highly confined ENZ mode in the optical fiber waveguide, the ENZ fiber could be potentially useful in studying nonlinear and magneto-optics as well as enhanced quantum emission near ENZ medium and transmitting optical energy below the diffraction limits in fiber.

In chapter five, a comprehensive investigation of of photoluminescence (PL) enhancement from monolayer MoS_2 on titanium nitride (TiN) films near the ENZ resonance is presented. The results shed light on the PL's dependence on the losses in the ENZ films, the wavelength of the excitation laser, and the spacer thickness between the emitter and ENZ layer. It is observed that the MBE-grown TiN films achieve larger PL enhancement than sputtered ones because of lower losses in the epitaxial crystalline films. The PL enhancement is found to double as TiN films transition from dielectric to metallic regime via the ENZ point. The effects of interference and the ENZ resonances are also distinguished by the choice of thick and thin spacers. The need to improve the radiative quantum efficiency for ultra-thin spacers using gratings and other outcoupling

mechanism is also suggested. The emission enhancement of TiN may find widespread applications. In particular, the ultrathin epitaxial crystalline TiN films can switch from a poorly reflecting dielectric to good metallic reflector with applied voltage at a fixed wavelength in the visible range due to the electrically tunable permittivity of thin TiN films. This property may be of great importance to various optical, optoelectrical, display, and energy harvesting technologies.

APPENDICES

APPENDIX A

Supporting Information for Excitation of Epsilon-Near-Zero Resonance in Ultrathin Indium Tin Oxide Shell Embedded Nanostructured Optical Fiber

A.1. ENZ Wavelength of ITO

The complex refractive index of ITO ($\boldsymbol{n} = \sqrt{\boldsymbol{\varepsilon}}$) is calculated from the Drude model permittivity function:

$$\boldsymbol{\varepsilon(\omega)} = \boldsymbol{\varepsilon}_{\infty} - \frac{\boldsymbol{\omega_p}^2}{\boldsymbol{\omega^2 + i\omega\Gamma}}$$

with the large frequency limit $\varepsilon_{\infty} = 3.6$, plasma frequency $\omega_p = 3.3722 \times 10^{15}\ s^{-1}$, and damping coefficient $\Gamma = 2.0263 \times 10^{14} s^{-1}$. Since $Re(\varepsilon) = Re(n)^2 - Im(n)^2$, the vanishing real part of permittivity can be seen in figure A.1 as the intersection of real and imaginary parts of refractive index curves. To the left of this ENZ wavelength, large $Re(n)$ and small $Im(n)$ implies that the optical property of ITO is dielectric-like, while to the right at large wavelengths, larger imaginary than the real part of index, or equivalently, the negative real part of permittivity, implies metal-like behavior.

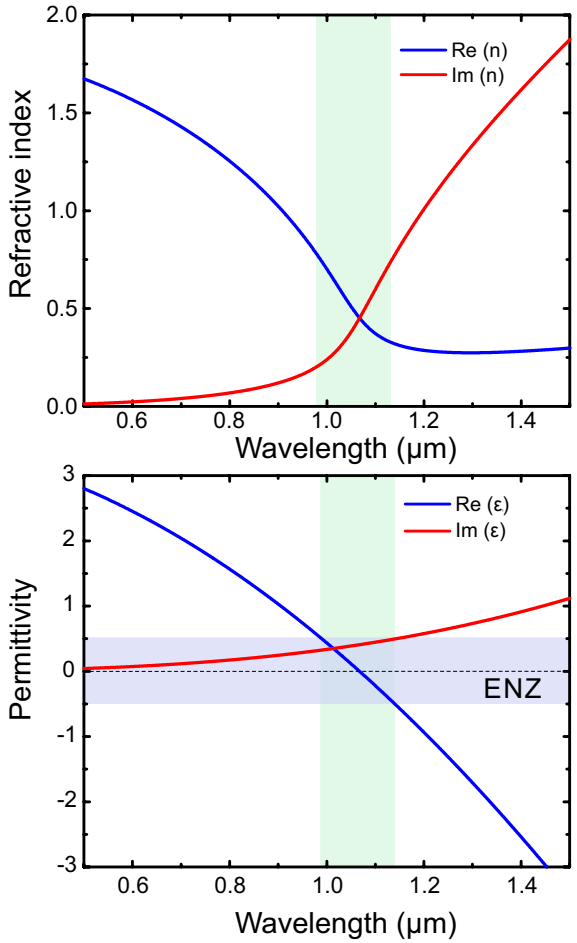

Fig. A. 1. Complex refractive index and permittivity of ITO as a function of free space wavelength. At the crossover of real and imaginary parts of the index, the real part of permittivity vanishes

A.2. Higher Order Modes of ENZ Fiber

At low wavelengths, the ENZ nanobore fiber can support four modes: HE11, HE21, TM01, TE01. However, only the fundamental HE11 mode (linearly polarized) is supported by the fiber at large wavelengths since the three higher order modes cut off below 900nm. We use finite difference method to solve Maxwell's equations on a cross-section of the ENZ fiber with the 10 nm thick ITO shell at the wavelength of 600 nm. Each of the three higher order modes is tracked over a wavelength range to calculate the modal loss, defined as $loss = -20log_{10}e^{-2\pi k/\lambda_0}$, where k is the imaginary part of the effective index. Near the cut off wavelength of each mode, the optical field gets more and more spread out into the cladding. As a result, the loss vanishes as the cut off wavelength is approached. Figure A.2 shows the modal losses of those modes as a function of wavelength.

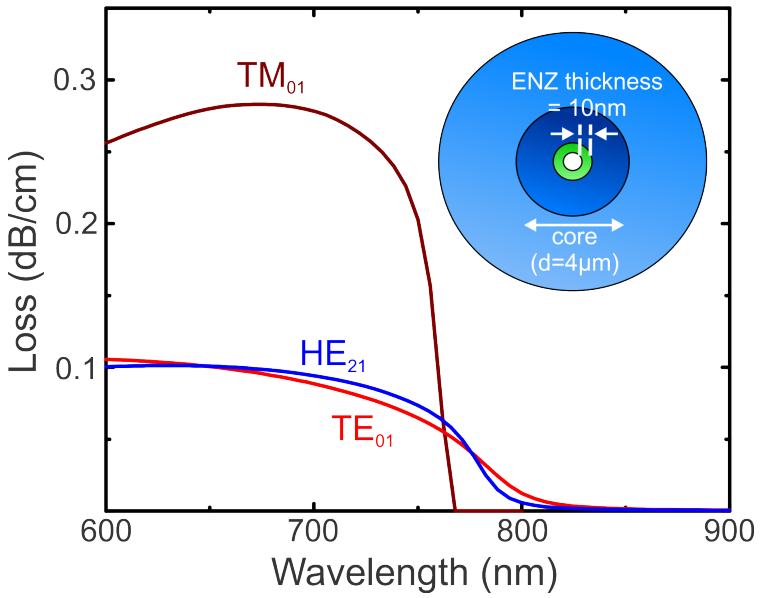

Fig. A. 2. Modal losses of ENZ fiber higher order modes. Loss vanishes as the mode approaches cutoff wavelength. The graph shows they cut off well below ENZ regime of ITO and thus, only the fundamental mode exhibits ENZ mode confinement.

A.3. Thin Film ENZ Mode in Planar Three Layer Geometry

We investigate the three layer geometry shown in the insert of figure A.3(d) using transfer matrix method. The thin film ENZ mode is excited from the glass—the core material in the ENZ fiber—half space using Kretschmann configuration. The thickness of the ITO layer is 20 nm. The reflectance is calculated for varying incident angles and wavelengths for three exiting media: ethanol, acetonitrile and air. Light incident from glass onto ITO layer is perfectly absorbed at angles larger than the critical angle and at resonant wavelengths which corresponds to the ENZ mode. Contour plots of the reflectance as a function of incident angle and excitation wavelength is presented in figure A.3(a), (b) and (c) for ethanol, air and acetonitrile as exiting media respectively. The dashed white lines show the so-called light lines or the critical angle dispersion. The dotted white lines show the locus of the minimum reflectivity at a fixed incident angle or the ENZ mode dispersion. Electric field profile across the ITO layer and the exiting medium at the phase matching wavelength and angle is also calculated using transfer matrix simulations and plotted in figure A.3(d) for the three exiting media mentioned above. The field enhancement in the ITO layer is dependent on the exiting medium refractive index in agreement with the results reported in the main manuscript.

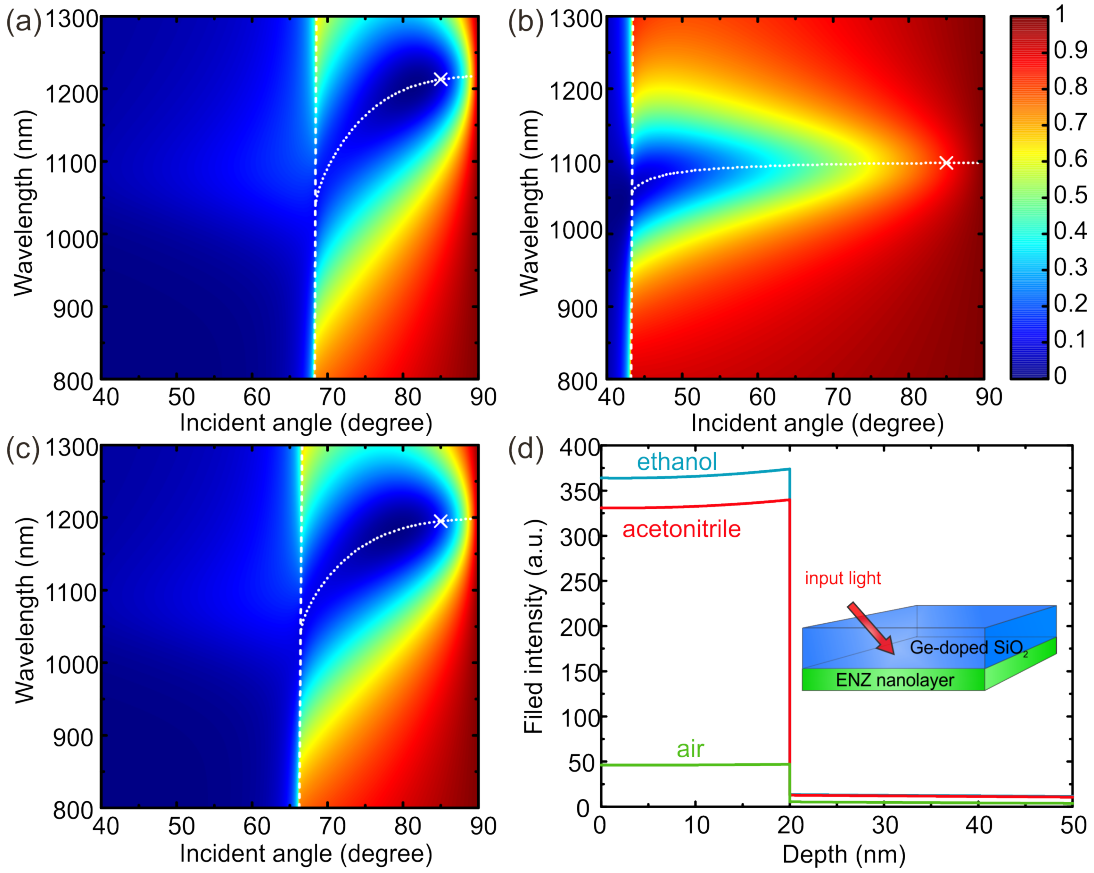

Fig. A. 3. Thin-film ENZ modes in three layer structure. Contour plot of reflectance as a function of wavelength and incident angle for (a) glass-ITO-ethanol, (b) glass-ITO-air, and (c) glass-ITO-acetonitrile structures. ITO layer thickness is 20 nm; the white dashed lines are the light lines/critical angles; the white dotted lines are the ENZ dispersion curves; and the white crosses are the phase-matching angles/wavelengths. (d) |E| inside the ITO layer for structures in (a), (b) and (c) calculated at the phase-matching wavelengths. Zero depth corresponds to the glass-ITO interface.

APPENDIX B

Supporting Information for Excitation of Enhanced Spontaneous Emission of Monolayer MoS2 on Epitaxially Grown Titanium Nitride Epsilon-Near-Zero Thin Films

B.1. PL Spectra from Different Spots on Monolayer MoS_2 Flake

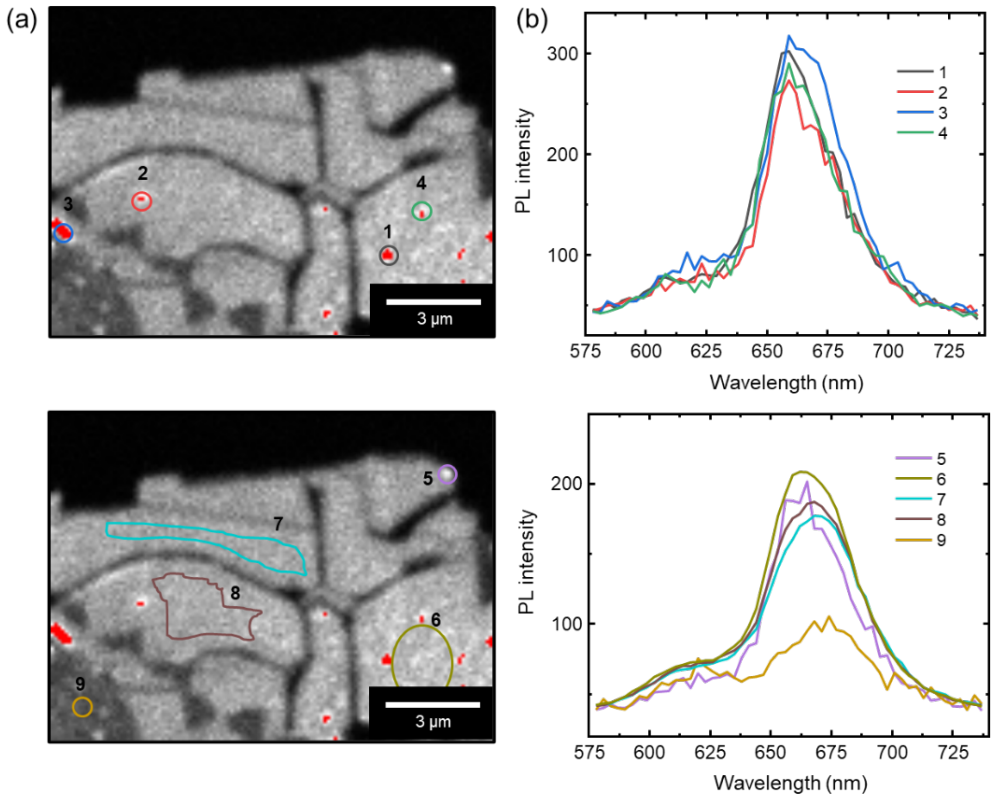

Fig. B. 1. (a) PL images of MoS_2 on TiN with 30 nm spacer taken with 488 nm excitation laser. The PL spectra from the labeled area are plotted in (b). The extremely bright spots, which are due to folds in the flake, plotted on the top panel and the extremely dim area such as the one labeled 9 are not included in the PL ratio calculations. Only the areas with homogeneous emitters such as those labeled 7 and 8 are considered.

B.2. The Permittivity of TiN Films Used in the Experiments

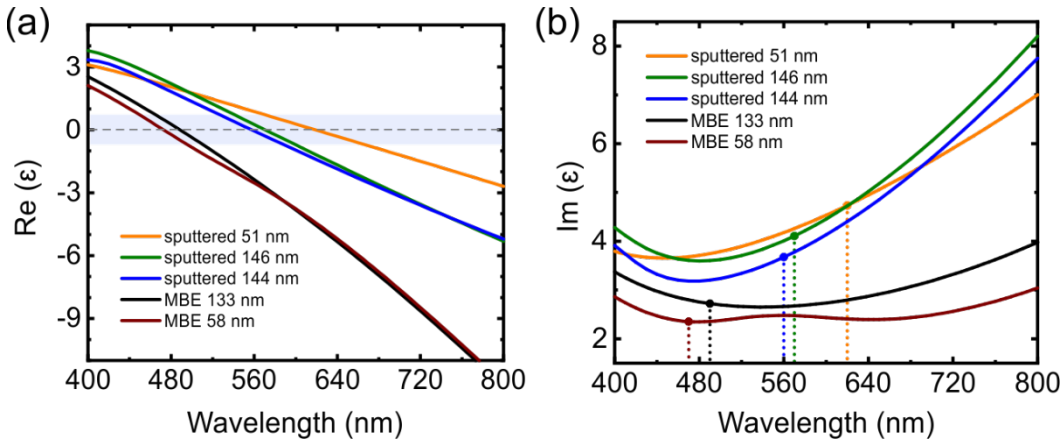

Fig. B. 2. (a) The real part and (b) imaginary part of all TiN films that are used in the experiments discussed in the main text. The thickness of the MBE samples are obtained from TEM images and that of magnetron sputtered samples are obtained from fitting the ellipsometry data. The horizontal dashed line on the left figure represents the ENZ line whereas the vertical dashed lines in the right figure denotes the ENZ wavelengths of the respective samples.

B.3. The Decomposition of MoS_2 PL into Exciton and Trion peaks

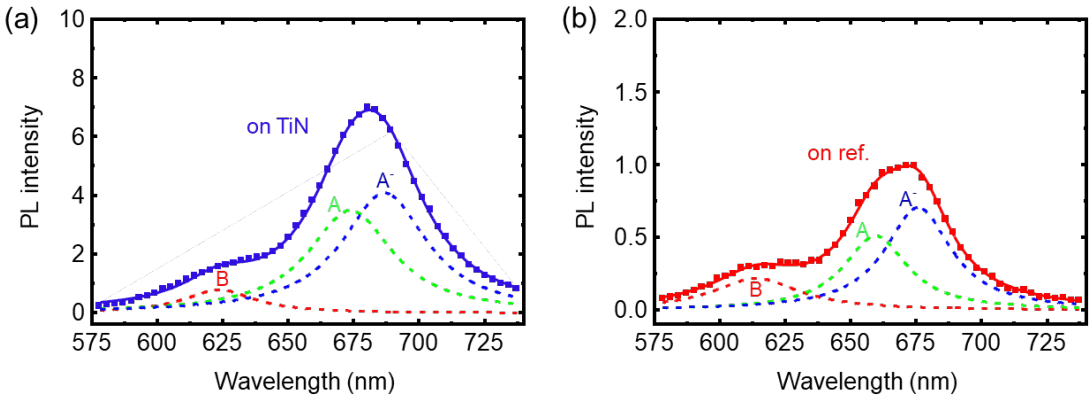

Fig. B. 3. The PL spectra of MoS_2 on (a) 30nmAl_2O_3 on 133nm TiN, and (b) reference sapphire substrate. The dots are the measured PL data, the solid curve is the fitted curve to the data using three Lorentzian peaks (dashed curves) corresponding to B-exciton (red dashed), A-exciton (green dashed), and A-trion (blue dashed). The PL ratio or enhancement is calculated by taking the ratio of the integrated areas under the total fitted curve.

B.4. Dispersion Relation of MoS_2-Al_2O_3-TiN-sapphire Structure and Dependence of Purcell Factor on TiN Thickness

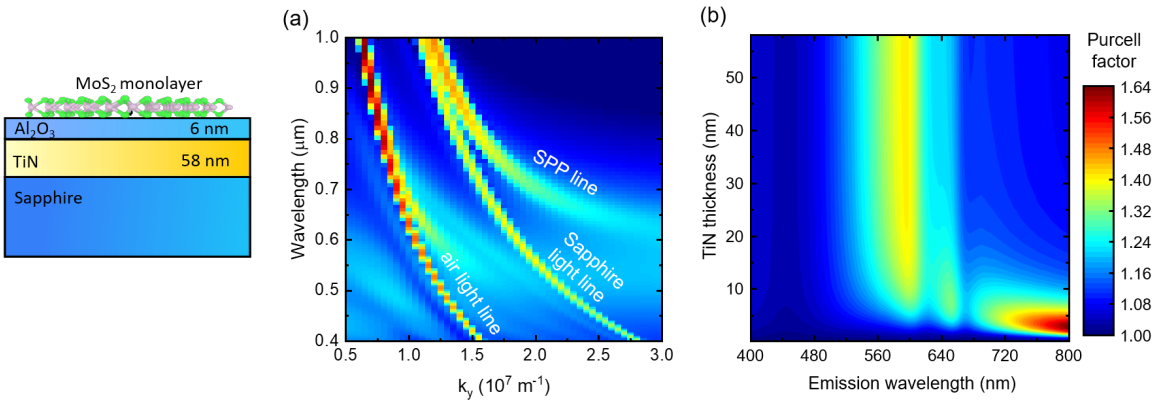

Fig. B. 4. (a) Dispersion relation of MoS_2-Al_2O_3-TiN-sapphire structure whose schematics are shown on the left panel. (b) The Purcell factor for the horizontal dipole located at the center of the MoS_2 layer as the function of TiN film thickness and emission wavelength. The contour of the maximum Purcell factor corresponds to the SPP resonance. For ultrathin films, the shift of the SPP dispersion manifests in the redshift of the Purcell map.

B.5. Dependence of the PL Enhancement on the Permittivity of the TiN films

From ellipsometry measurement, the carrier concentration of 58 nm thick TiN film is found to be around $4x10^{22}$ cm^{-3}, we varied this quantity from 10^{22} to 10^{23} cm^{-3} and calculated the field intensity enhancement in the wavelength range 400 to 590 nm (Fig. S5a) and external quantum efficiency (EQE) enhancement in the emission wavelength range 575 to 740 nm (Fig. S5b) for the MoS_2-Al_2O_3-TiN stack for 6nm Al_2O_3 spacer. The effect of the permittivity of TiN on the MoS_2 emission can be clearly seen as maximum contours in these figures. The constant TiN permittivity (real part) curves are overlaid on the contour maps so that the maximum enhancement and the TiN permittivity can be correlated. The maximum field intensity contour in Fig. S5a is slightly displaced from the ENZ curve because of the losses in the TiN material. As the carrier density increases, the losses in the TiN increases; as a result, deviation of maximum enhancement from ENZ

gets larger towards the large carrier density region of the map. The effect of ENZ is more clearly seen in the emission enhancement plot as the maximum EQE follows the ENZ curve very closely. Along this line, TiN has the smaller refractive index than air and emission is preferentially directed toward the air (see Fig. B.5c). The minimum at real permittivity contour -2.8 can be attributed to the SPP contribution.

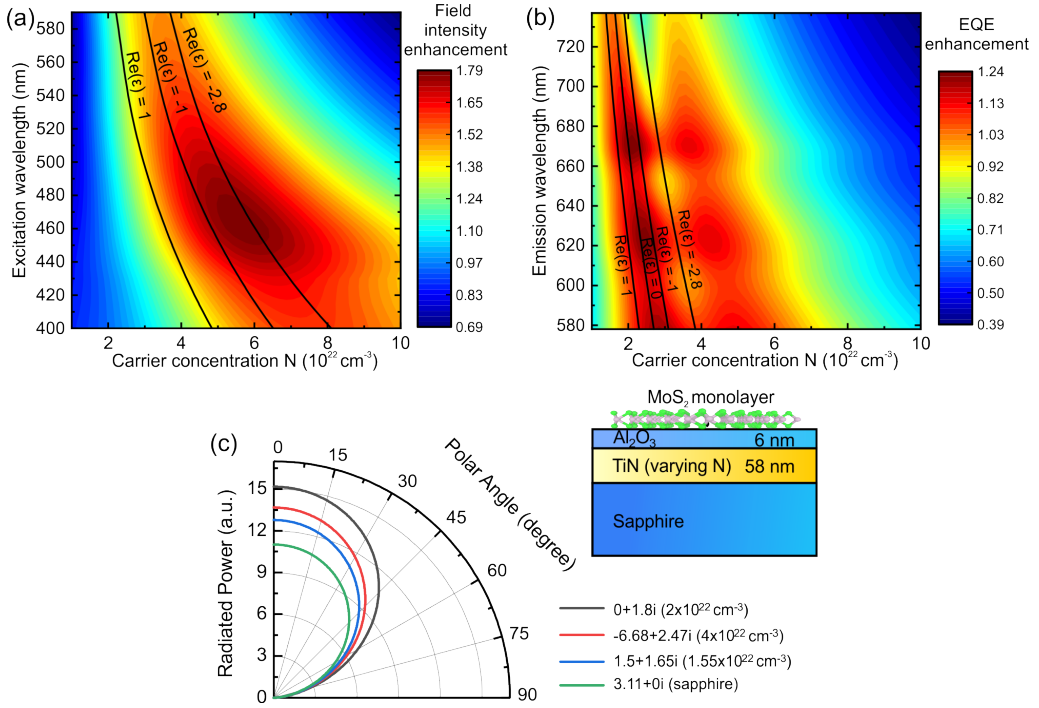

Fig. B. 5. (a) Field intensity enhancement and (b) EQE enhancement for a horizontal dipole inside MoS_2 on 6 nm thick spacer on 58 nm thick TiN (schematics on the bottom) with respect to that on sapphire substrate for a varying carrier concentration. The overlaid black curves show the real part of permittivity of TiN. (c) The radiated power from the dipole at the center of MoS_2 as a function of polar angle at the 671 nm emission wavelength, for varying carrier concentration of TiN shown inside the parentheses in the legend. The radiated power towards the air is largest on the ENZ TiN (black curve); followed by the metallic TiN (red curve), dielectric TiN (blue curve) and on Sapphire (green curve).

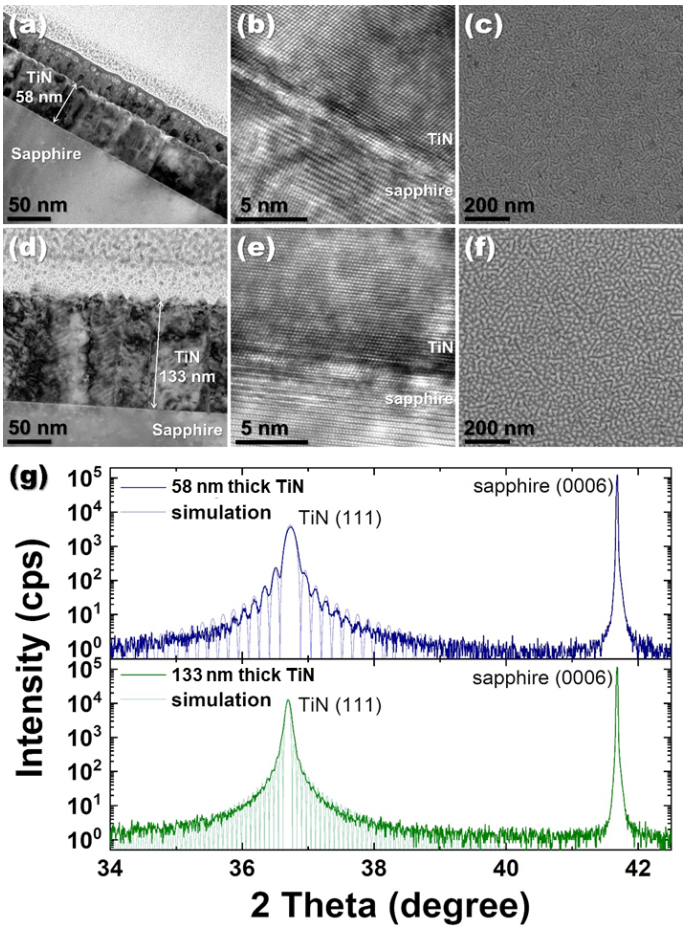

Fig. B. 6. TEM cross-sectional images for (a) 58 nm thick TiN, and (d) 133 nm thick TiN. The atomic-resolution TEM images of (b) 58 nm thick TiN, and (e) 133 nm thick. The layer spacing for 58 nm thick TiN and 133 nm thick are 2.43 Å and 2.45 Å, respectively. The sharp interface between TiN and sapphire is also demonstrated. The SEM top views of (c) Sample A showing the brain-folds-like structure, and (f) 133 nm thick showing the triangle boundary with ~20 nm edge. (g) Experimental (navy-blue line (58 nm thick TiN), and olive-green line (133 nm thick)) and simulated (light-blue line (58 nm thick TiN), and light-green line (133 nm thick)) HR-XRD theta-2theta spectra for TiN (111) grown on the c-sapphire. The film thickness around TiN (111) reflection can be determined by Kiessig fringes.

BIBLIOGRAPHY

1. Stockman, M. I., Nanofocusing of optical energy in tapered plasmonic waveguides. *Phys Rev Lett* **2004,** *93* (13).

2. Zhang, R.; Zhang, Y.; Dong, Z. C.; Jiang, S.; Zhang, C.; Chen, L. G.; Zhang, L.; Liao, Y.; Aizpurua, J.; Luo, Y.; Yang, J. L.; Hou, J. G., Chemical mapping of a single molecule by plasmon-enhanced Raman scattering. *Nature* **2013,** *498*, 82.

3. Campione, S.; Kim, I.; Ceglia, D. d.; Keeler, G. A.; Luk, a. T. S., Experimental verification of epsilon-near-zero plasmon polariton modes in degenerately doped semiconductor nanolayers. *Opt Express* **2016,** *24*, 18782-18789.

4. Girón-Sedas, J.; Gómez, F. R.; Albella, P.; Mejía-Salazar, J.; Oliveira Jr, O. N., Giant enhancement of the transverse magneto-optical Kerr effect through the coupling of ε-near-zero and surface plasmon polariton modes. *Physical Review B* **2017,** *96* (7), 075415.

5. Halterman, K.; Feng, S. M.; Nguyen, V. C., Controlled leaky wave radiation from anisotropic epsilon near zero metamaterials. *Phys Rev B* **2011,** *84* (7).

6. Zhang, J.; Zhang, L.; Xu, W., Surface plasmon polaritons: physics and applications. *Journal of Physics D: Applied Physics* **2012,** *45* (11), 113001.

7. Babadjanyan, A. J.; Margaryan, N. L.; Nerkararyan, K. V., Superfocusing of Surface Polaritons in the Conical Structure. *J. Appl. Phys.* **2000,** *87* (8), 3785-3788.

8. Stockman, M. I., Nanofocusing of Optical Energy in Tapered Plasmonic Waveguides. *Phys. Rev. Lett.* **2004,** *93* (13), 019901.

9. Minn, K.; Birmingham, B.; Zhang, Z., New development of nanoscale spectroscopy using scanning probe microscope. *Journal of Vacuum Science & Technology A* **2020,** *38* (3), 030801.

10. Campione, S.; Brener, I.; Marquier, F., Theory of epsilon-near-zero modes in ultrathin films. *Phys Rev B* **2015,** *91* (12), 121408.

11. Kinsey, N.; DeVault, C.; Boltasseva, A.; Shalaev, V. M., Near-zero-index materials for photonics. *Nature Reviews Materials* **2019,** *4* (12), 742-760.

12. Novotny, L.; Hecht, B., *Principles of nano-optics*. Cambridge university press: 2012.

13. Gramotnev, D. K.; Bozhevolnyi, S. I., Plasmonics beyond the diffraction limit. *Nat Photonics* **2010,** *4* (2), 83-91.

14. Ding, W.; Andrews, S. R.; Maier, S. A., Internal excitation and superfocusing of surface plasmon polaritons on a silver-coated optical fiber tip. *Phys Rev A* **2007,** *75* (6).

15. Berweger, S.; Atkin, J. M.; Olmon, R. L.; Raschke, M. B., Adiabatic Tip-Plasmon Focusing for Nano-Raman Spectroscopy. *J Phys Chem Lett* **2010,** *1* (24), 3427-3432.

16. Tugchin, B. N.; Janunts, N.; Klein, A. E.; Steinert, M.; Fasold, S.; Diziain, S.; Sison, M.; Kley, E. B.; Tunnermann, A.; Pertsch, T., Plasmonic Tip Based on Excitation of Radially Polarized Conical Surface Plasmon Polariton for Detecting Longitudinal and Transversal Fields. *Acs Photonics* **2015,** *2* (10), 1468-1475.

17. Tuniz, A.; Chemnitz, M.; Dellith, J.; Weidlich, S.; Schmidt, M. A., Hybrid-Mode-Assisted Long-Distance Excitation of Short-Range Surface Plasmons in a Nanotip-Enhanced Step-Index Fiber. *Nano Lett* **2017,** *17* (2), 631-637.

18. Jiang, R. H.; Chen, C.; Lin, D. Z.; Chou, H. C.; Chu, J. Y.; Yen, T. J., Near-Field Plasmonic Probe with Super Resolution and High Throughput and Signal-to-Noise Ratio. *Nano Lett* **2018,** *18* (2), 881-885.

19. Chen, X.-W.; Sandoghdar, V.; Agio, M., Highly Efficient Interfacing of Guided Plasmons and Photons in Nanowires. *Nano Lett* **2009,** *9* (11), 3756-3761.

20. Tuniz, A.; Schmidt, M. A., Interfacing optical fibers with plasmonic nanoconcentrators. *Nanophotonics* **2018,** *7* (7), 1279.

21. Frey, H. G.; Keilmann, F.; Kriele, A.; Guckenberger, R., Enhancing the resolution of scanning near-field optical microscopy by a metal tip grown on an aperture probe. *Appl Phys Lett* **2002,** *81* (26), 5030-5032.

22. Minn, K.; Howard Lee, H. W.; Zhang, Z., Enhanced subwavelength coupling and nano-focusing with optical fiber-plasmonic hybrid probe. *Opt Express* **2019,** *27* (26), 38098-38108.

23. Yoon, J.; Zhou, M.; Badsha, M. A.; Kim, T. Y.; Jun, Y. C.; Hwangbo, C. K., Broadband Epsilon-Near-Zero Perfect Absorption in the Near-Infrared. *Sci Rep-Uk* **2015,** *5*, 12788.

24. Luk, T. S.; Campione, S.; Kim, I.; Feng, S. M.; Jun, Y. C.; Liu, S.; Wright, J. B.; Brener, I.; Catrysse, P. B.; Fan, S. H.; Sinclair, M. B., Directional perfect absorption using deep subwavelength low-permittivity films. *Phys Rev B* **2014,** *90* (8), 085411.

25. Kim, T. Y.; Badsha, M. A.; Yoon, J.; Lee, S. Y.; Jun, Y. C.; Hwangbo, C. K., General Strategy for Broadband Coherent Perfect Absorption and Multi-wavelength All-optical Switching Based on Epsilon-Near-Zero Multilayer Films. *Sci Rep-Uk* **2016,** *6*, 22941

26. Feng, S.; Halterman, K., Coherent perfect absorption in epsilon-near-zero metamaterials. *Phys Rev B* **2012,** *86* (16).

27. Campione, S.; Wendt, J. R.; Keeler, G. A.; Luk, T. S., Near-Infrared Strong Coupling between Metamaterials and Epsilon-near-Zero Modes in Degenerately Doped Semiconductor Nanolayers. *Acs Photonics* **2016,** *3* (2), 293-297.

28. Kaltenbaek, R.; Aspelmeyer, M.; Barker, P. F.; Bassi, A.; Bateman, J.; Bongs, K.; Bose, S.; Braxmaier, C.; Brukner, C.; Christophe, B.; Chwalla, M.; Cohadon, P. F.; Cruise, A. M.; Curceanu, C.; Dholakia, K.; Diosi, L.; Doringshoff, K.; Ertmer, W.; Gieseler, J.; Gurlebeck, N.; Hechenblaikner, G.; Heidmann, A.; Herrmann, S.; Hossenfelder, S.; Johann, U.; Kiesel, N.; Kim, M.; Lammerzahl, C.; Lambrecht, A.; Mazilu, M.; Milburn, G. J.; Muller, H.; Novotny, L.; Paternostro, M.; Peters, A.; Pikovski, I.; Zanoni, A. P.; Rasel, E. M.; Reynaud, S.; Riedel, C. J.; Rodrigues, M.; Rondin, L.; Roura, A.; Schleich, W. P.; Schmiedmayer, J.; Schuldt, T.; Schwab, K. C.; Tajmar, M.; Tino, G. M.; Ulbricht, H.; Ursin, R.; Vedral, V., Macroscopic Quantum Resonators (MAQRO): 2015 update. *Epj Quantum Technol* **2016,** *3*.

29. Capretti, A.; Wang, Y.; Engheta, N.; Dal Negro, L., Comparative Study of Second-Harmonic Generation from Epsilon-Near-Zero Indium Tin Oxide and Titanium Nitride Nanolayers Excited in the Near-Infrared Spectral Range. *Acs Photonics* **2015,** *2* (11), 1584-1591.

30. Caspani, L.; Kaipurath, R. P. M.; Clerici, M.; Ferrera, M.; Roger, T.; Kim, J.; Kinsey, N.; Pietrzyk, M.; Di Falco, A.; Shalaev, V. M.; Boltasseva, A.; Faccio, D., Enhanced Nonlinear Refractive Index in epsilon-Near-Zero Materials. *Phys Rev Lett* **2016,** *116* (23), 233901.

31. Kinsey, N.; DeVault, C.; Kim, J.; Ferrera, M.; Shalaev, V. M.; Boltasseva, A., Epsilon-near-zero Al-doped ZnO for ultrafast switching at telecom wavelengths. *Optica* **2015,** *2* (7), 616-622.

32. Alam, M. Z.; De Leon, I.; Boyd, R. W., Large optical nonlinearity of indium tin oxide in its epsilon-near-zero region. *Science* **2016,** *352* (6287), 795-7.

33. Yang, Y. M.; Kelley, K.; Sachet, E.; Campione, S.; Luk, T. S.; Maria, J. P.; Sinclair, M. B.; Brener, I., Femtosecond optical polarization switching using a cadmium oxide-based perfect absorber. *Nat Photonics* **2017,** *11* (6), 390-+.

34. Park, J.; Kang, J. H.; Liu, X.; Brongersma, M. L., Electrically Tunable Epsilon-Near-Zero (ENZ) Metafilm Absorbers. *Sci Rep-Uk* **2015,** *5*, 15754.

35. Huang, Y. W.; Lee, H. W.; Sokhoyan, R.; Pala, R. A.; Thyagarajan, K.; Han, S.; Tsai, D. P.; Atwater, H. A., Gate-Tunable Conducting Oxide Metasurfaces. *Nano Lett* **2016,** *16* (9), 5319-25.

36. Lee, H. W.; Papadakis, G.; Burgos, S. P.; Chander, K.; Kriesch, A.; Pala, R.; Peschel, U.; Atwater, H. A., Nanoscale Conducting Oxide PlasMOStor. *Nano Letters* **2014,** *14* (11), 6463-6468.

37. Alù, A.; Engheta, N., Boosting Molecular Fluorescence with a Plasmonic Nanolauncher. *Phys Rev Lett* **2009,** *103* (4), 043902.

38. Fleury, R.; Alù, A., Enhanced superradiance in epsilon-near-zero plasmonic channels. *Phys Rev B* **2013,** *87* (20), 201101.

39. Caligiuri, V.; Palei, M.; Imran, M.; Manna, L.; Krahne, R., Planar Double-Epsilon-Near-Zero Cavities for Spontaneous Emission and Purcell Effect Enhancement. *Acs Photonics* **2018,** *5* (6), 2287-2294.

40. Labelle, A. J.; Bonifazi, M.; Tian, Y.; Wong, C.; Hoogland, S.; Favraud, G.; Walters, G.; Sutherland, B.; Liu, M.; Li, J.; Zhang, X.; Kelley, S. O.; Sargent, E. H.; Fratalocchi, A., Broadband Epsilon-near-Zero Reflectors Enhance the Quantum Efficiency of Thin Solar Cells at Visible and Infrared Wavelengths. *ACS Applied Materials & Interfaces* **2017,** *9* (6), 5556-5565.

41. Buscema, M.; Steele, G. A.; van der Zant, H. S. J.; Castellanos-Gomez, A., The effect of the substrate on the Raman and photoluminescence emission of single-layer MoS2. *Nano Res.* **2014,** *7* (4), 561-571.

42. Liu, J. T.; Wang, T. B.; Li, X. J.; Liu, N. H., Enhanced absorption of monolayer MoS2 with resonant back reflector. *J. Appl. Phys.* **2014,** *115* (19), 193511.

43. Jeong, H. Y.; Kim, U. J.; Kim, H.; Han, G. H.; Lee, H.; Kim, M. S.; Jin, Y.; Ly, T. H.; Lee, S. Y.; Roh, Y. G.; Joo, W. J.; Hwang, S. W.; Park, Y.; Lee, Y. H., Optical Gain in MoS2 via Coupling with Nanostructured Substrate: Fabry-Perot Interference and Plasmonic Excitation. *ACS Nano* **2016,** *10* (9), 8192-8198.

44. Wang, Q. X.; Guo, J.; Ding, Z. J.; Qi, D. Y.; Jiang, J. Z.; Wang, Z.; Chen, W.; Xiang, Y. J.; Zhang, W. J.; Wee, A. T. S., Fabry-Perot Cavity-Enhanced Optical Absorption in Ultrasensitive Tunable Photodiodes Based on Hybrid 2D Materials. *Nano Lett.* **2017,** *17* (12), 7593-7598.

45. Galfsky, T.; Sun, Z.; Considine, C. R.; Chou, C. T.; Ko, W. C.; Lee, Y. H.; Narimanov, E. E.; Menon, V. M., Broadband Enhancement of Spontaneous Emission in Two-Dimensional Semiconductors Using Photonic Hypercrystals. *Nano Lett.* **2016,** *16* (8), 4940-4945.

46. Hartschuh, A.; Sanchez, E. J.; Xie, X. S.; Novotny, L., High-resolution near-field Raman microscopy of single-walled carbon nanotubes. *Phys Rev Lett* **2003,** *90* (9).

47. Poliani, E.; Wagner, M. R.; Vierck, A.; Herziger, F.; Nenstiel, C.; Gannott, F.; Schweiger, M.; Fritze, S.; Dadgar, A.; Zaumsei, J.; Krost, A.; Hoffmann, A.; Maultzsch, J., Breakdown of Far-Field Raman Selection Rules by Light-Plasmon Coupling Demonstrated by Tip-Enhanced Raman Scattering. *J Phys Chem Lett* **2017,** *8* (22), 5462-5471.

48. Birmingham, B.; Liege, Z.; Larson, N.; Lu, W. G.; Park, K. T.; Lee, H. W. H.; Voronine, D. V.; Scully, M. O.; Zhang, Z. R., Probing Interaction between Individual Submonolayer Nanoislands and Bulk MoS2 Using Ambient TERS. *J Phys Chem C* **2018,** *122* (5), 2753-2760.

49. Kang, G.; Yang, M. W.; Mattei, M. S.; Schatz, G. C.; Van Duyne, R. P., In Situ Nanoscale Redox Mapping Using Tip-Enhanced Raman Spectroscopy. *Nano Lett* **2019,** *19* (3), 2106-2113.

50. Bhattarai, A.; El-Khoury, P. Z., Nanoscale Chemical Reaction Imaging at the Solid-Liquid Interface via TERS. *J Phys Chem Lett* **2019,** *10* (11), 2817-2822.

51. Tuniz, A.; Schmidt, M. A., Interfacing optical fibers with plasmonic nanoconcentrators. *Nanophotonics* **2018,** *7* (7), 1279-1298.

52. Lee, H. W.; Schmidt, M. A.; Tyagi, H. K.; Sempere, L. P.; Russell, P. S. J., Polarization-dependent coupling to plasmon modes on submicron gold wire in photonic crystal fiber. *Appl Phys Lett* **2008,** *93* (11).

53. Yang, J. Y.; Ghimire, I.; Wu, P. C.; Gurung, S.; Arndt, C.; Tsai, D. P.; Lee, H. W. H., Photonic crystal fiber metalens. *Nanophotonics* **2019,** *8* (3), 443-449.

54. Lindquist, N. C.; Nagpal, P.; Lesuffleur, A.; Norris, D. J.; Oh, S. H., Three-Dimensional Plasmonic Nanofocusing. *Nano Lett* **2010,** *10* (4), 1369-1373.

55. Bao, W.; Melli, M.; Caselli, N.; Riboli, F.; Wiersma, D. S.; Staffaroni, M.; Choo, H.; Ogletree, D. F.; Aloni, S.; Bokor, J.; Cabrini, S.; Intonti, F.; Salmeron, M. B.; Yablonovitch, E.; Schuck, P. J.; Weber-Bargioni, A., Mapping Local Charge Recombination Heterogeneity by Multidimensional Nanospectroscopic Imaging. *Science* **2012,** *338* (6112), 1317-1321.

56. Mivelle, M.; van Zanten, T. S.; Garcia-Parajo, M. F., Hybrid Photonic Antennas for Subnanometer Multicolor Localization and Nanoimaging of Single Molecules. *Nano Lett* **2014,** *14* (8), 4895-4900.

57. Lee, H. W.; Schmidt, M. A.; Russell, R. F.; Joly, N. Y.; Tyagi, H. K.; Uebel, P.; Russell, P. S. J., Pressure-assisted melt-filling and optical characterization of Au nano-wires in microstructured fibers. *Opt Express* **2011,** *19* (13), 12180-12189.

58. Lee, H. W.; Schmidt, M. A.; Russell, P. S. J., Excitation of a nanowire "molecule" in gold-filled photonic crystal fiber. *Opt Lett* **2012,** *37* (14), 2946-2948.

59. Uebel, P.; Schmidt, M. A.; Lee, H. W.; Russell, P. S., Polarisation-resolved near-field mapping of a coupled gold nanowire array. *Opt Express* **2012,** *20* (27), 28409-28417.

60. Vogel, M. W.; Gramotnev, D. K., Shape effects in tapered metal rods during adiabatic nanofocusing of plasmons. *J Appl Phys* **2010,** *107* (4), 044303.

61. Thu, N. T.; Tanaka, K.; Tanaka, M.; Chien, D. N., Superfocusing of surface plasmon polaritons by metal-coated dielectric probe of tilted conical shape. *J Opt Soc Am A* **2013,** *30* (6), 1113-1118.

62. Weber, T.; Kiel, T.; Irsen, S.; Busch, K.; Linden, S., Near-field study on the transition from localized to propagating plasmons on 2D nano-triangles. *Opt Express* **2017,** *25* (15), 16947-16956.

63. Aizpurua, J.; Bryant, G. W.; Richter, L. J.; de Abajo, F. J. G.; Kelley, B. K.; Mallouk, T., Optical properties of coupled metallic nanorods for field-enhanced spectroscopy. *Phys Rev B* **2005,** *71* (23).

64. Yariv, A.; Yeh, P., Photonics: optical electronics in modern communications (the oxford series in electrical and computer engineering). *Oxford University Press, Inc* **2006,** *231*, 232.

65. Huth, F.; Chuvilin, A.; Schnell, M.; Amenabar, I.; Krutokhvostov, R.; Lopatin, S.; Hillenbrand, R., Resonant Antenna Probes for Tip-Enhanced Infrared Near-Field Microscopy. *Nano Lett* **2013,** *13* (3), 1065-1072.

66. TipsNano AFM probes and accessories. https://tipsnano.com/catalog/snom/snom-fiber-probes/mf003/ (accessed 25 June 2020).

67. Ropers, C.; Neacsu, C. C.; Elsaesser, T.; Albrecht, M.; Raschke, M. B.; Lienau, C., Grating-coupling of surface plasmons onto metallic tips: A nanoconfined light source. *Nano Lett* **2007,** *7* (9), 2784-2788.

68. Neacsu, C. C.; Berweger, S.; Olmon, R. L.; Saraf, L. V.; Ropers, C.; Raschke, M. B., Near-Field Localization in Plasmonic Superfocusing: A Nanoemitter on a Tip. *Nano Lett* **2010,** *10* (2), 592-596.

69. Auwarter, D.; Mihaljevic, J.; Meixner, A. J.; Zimmermann, C.; Slama, S., Coupling of optical far fields into apertureless plasmonic nanofiber tips. *Phys Rev A* **2013,** *88* (6).

70. Gazzadi, G. C.; Frabboni, S.; Menozzi, C., Suspended nanostructures grown by electron beam-induced deposition of Pt and TEOS precursors. *Nanotechnology* **2007,** *18* (44), 445709.

71. Fernandez-Pacheco, A.; De Teresa, J. M.; Cordoba, R.; Ibarra, M. R., Metal-insulator transition in Pt-C nanowires grown by focused-ion-beam-induced deposition. *Phys Rev B* **2009,** *79* (17), 174204.

72. Palik, E. D., *Handbook of optical constants of solids*. Academic press: 1998; Vol. 3.

73. Johnson, P. B.; Christy, R. W., Optical Constants of Noble Metals. *Phys Rev B* **1972,** *6* (12), 4370-4379.

74. Zhou, W. J.; Mandia, D. J.; Barry, S. T.; Albert, J., Absolute near-infrared refractometry with a calibrated tilted fiber Bragg grating. *Opt Lett* **2015,** *40* (8), 1713-1716.

75. Stolen, R. H.; Tom, H. W. K., Self-organized phase-matched harmonic generation in optical fibers. *Opt Lett* **1987,** *12* (8), 585-587.

76. Granzow, N.; Stark, S. P.; Schmidt, M. A.; Tverjanovich, A.; Wondraczek, L.; Russell, P. S. J., Supercontinuum generation in chalcogenide-silica step-index fibers. *Opt Express* **2011,** *19* (21), 21003-21010.

77. Caucheteur, C.; Guo, T.; Albert, J., Review of plasmonic fiber optic biochemical sensors: improving the limit of detection. *Anal Bioanal Chem* **2015,** *407* (14), 3883-3897.

78. Mowbray, S. E.; Amiri, A. M., A Brief Overview of Medical Fiber Optic Biosensors and Techniques in the Modification for Enhanced Sensing Ability. *Diagnostics* **2019,** *9* (1), 2075-4418.

79. Bayindir, M.; Sorin, F.; Abouraddy, A. F.; Viens, J.; Hart, S. D.; Joannopoulos, J. D.; Fink, Y., Metal–insulator–semiconductor optoelectronic fibres. *Nature* **2004,** *431* (7010), 826-829.

80. Heeres, R. W.; Kouwenhoven, L. P.; Zwiller, V., Quantum interference in plasmonic circuits. *Nat Nanotechnol* **2013,** *8* (10), 719-722.

81. Ma, X.; Zhu, Y.; Yu, N.; Kim, S.; Liu, Q.; Apontti, L.; Xu, D.; Yan, R.; Liu, M., Toward High-Contrast Atomic Force Microscopy-Tip-Enhanced Raman Spectroscopy Imaging: Nanoantenna-Mediated Remote-Excitation on Sharp-Tip Silver Nanowire Probes. *Nano Lett* **2019,** *19* (1), 100-107.

82. Berweger, S.; Atkin, J. M.; Olmon, R. L.; Raschke, M. B., Light on the Tip of a Needle: Plasmonic Nanofocusing for Spectroscopy on the Nanoscale. *The Journal of Physical Chemistry Letters* **2012,** *3* (7), 945-952.

83. Zhou, Z.-K.; Liu, J.; Bao, Y.; Wu, L.; Png, C. E.; Wang, X.-H.; Qiu, C.-W., Quantum plasmonics get applied. *Progress in Quantum Electronics* **2019,** *65*, 1-20.

84. Lee, H. W.; Schmidt, M. A.; Tyagi, H. K.; Sempere, L. P.; Russell, P. S. J., Polarization-dependent coupling to plasmon modes on submicron gold wire in photonic crystal fiber. *Appl Phys Lett* **2008,** *93* (11), 111102.

85. Guo, X.; Qiu, M.; Bao, J.; Wiley, B. J.; Yang, Q.; Zhang, X.; Ma, Y.; Yu, H.; Tong, L., Direct Coupling of Plasmonic and Photonic Nanowires for Hybrid Nanophotonic Components and Circuits. *Nano Lett* **2009,** *9* (12), 4515-4519.

86. Li, X.; Li, W.; Guo, X.; Lou, J.; Tong, L., All-fiber hybrid photon-plasmon circuits: integrating nanowire plasmonics with fiber optics. *Opt Express* **2013,** *21* (13), 15698-15705.

87. Kim, S.; Yu, N.; Ma, X.; Zhu, Y.; Liu, Q.; Liu, M.; Yan, R., High external-efficiency nanofocusing for lens-free near-field optical nanoscopy. *Nat Photonics* **2019,** *13* (9), 636-643.

88. Koops, H. W. P.; Weiel, R.; Kern, D. P.; Baum, T. H., High-resolution electron-beam induced deposition. *Journal of Vacuum Science & Technology B: Microelectronics Processing and Phenomena* **1988,** *6* (1), 477-481.

89. Huth, M.; Porrati, F.; Dobrovolskiy, O. V., Focused electron beam induced deposition meets materials science. *Microelectronic Engineering* **2018,** *185-186*, 9-28.

90. Birks, T. A.; Knight, J. C.; Russell, P. S. J., Endlessly single-mode photonic crystal fiber. *Opt Lett* **1997,** *22* (13), 961-963.

91. Silvis-Cividjian, N.; Hagen, C. W.; Kruit, P., Spatial resolution limits in electron-beam-induced deposition. *J Appl Phys* **2005,** *98* (8), 084905.

92. Zhang, S.; Wei, H.; Bao, K.; Håkanson, U.; Halas, N. J.; Nordlander, P.; Xu, H., Chiral Surface Plasmon Polaritons on Metallic Nanowires. *Phys Rev Lett* **2011,** *107* (9), 096801.

93. Pan, D.; Wei, H.; Jia, Z.; Xu, H., Mode Conversion of Propagating Surface Plasmons in Nanophotonic Networks Induced by Structural Symmetry Breaking. *Sci Rep-Uk* **2014,** *4* (1), 4993.

94. Chang, D. E.; Sørensen, A. S.; Hemmer, P. R.; Lukin, M. D., Strong coupling of single emitters to surface plasmons. *Phys Rev B* **2007,** *76* (3), 035420.

95. Thu, N. T.; Tanaka, K.; Tanaka, M.; Chien, D. N., Superfocusing of surface plasmon polaritons by metal-coated dielectric probe of tilted conical shape. *Journal of the Optical Society of America A* **2013,** *30* (6), 1113-1118.

96. Stockman, M. I., Nanofocusing of Optical Energy in Tapered Plasmonic Waveguides. *Phys Rev Lett* **2004,** *93* (13), 137404.

97. Alù, A.; Silveirinha, M. G.; Salandrino, A.; Engheta, N., Epsilon-near-zero metamaterials and electromagnetic sources: Tailoring the radiation phase pattern. *Phys Rev B* **2007,** *75*, 155410.

98. Ziolkowski, R. W., Propagation in and scattering from a matched metamaterial having a zero index of refraction. *Phys Rev E* **2004,** *70* (4), 046608.

99. Davoyan, A. R.; Mahmoud, A. M.; Engheta, N., Optical isolation with epsilon-near-zero metamaterials. *Opt Express* **2013,** *21* (3), 3279-3286.

100. Silveirinha, M.; Engheta, N., Tunneling of electromagnetic energy through subwavelength channels and bends using epsilon-near-zero materials. *Phys Rev Lett* **2006,** *97* (15), 157403.

101. Alu, A.; Engheta, N., Dielectric sensing in epsilon-near-zero narrow waveguide channels. *Phys Rev B* **2008,** *78* (4).

102. Powell, D. A.; Alu, A.; Edwards, B.; Vakil, A.; Kivshar, Y. S.; Engheta, N., Nonlinear control of tunneling through an epsilon-near-zero channel. *Phys Rev B* **2009,** *79* (24).

103. Anopchenko, A.; Lee, H. W. H. In *ENZ Conducting Oxide Broadband Perfect Absorbers with Deep Sub-Wavelength Thicknesses*, Conference on Lasers and Electro-Optics, San Jose, California, 2017/05/14; Optical Society of America: San Jose, California, 2017; p JTh2A.94.

104. Campione, S.; Brener, I.; Marquier, F., Theory of epsilon-near-zero modes in ultrathin films. *Phys Rev B* **2015,** *91* (12).

105. Russell, P., Photonic crystal fibers. *Science* **2003,** *299* (5605), 358-62.

106. Tuniz, A.; Jain, C.; Weidlich, S.; Schmidt, M. A., Broadband azimuthal polarization conversion using gold nanowire enhanced step-index fiber. *Opt Lett* **2016,** *41* (3), 448-451.

107. Faez, S.; Lahini, Y.; Weidlich, S.; Garmann, R. F.; Wondraczek, K.; Zeisberger, M.; Schmidt, M. A.; Orrit, M.; Manoharan, V. N., Fast, Label-Free Tracking of Single Viruses and Weakly Scattering Nanoparticles in a Nanofluidic Optical Fiber. *ACS Nano* **2015,** *9* (12), 12349-57.

108. Naik, G. V.; Kim, J.; Boltasseva, A., Oxides and nitrides as alternative plasmonic materials in the optical range *Optical Materials Express* **2011,** *1* (6), 1090-1099.

109. Noginov, M. A.; Gu, L.; Livenere, J.; Zhu, G.; Pradhan, A. K.; Mundle, R.; Bahoura, M.; Barnakov, Y. A.; Podolskiy, V. A., Transparent conductive oxides: Plasmonic materials for telecom wavelengths. *Appl Phys Lett* **2011,** *99* (2), 021101.

110. Abb, M.; Sepulveda, B.; Chong, H. M. H.; Muskens, O. L., Transparent conducting oxides for active hybrid metamaterial devices. *Journal of Optics* **2012,** *14* (11), 114007.

111. Malek, G. A.; Aytug, T.; Liu, Q. F.; Wu, J. D., Plasmonic Three-Dimensional Transparent Conductor Based on Al-Doped Zinc Oxide-Coated Nanostructured Glass Using Atomic Layer Deposition. *Acs Appl Mater Inter* **2015,** *7* (16), 8556-8561.

112. Tarasov, K.; Raccurt, O., A wet chemical preparation of transparent conducting thin films of Al-doped ZnO nanoparticles. *J Nanopart Res* **2011,** *13* (12), 6717-6724.

113. Raether, H., Surface-Plasmons on Smooth and Rough Surfaces and on Gratings. *Springer Trac Mod Ph* **1988,** *111*, 1-133.

114. Kedenburg, S.; Vieweg, M.; Gissibl, T.; Giessen, H., Linear refractive index and absorption measurements of nonlinear optical liquids in the visible and near-infrared spectral region. *Optical Materials Express* **2012,** *2* (11), 1588-1611.

115. Moutzouris, K.; Papamichael, M.; Betsis, S. C.; Stavrakas, I.; Hloupis, G.; Triantis, D., Refractive, dispersive and thermo-optic properties of twelve organic solvents in the visible and near-infrared. *Appl Phys B-Lasers O* **2014,** *116* (3), 617-622.

116. Ni, K.; Dong, X. Y.; Chan, C. C.; Li, T.; Hu, L. M.; Qian, W. W., Miniature refractometer based on Mach-Zehnder interferometer with waist-enlarged fusion bitaper. *Opt Commun* **2013,** *292*, 84-86.

117. Chen, Y. F.; Han, Q.; Liu, T. G.; Lu, X. Y., Self-temperature-compensative refractometer based on singlemode-multimode-singlemode fiber structure. *Sensor Actuat B-Chem* **2015,** *212*, 107-111.

118. Liang, W.; Huang, Y. Y.; Xu, Y.; Lee, R. K.; Yariv, A., Highly sensitive fiber Bragg grating refractive index sensors. *Appl Phys Lett* **2005,** *86* (15).

119. Chong, J. H.; Shum, P.; Haryono, H.; Yohana, A.; Rao, M. K.; Lu, C.; Zhu, Y. N., Measurements of refractive index sensitivity using long-period grating refractometer. *Opt Commun* **2004,** *229* (1-6), 65-69.

120. Wiederhecker, G. S.; Cordeiro, C. M. B.; Couny, F.; Benabid, F.; Maier, S. A.; Knight, J. C.; Cruz, C. H. B.; Fragnito, H. L., Field enhancement within an optical fibre with a subwavelength air core. *Nat Photonics* **2007,** *1* (2), 115-118.

121. Anopchenko, A.; Occhicone, A.; Rizzo, R.; Sinibaldi, A.; Figliozzi, G.; Danz, N.; Munzert, P.; Michelotti, F., Effect of thickness disorder on the performance of photonic crystal surface wave sensors. *Optics Express* **2016,** *24* (7), 7728-7742.

122. Yeh, P.; Yariv, A.; Hong, C. S., Electromagnetic Propagation in Periodic Stratified Media .1. General Theory. *J Opt Soc Am* **1977,** *67* (4), 423-438.

123. Holman, Z. C.; Filipic, M.; Descoeudres, A.; De Wolf, S.; Smole, F.; Topic, M.; Ballif, C., Infrared light management in high-efficiency silicon heterojunction and rear-passivated solar cells. *J Appl Phys* **2013,** *113* (1).

124. Butun, S.; Tongay, S.; Aydin, K., Enhanced Light Emission from Large-Area Monolayer MoS2 Using Plasmonic Nanodisc Arrays. *Nano Lett.* **2015,** *15* (4), 2700-2704.

125. Bahauddin, S. M.; Robatjazi, H.; Thomann, I., Broadband Absorption Engineering to Enhance Light Absorption in Monolayer MoS_2. *ACS Photonics* **2016,** *3* (5), 853-862.

126. Guler, U.; Boltasseva, A.; Shalaev, V. M., Refractory Plasmonics. *Science* **2014,** *344* (6181), 263.

127. Igasaki, Y.; Mitsuhashi, H.; Azuma, K.; Muto, T., Structure and Electrical Properties of Titanium Nitride Films. *Japanese Journal of Applied Physics* **1978,** *17* (1), 85-96.

128. Briggs, J. A.; Naik, G. V.; Petach, T. A.; Baum, B. K.; Goldhaber-Gordon, D.; Dionne, J. A., Fully CMOS-compatible titanium nitride nanoantennas. *Appl Phys Lett* **2016,** *108* (5), 051110.

129. Guo, W.-P.; Mishra, R.; Cheng, C.-W.; Wu, B.-H.; Chen, L.-J.; Lin, M.-T.; Gwo, S., Titanium Nitride Epitaxial Films as a Plasmonic Material Platform: Alternative to Gold. *ACS Photonics* **2019,** *6* (8), 1848-1854.

130. Kinsey, N.; Syed, A. A.; Courtwright, D.; DeVault, C.; Bonner, C. E.; Gavrilenko, V. I.; Shalaev, V. M.; Hagan, D. J.; Van Stryland, E. W.; Boltasseva, A., Effective third-order nonlinearities in metallic refractory titanium nitride thin films. *Optical Materials Express* **2015,** *5* (11), 2395-2403.

131. Wen, X. L.; Li, G. Y.; Gu, C. Y.; Zhao, J. X.; Wang, S. J.; Jiang, C. P.; Palomba, S.; de Sterke, C. M.; Xiong, Q. H., Doubly Enhanced Second Harmonic Generation through Structural and Epsilon-near-Zero Resonances in TiN Nanostructures. *Acs Photonics* **2018,** *5* (6), 2087-2093.

132. Kharitonov, A.; Kharintsev, S., Tunable optical materials for multi-resonant plasmonics: from TiN to TiON. *Opt. Mater. Express* **2020,** *10* (2), 513-531.

133. Braic, L.; Vasilantonakis, N.; Mihai, A.; Garcia, I. J. V.; Fearn, S.; Zou, B.; Alford, N. M.; Doiron, B.; Oulton, R. F.; Maier, S. A.; Zayats, A. V.; Petrov, P. K., Titanium Oxynitride Thin Films with Tunable Double Epsilon-Near-Zero Behavior for Nanophotonic Applications. *Acs Applied Materials & Interfaces* **2017,** *9* (35), 29857-29862.

134. Lu, Y.-J.; Sokhoyan, R.; Cheng, W.-H.; Kafaie Shirmanesh, G.; Davoyan, A. R.; Pala, R. A.; Thyagarajan, K.; Atwater, H. A., Dynamically controlled Purcell enhancement of visible spontaneous emission in a gated plasmonic heterostructure. *Nat Commun* **2017,** *8* (1), 1631.

135. Kharintsev, S. S.; Kharitonov, A. V.; Alekseev, A. M.; Kazarian, S. G., Superresolution stimulated Raman scattering microscopy using 2-ENZ nano-composites. *Nanoscale* **2019,** *11* (16), 7710-7719.

136. Kharintsev, S. S.; Kharitonov, A. V.; Gazizov, A. R.; Kazarian, S. G., Disordered Nonlinear Metalens for Raman Spectral Nanoimaging. *Acs Applied Materials & Interfaces* **2020,** *12* (3), 3862-3872.

137. Vertchenko, L.; Akopian, N.; Lavrinenko, A. V., Epsilon-Near-Zero Grids for On-chip Quantum Networks. *Sci Rep* **2019,** *9*, 7.

138. Kuc, A.; Zibouche, N.; Heine, T., Influence of quantum confinement on the electronic structure of the transition metal sulfide TS2. *Phys Rev B* **2011,** *83* (24), 245213.

139. Mak, K. F.; Lee, C.; Hone, J.; Shan, J.; Heinz, T. F., Atomically Thin MoS2: A New Direct-Gap Semiconductor. *Phys Rev Lett* **2010,** *105* (13), 136805.

140. Wang, Q. H.; Kalantar-Zadeh, K.; Kis, A.; Coleman, J. N.; Strano, M. S., Electronics and optoelectronics of two-dimensional transition metal dichalcogenides. *Nat Nanotechnol* **2012,** *7* (11), 699-712.

141. Moody, G.; Schaibley, J.; Xu, X. D., Exciton dynamics in monolayer transition metal dichalcogenides Invited. *J. Opt. Soc. Am. B-Opt. Phys.* **2016,** *33* (7), C39-C49.

142. Tripathi, L. N.; Iff, O.; Betzold, S.; Dusanowski, L.; Emmerling, M.; Moon, K.; Lee, Y. J.; Kwon, S. H.; Hofling, S.; Schneider, C., Spontaneous Emission Enhancement in Strain-Induced WSe2 Monolayer-Based Quantum Light Sources on Metallic Surfaces. *Acs Photonics* **2018,** *5* (5), 1919-1926.

143. Zhang, X.; De-Eknamkul, C.; Gu, J.; Boehmke, A. L.; Menon, V. M.; Khurgin, J.; Cubukcu, E., Guiding of visible photons at the ångström thickness limit. *Nat Nanotechnol* **2019,** *14* (9), 844-850.

144. Cihan, A. F.; Curto, A. G.; Raza, S.; Kik, P. G.; Brongersma, M. L., Silicon Mie resonators for highly directional light emission from monolayer MoS2. *Nat Photonics* **2018,** *12* (5), 284-290.

145. Godiksen, R. H.; Wang, S.; Raziman, T. V.; Guimaraes, M. H. D.; Rivas, J. G.; Curto, A. G., Correlated Exciton Fluctuations in a Two-Dimensional Semiconductor on a Metal. *Nano Lett.* **2020**.

146. Wang, H.; Zhang, C.; Rana, F., Ultrafast Dynamics of Defect-Assisted Electron–Hole Recombination in Monolayer MoS2. *Nano Lett* **2015,** *15* (1), 339-345.

147. Lien, D. H.; Uddin, S. Z.; Yeh, M.; Amani, M.; Kim, H.; Ager, J. W.; Yablonovitch, E.; Javey, A., Electrical suppression of all nonradiative recombination pathways in monolayer semiconductors. *Science* **2019,** *364* (6439), 468-471.

148. Schuller, J. A.; Karaveli, S.; Schiros, T.; He, K.; Yang, S.; Kymissis, I.; Shan, J.; Zia, R., Orientation of luminescent excitons in layered nanomaterials. *Nat Nanotechnol* **2013,** *8* (4), 271-276.

149. Chen, H. Y.; Palummo, M.; Sangalli, D.; Bernardi, M., Theory and Ab Initio Computation of the Anisotropic Light Emission in Monolayer Transition Metal Dichalcogenides. *Nano Lett.* **2018,** *18* (6), 3839-3843.

150. Johnson, P. B.; Christy, R. W., Optical Constants of the Noble Metals. *Phys Rev B* **1972,** *6* (12), 4370-4379.

151. Born, M.; Wolf, E.; Bhatia, A. B., *Principles of optics : electromagnetic theory of propagation, interference, and diffraction of light*. Seventh (expanded) anniversary edition, 60th anniversary edition. ed.; Cambridge University Press: Cambridge, 2019; p pages cm.

152. Krayer, L. J.; Kim, J.; Munday, J. N., Near-perfect absorption throughout the visible using ultra-thin metal films on index-near-zero substrates [Invited]. *Optical Materials Express* **2019,** *9* (1), 330-338.

153. Jun, Y. C.; Reno, J.; Ribaudo, T.; Shaner, E.; Greffet, J.-J.; Vassant, S.; Marquier, F.; Sinclair, M.; Brener, I., Epsilon-Near-Zero Strong Coupling in Metamaterial-Semiconductor Hybrid Structures. *Nano Lett* **2013,** *13* (11), 5391-5396.

154. Christopher, J. W.; Goldberg, B. B.; Swan, A. K., Long tailed trions in monolayer MoS_2: Temperature dependent asymmetry and resulting red-shift of trion photoluminescence spectra. *Sci Rep* **2017,** *7*, 14062.

155. Danz, N.; Waldhausl, R.; Brauer, A.; Kowarschik, R., Dipole lifetime in stratified media. *J. Opt. Soc. Am. B-Opt. Phys.* **2002,** *19* (3), 412-419.

156. Neyts, K. A., Simulation of light emission from thin-film microcavities. *J. Opt. Soc. Am. A-Opt. Image Sci. Vis.* **1998,** *15* (4), 962-971.

157. Bharadwaj, P.; Novotny, L., Spectral dependence of single molecule fluorescence enhancement. *Opt Express* **2007,** *15* (21), 14266-14274.

158. Amani, M.; Lien, D. H.; Kiriya, D.; Xiao, J.; Azcatl, A.; Noh, J.; Madhvapathy, S. R.; Addou, R.; Santosh, K. C.; Dubey, M.; Cho, K.; Wallace, R. M.; Lee, S. C.; He, J. H.; Ager, J. W.; Zhang, X.; Yablonovitch, E.; Javey, A., Near-unity photoluminescence quantum yield in MoS2. *Science* **2015,** *350* (6264), 1065-1068.

159. Galfsky, T.; Krishnamoorthy, H. N. S.; Newman, W.; Narimanov, E. E.; Jacob, Z.; Menon, V. M., Active hyperbolic metamaterials: enhanced spontaneous emission and light extraction. *Optica* **2015,** *2* (1), 62-65.

160. Wang, Y.; Sugimoto, H.; Inampudi, S.; Capretti, A.; Fujii, M.; Negro, L. D., Broadband enhancement of local density of states using silicon-compatible hyperbolic metamaterials. *Appl Phys Lett* **2015,** *106* (24), 241105.

161. Lee, K. J.; Xin, W.; Fann, C.; Ma, X.; Xing, F.; Liu, J.; Zhang, J.; Elkabbash, M.; Guo, C., Exciton dynamics in two-dimensional MoS2 on a hyperbolic metamaterial-based nanophotonic platform. *Phys Rev B* **2020,** *101* (4), 041405.

162. Wang, W.; Yang, X.; Luk, T. S.; Gao, J., Enhanced quantum dots spontaneous emission with metamaterial perfect absorbers. *Appl Phys Lett* **2019,** *114* (2), 021103.

163. Lu, D.; Kan, J. J.; Fullerton, E. E.; Liu, Z., Enhancing spontaneous emission rates of molecules using nanopatterned multilayer hyperbolic metamaterials. *Nat Nanotechnol* **2014,** *9* (1), 48-53.

164. Castellanos-Gomez, A.; Buscema, M.; Molenaar, R.; Singh, V.; Janssen, L.; van der Zant, H. S. J.; Steele, G. A., Deterministic transfer of two-dimensional materials by all-dry viscoelastic stamping. *2D Materials* **2014,** *1* (1), 011002.